Microstructural Investigation of Al/Al-Fe alloy-Al_2O_3 Interpenetrating Phase Composites Produced by Reactive Metal Penetration

by

Anthony M. Yurcho

Submitted in Partial Fulfillment of the Requirements

for the Degree of

Master of Science in Engineering

in the

Chemical Engineering

Program

YOUNGSTOWN STATE UNIVERSITY

May, 2011

Microstructural Investigation of Al/Al-Fe alloy-Al_2O_3 Interpenetrating Phase Composites Produced by Reactive Metal Penetration

by

Anthony M. Yurcho

I hereby release this thesis to the public. I understand this thesis will be housed at the Circulation Desk of the University library and will be available for public access. I also authorize the University or other individuals to make copies of this thesis as needed for scholarly research.

Signature:

Anthony M. Yurcho, student Date

Approvals:

Dr. Virgil C. Solomon, Thesis Advisor Date

Dr. Douglas M. Price, Committee Member Date

Dr. Timothy R. Wagner, Committee Member Date

Dr. Matthias Zeller, Committee Member Date

Dr. Peter J. Kasvinsky, Dean of Graduate Studies Date

Abstract

Aluminum-Al_2O_3 and Al alloy-Al_2O_3 based ceramic-metallic interpenetrating phase composites (IPC's) possess unique physical and mechanical properties that are desirable for a number of potential applications. Fireline TCON, Inc. (FTi) of Youngstown, OH produces such ceramic-metallic IPC's using a reactive metal penetration (RMP) process. The RMP process allows other materials and alloying metals to be added to the composite in order to tailor its final properties. Currently, TCON® IPC's are being marketed as refractory materials for handling high temperature molten metals. However, it is desired to expand the applications of ceramic-metallic IPC's to markets such as automotive brake rotors and military vehicle and body armor.

In order to tailor ceramic-metallic IPC's to different applications, a more thorough understanding of their microstructures and how they are affected by additions is necessary. In this study, the microstructural properties of two IPC's produced by the TCON RMP process were investigated. The materials include Al-Al_2O_3 and an Al-Fe alloy-Al_2O_3 ceramic-metallic IPCs. Analysis was performed using optical microscopy (OM), scanning electron microscopy (SEM), scanning/transmission electron microscopy (S/TEM), energy dispersive spectroscopy (EDS), focused ion beam (FIB), X-ray diffraction (XRD), and Vickers hardness testing. The results can be used to correlate the microstructure properties to the materials' physical performance. This information is valuable for developing IPC's modified for specific applications.

Acknowledgements

I am dedicating this thesis to my parents, Mr. and Mrs. George and Lisa Yurcho, and to my brother, Vincent Yurcho. Their endless love, unwavering support, and belief in me have served as my inspiration to dream and achieve beyond my own expectations.

I would like to thank my advisor, Dr. Virgil Solomon, for his constant support and guidance during my graduate studies at Youngstown State University. The research and analytical skills he has shared with me will undoubtedly allow me to excel as I further my career. Working with Dr. Solomon has helped me grow both as an individual and professional.

I would also like to thank my thesis committee members for their insight and contributions to this thesis. I would like to extend personal thanks to Dr. Douglas Price for his academic advisement both as an undergraduate and graduate student, Dr. Timothy Wagner for his part in coordinating this project and managing my student funding, and Dr. Matthias Zeller for his assistance with the XRD laboratory, interpretation of results, and editing.

I am also grateful for the support of Mr. Klaus-Markus Peters and Mr. Brian Hetzel of Fireline TCON, Inc. for providing me with the opportunity to study their company’s products and for their expertise in interpreting the results. They have gone above and beyond to provide me with the information and material necessary to complete my research.

I would also like to acknowledge Mr. and Mrs. Andrew and Carol Hirt of Materials Research Laboratory, Inc. and the entire MRL staff for the use of their facilities, expert technical advice, and support of my research endeavors.

Finally, I would like to thank my family and friends for their interest in my academic endeavors and their willingness to help me achieve my goals in any way that they can.

Table of Contents

List of Figures

List of Tables

List of Symbols and Terminology

Å	Ångstrom (10^{-10} m)
α	Alpha, lattice angle
a, b, c	Cell lattice parameters
Al	Aluminum
Al_2O_3	Aluminum oxide, alumina
At.%	Atomic percentage
β	Beta, lattice angle
Backscatter	Referring to elastic scattering of electrons or ions
°C	Degree Celsius
Clear Fused Quartz	Amorphous form of SiO_2
d	Distance, interplanar spacing
EDS	Energy dispersive spectroscopy
eV	Electron Volt
Fe	Iron
FIB	Focused ion beam
γ	Gamma, lattice angle
ΔG	Gibbs free energy (KJ/mol or kcal/mol)
GPa	Gigapascal (10^9 Pascals)
hr	Hour
HV	Vickers hardness value
IPC	Interpenetrating phase composite
K	Kelvin
L	Liquid
Micron	1 μm (10^{-6} m), micrometer
Mol	Mole
MPa	Megapascal (10^6 Pascals)
n	Integer (1,2,3,…,n)
N	Newton

O	Oxygen
OM	Optical microscopy
P	Load (N)
PCA	Phase cluster analysis
Preform	Starting material of the RMP process (typically silica based)
RMP	Reactive metal penetration
Secondary electron	Referring to inelastic scattering of electrons
SEM	Scanning electron microscopy
Si	Silicon
SiO_2	Silicon dioxide, silica
Space group	Classification describing a crystal’s symmetry
S/TEM	Scanning/transmission electron microscopy
TCON	Trademark name for Fireline TCON, Inc. IPC materials
TEM	Transmission electron microscopy
θ	Theta, incident angle
Transformation	Production of an IPC via chemical reaction during the RMP process
W/m K	Watts per meter Kelvin
wt.%	Weight percentage
XRD	X-ray diffraction
x,y,z	Coordinate/direction system

Chapter 1: Introduction

Interpenetrating phase composites (IPC's) are a class of materials that have been the topic of extensive research since the late 1980's.[7] IPC's are unique composite materials containing two or more interlocked phases that are continuous throughout the microstructure.[8] The interlocking of multiple phases, each of which contributes its own properties, results in a three-dimensional microstructure that has multifunctional characteristics.[9] The unique properties achieved by such materials makes them excellent candidates for replacing traditional materials in a number of applications. Current markets targeted for IPC implementation include: 1) high wear/corrosion resistant refractory shapes for handling molten metals, 2) lightweight vehicle braking components, and 3) high performance military body and vehicle armor.[10]

Some of the most widely studied IPC's, and the topic of this work, are those that contain a combination of ceramic and metallic phases. In particular, the Al_2O_3-Al system has been of focal interest amid research efforts. Al_2O_3-Al IPC's offer high thermal resistance and improved wear properties contributed by the ceramic phase with enhanced toughness achieved by the metal phase.[11] Even though the basic Al_2O_3-Al system is highly effective unmodified, several attempts to adapt the structure have been documented. The primary goal of these efforts is to produce materials with increased strength, hardness, and wear resistance.[12]

One method of tailoring ceramic-metallic IPC properties is by the addition of alloying elements. In this study, the effect of iron additions to the Al_2O_3-Al system is examined. Al-Fe alloys exhibit excellent resistance to oxidation and sulfidation, exhibit significantly improved mechanical properties at room temperature, and are relatively inexpensive compared to other (high-temperature) alloys.[13] Aside from these advantages, it is hypothesized that Al-Fe alloys contained within an Al_2O_3-Al composite will increase strength at elevated temperatures.[14] In addition, the potential formation of nano-scale intermetallic compounds may be beneficial in improving the properties of ceramic-metallic IPC's.[10]

Several processes have been proposed to manufacture ceramic-metallic IPC materials, including combustion synthesis,[15-17] pressurized melt infiltration,[17,18] and robotic deposition.[11] Each of these processes suffer from inefficiencies, such as size and shape restrictions, high product porosity, poor reproducibility, and excessive costs. Reactive Metal Penetration (RMP), which is sometimes referred to in the literature as a liquid-solid displacement reaction, is a viable solution to these processing issues.[7,8,10,19,20] RMP processing involves submerging a sacrificial ceramic preform into a molten metal bath for a given length of time and allowing chemical reactions to take place. While the dynamics of the RMP process make it a practical method for producing IPC's on an industrial scale,[10] strict conditions must be met for the reaction to produce the desired product.[21]

The reaction between the ceramic preform and molten metal during RMP processing can be classified as a thermite reaction. Thermite reactions are defined as an exothermic reaction between a metal (M) and a metallic or non-metallic oxide (AO) that forms a more stable oxide (MO) and the corresponding metal or non-metal of the reactant oxide (A), described by Eq. 1-1.[22] Thermite reactions are known specifically for high heat release, which often produces temperatures above the melting points of their products. The highly exothermic properties of these reactions generally cause them to proceed rapidly or uncontrollably and yield products with phases and structures not predicted by the overall equation.[23] However, a select few metal-oxide pairs will react slowly and in a predictable nature allowing the formation of a ceramic-metallic IPC.[21] One of these exceptions is the reaction between aluminum and silicon dioxide.

$$M + AO \rightarrow MO + A + \Delta G \qquad \text{(Eq. 1-1)}$$

The materials presented in this work were manufactured using the TCON process of Fireline TCON, Inc., located in Youngstown, Ohio. The TCON process is a unique RMP process in which the parameters are carefully controlled.[24] Basic Al_2O_3-Al TCON material is produced by reacting a clear fused quartz preform in a high temperature (≈1200 °C) molten aluminum bath, as represented by Eq. 1-2. Additional materials can be added to the process in order to alter the final properties, represented by Eq. 1-3.[10] It is important to note that clear fused quartz is not the only form of SiO_2 that can be transformed by this process. Polycrystalline SiO_2 preforms can also be transformed and offer some advantages in specific situations.[8] Current research has focused on using cost efficient materials, such as clays, as the ceramic preform.[10]

$3SiO_2 + 4Al \rightarrow 2Al_2O_3 + 3Si$ (Eq. 1-2)

$3SiO_2 + (\text{additives}) + 4Al \rightarrow 2Al_2O_3 + (\text{additives}) + 3Si$ (Eq. 1-3)

In this study, two TCON materials were investigated. Both materials were manufactured using clear fused quartz preforms transformed at approximately 1200 °C. The first was transformed in pure aluminum and the other in an aluminum-alloy containing 7.5 percent iron by weight. To increase the understanding of these TCON products, three supplementary materials were examined. They include a solidified sample of the Al-7.5wt.%Fe alloy melt, a TCON material produced by transforming clear fused quartz in an Al-25wt.%Si alloy, and a partially transformed TCON material (clear fused quartz in Al) stopped short of complete reaction. The materials were analyzed using optical microscopy (OM), scanning electron microscopy (SEM), energy dispersive spectroscopy (EDS), powder x-ray diffraction (XRD), focused ion beam (FIB) techniques, transmission electron microscopy (TEM), and Vickers indentation hardness testing.

The objective of this thesis is to provide a detailed microstructural analysis of the two TCON materials. This constitutes providing a compositional and structural description of phases, explanation of significant features including defects and porosity, and a measure of physical properties. This goal was realized by the utilization of the previously mentioned analytical techniques. A microstructural investigation of these materials is important because it provides crucial information pertaining to the manufacturing of TCON products. An understanding of how the RMP process is affected by alloying additions, such as Fe, can facilitate the development of ceramic-metallic IPC’s tailored to specific applications. Eventually, the large scale production of such materials can lead to cost and energy savings for a variety of industrial applications.

Chapter 2: Background

2.1. Introduction to Interpenetrating Phase Composites

Interpenetrating phase composites (IPC's) are a class of materials containing two or more continuous phases that are interconnected throughout a microstructure. Each phase contributes its own unique properties to the overall structure enabling multifunctional characteristics. For example, one phase might contribute strength while the other provides the necessary transport property. Traditional composite materials typically have a microstructure consisting of an isolated phase dispersed in a homogeneous matrix. The continuous property of IPC materials is advantageous over traditional composites because it allows a larger volume of the second phase. IPC's commonly occur in biology, such as mammal bones and the trunks and limbs of plants, but there are currently few large scale synthetic applications. Over the past two decades, IPC's have gained strong interest in the scientific community because their unique properties have expanded the capabilities and applications of composite materials. As a result, several means of producing such materials for industrial and commercial application have been researched.[9]

2.2. Ceramic-Metallic Interpenetrating Phase Composites

Among the most studied synthetic IPC's are ceramic-metallic composites that contain a hard, thermal resistant ceramic phase toughened by a ductile metal phase. There have been several processes developed to produce ceramic-metallic IPC's, including reactive sintering,[12] combustion synthesis,[15,16] pressurized melt infiltration,[18] liquid displacement reactions,[7,19] robotic deposition,[11] and by combining various techniques.[17] A vast majority of research has been performed on the alumina-aluminum (Al_2O_3-Al) system. The Al_2O_3-Al system is popular because it can be fabricated using in-situ techniques resulting in net-shape or near net-shape products. The net-shape ability combined with the relatively low cost of the aluminum starting material makes this system economically advantageous.[10] Furthermore, the final material properties can be tailored by the addition of inert and/or reactive components without compromising the overall structure. For example, SiC additions can increase the thermal conductivity and overal wear properties of the Al_2O_3-Al system.[25] Al_2O_3-Al based materials are not the only ceramic-metallic IPC's that can be produced, but currently they are the most widely studied.

2.2.1. Literature Relating to the Manufacturing of Ceramic-Metallic IPC's

Henri George's patent[26] published in 1955 describes a method of producing materials that exhibit both ceramic and metallic properties from silica containing compounds. George used the following equation to describe his process: $SiO_2 + M \rightarrow MSi^n + MO_x$, where SiO_2 is combined or free silica, M is any reducing metal, MSi is an alloy of metal M and silicon, *n* indicates that the proportions of M and Si in the alloy are variable, and MO_x is an oxide of the metal M. It is noted that raw silica can be in a combined or uncombined state, meaning that sand, quartz, silica glass, pure fused silica, or any other form of silica can be used. The reducing metal in the patent is primarily described as aluminum; however, other elements including Mg, Na, K, Li, Ca, Ba, and Sr are also listed as viable metals. George states that certain alloying metals, which can be added either to the metal bath or as silicates in the ceramic body, can be used to form interstitial alloys. He also includes the addition of inactive matter, like alumina, as a variation to the process. A temperature range of 700 to 900 °C is listed as satisfactory for the reaction, and temperatures over 1000 °C can be used to increase the size of the alumina grains. George describes successfully transforming various silica objects of different dimensions in aluminum baths. The resulting products preserved the original object's shape and geometry and contained approximately 80% alumina and 20% aluminum-silicon alloy. Thus, Henri George's patent was the first to describe a net-shape process used to created ceramic-metallic composites. Even though George described these materials as "having high industrial value in many fields," there were no significant publications regarding ceramic-metallic composites for many years.

By the 1970's the two dominant means of producing ceramic-metallic composites were powder metallurgy techniques and liquid metal infiltration. Powder metallurgy techniques involve cold-pressing, hot-pressing, or sintering mixtures of ceramic and metallic powders or particles. Liquid-metal infiltration utilizes a pre-fabricated porous ceramic preform that is infilitrated by a liquid metal. Both methods are limited by shape and size restrictions, discontinuity of phases, low obtainable ceramic volume, and relatively high final porosity.[27] During the ensuing decades there were several attempts to address these quality issues, including efforts to utilize fibrous mats,[28] applied pressure,[29] wetting agents,[30-31] and applied vacuum.[32] However, these methods still had shortcomings and there existed a need to process ceramic-metallic composites more simply and reliably.

In 1986, a technique to create ceramic-metallic composites commonly referred to as the Lanxide process was patented by Newkirk *et al.*[33] The Lanxide process, named for the company who owns the patent, is used to create alumina-aluminum and aluminum-nitride-aluminum composites. The process begins by heating a metal with one or more surfaces exposed to a vapor-phase oxidizing environment, usually aluminum in air. The temperature range of the reaction is described as greater than the melting point of the metal but lower than the melting point of the oxidation product. Initially, a pool of liquid metal on the exposed surface will react with the oxidizing vapor to form a layer of the oxidation product, which is alumina in the aluminum/air system. As the process continues, molten metal is pulled through newly forming micro-sized channels in a manner similar to capillary action. The molten metal will continue to react with the oxidizing vapor as long as both are in supply and the temperature is within the necessary range. This results in a directionally grown ceramic network. The ceramic network contains a percentage of voids that can be partially or nearly completely filled with metal. Processing conditions such as temperature, time, and type of metal determine the porosity percentage. The final product contains a ceramic phase interconnected three-dimensionally and a metal phase that is completely or at least partially interconnected. It has been shown that adding dopants, such as magnesium and zinc, can initiate ceramic growth, enhance metal transport, and improve the growth morphology of the oxidation product. Other metals besides aluminum are covered by the patent and include silicon, tin, titanium, and zirconium. However, there does not appear to be any research using these materials in the Lanxide process.

Michael Breslin published a patent[34] in 1993 that is similar to the process described by George in 1955. The patent explains a method for making ceramic-metallic composite bodies by a non-vapor oxidation method, as to distinguish it from the Lanxide process. The process involves submersing a sacrificial ceramic preform into a molten metal bath. This process produces a net-shape composite based on the preform's geometry that contains one or two continuous phases. It is noted that the preferred preform/metal pair is silica and aluminum, but other combinations can be used. The patent also includes the addition of reactive or inert additions to the system, such as titania, zirconia, alumina, silicon nitride, and silicon carbide among others. The temperature range for this process is listed as 1000 to about 1250 °C, and an increase in reaction rate is correlated to an increase in temperature. Embodiments of the process produced co-continuous ceramic-metallic composites that were approximately 70% alumina and 30% aluminum metal. The patent also includes a formation mechanism, theories on how to alter the process, and various measurements of physical properties. There is great effort to distinguish this process from that of Newkirk's,[33] but there was no attempt to differentiate it from the George[26] process.

Two years later, Breslin *et al.*[19] published their findings on producing co-continuous ceramic composite (C4) materials synthesized by the liquid displacement reaction described in his patent. Near net-shape composites containing approximately 65% Al_2O_3 and the remainder being Al were obtained by immersing high purity SiO_2 rods into a molten aluminum bath. It was found that the most desirable products, which contain an α-Al_2O_3 (corundum) network, were obtained by transformation temperatures exceeding 1000 °C. In addition, the research confirmed that the transformation rate increases as temperature increases. A proposed mechanism of formation explains that as the SiO_2 precursor is submerged in the molten aluminum bath, a liquid phase displacement reaction results in a layer of Al_2O_3 on the surface. The Al_2O_3 experiences an approximate 35% volumetric contraction and cracking occurs. The molten Al flows through the cracks allowing the reaction to continue. The Si remaining from the reaction dissolves into the aluminum and diffuses away from the reaction front and into the aluminum bath. During cooling, the Si remaining in the aluminum channels becomes supersaturated and precipitates out. The resulting materials exhibit excellent mechanical properties and microstructural stability at elevated temperatures. TEM analysis showed that the two phases are strongly bonded in a faceted nature that has the effect of mechanical keying. However, the mechanical property tests had poor reducibility and explanation was left to future work.

Feng and Moore[15] described an *in situ* combustion synthesis technique for producing ceramic-metal IPCs in 1995. They used the overall reaction $3TiO_2 + 3C + (4+x)Al + yAl_2O_3 \rightarrow 3TiC + (2y)Al_2O_3 + xAl$ as the basis for their experiment. A combustion technique called self-propagating high-temperature synthesis (SHS) was employed. The reactants are packed into a pellet which is then heated to ignition temperature. The exothermic reaction produces enough energy to sustain the reaction until the powders are transformed into a ceramic-metal IPC. Previous to this research, SHS has produced IPCs with high porosity. Feng and Moore were able to produce high density IPCs by applying a compressive load to the pellet either prior to or immediately after the SHS initiation. The pressure allows the Al metal to rapidly infiltrate the ceramic network and produce a dense composite in a relatively short amount of time. This alternative method is energy efficient but limits the size and shape of the product.

In 1998, Zhou *et al.*[17] produced and examined interpenetrating phase composites by a two step-process consisting of self-propagating synthesis and pressurized metal infiltration. TiC-Al_2O_3 green pellets, used as preforms, were made by self-propagating high temperature synthesis (SHS) under a constant pressure load. Volatile agents were added to the starting mixture to increase the preforms' open porosity allowing for better infiltration. The preforms were infiltrated by pure Al and 2024 Al alloy at 750 °C under 9 MPa of nitrogen. The resulting materials were tested using three-point bending and exhibited unimpressive strength. This was contributed to the relatively low gas pressure of the furnace, limited to 9 MPa, which was not high enough to cause complete infiltration of the open pores. Additionally, it was noted that the strengths of the preforms were significantly decreased due to their high porosity.

In 2003, Marchi *et al.*[11] explored the possibility of making Al-Al_2O_3 IPC's by infiltrating a 3-D periodic ceramic preform produced by robotic deposition. Freeform fabrication allows layer-by-layer construction of complex 3-D ceramic preforms using fused deposition and direct-write methods. Marchi *et al.* constructed an alumina preform with periodic cubic symmetry via robotic deposition of an Al_2O_3-5%ZrO_2 gel. The preform had nominal dimensions of 6 mm × 4 mm × 4 mm and consisted of 30 layers of equidistant parallel rods connected at the ends by hair pins. Each layer was rotated 90° to produce vertical columns and horizontal spans. It was determined through helium pycnometry that the alumina network had a closed porosity as high as 9%. Closed porosity refers to isolated pores contained within the alumina phase that cannot be infiltrated. 99.99% pure aluminum was used to infiltrate the network under 3.5 MPa of argon gas at 750 °C. The resulting composite was calculated to be 70% ceramic by volume and the remainder aluminum. Mechanical testing yielded compressive strength values lower than IPCs produced by displacement reactions. The discrepancy in strength is attributed to the finer microstructure and significant amounts of silicon present in IPCs resulting from displacement reactions.

In 2007, Hu *et al.*[16] tried to improve the self-propagating high-temperature synthesis (SHS) used to produce TiC-Al_2O_3-Al composites by utilizing a method referred to as field-activated combustion synthesis (FACS). FACS uses an external electric field to activate self-propagating reactions. The main focus was to establish a means of incorporating more excess aluminum into the reaction. In previous research, the energy required to melt the excess aluminum limited the amount that could be used in self-propagating reactions. A reaction with more aluminum available to infiltrate the ceramic matrix could result in a denser product. It was found that the added electric field provides the necessary energy to overcome the thermodynamic limitation of SHS. The results showed that density improved and TiC and Al_2O_3 grain sizes reduced with increasing field strength. For example, a field strength of E=25 V cm^{-1} produced a TiC-Al_2O_3-Al composite with a relative density up to 92.5% and TiC and Al_2O_3 particles on the scale of 0.2-1.0 μm. FACS eliminates the need for mechanical pressure or processing and is more energy efficient than the SHS process alone.

2.2.2. Applications of Ceramic-Metallic IPC's

The improved thermal stability and corrosion resistance of ceramic-metallic IPC's has sparked interest in the field of refractory shapes used for handling molten metal and glass.[10] Containment materials applied in refractory settings experience extreme conditions that contribute to erosion, corrosion, and wear. The ensuing breakdown of refractory linings results in decreased thermal efficiency, decreased product quality, and production outages due to repair and maintenance.[35] Ceramics can contribute the necessary performance at elevated temperatures, while ductile metals improve overall durability. For this reason, ceramic-metallic IPC's are currently being developed and implemented as containment applications for handling high temperature molten metals. For example, Fireline TCON, Inc. (FTi) has developed an Al_2O_3-Al IPC that contains SiC particles having an approximate composition of 53 wt.% SiC, 35 wt.% Al_2O_3, and 12 wt.% Al for the handling of molten aluminum. The material was shown experimentally to exhibit improved resistance to wear and corrosion over traditional materials, and is being market by FTi in partnership with Rex Materials Group.[35]

A future market for IPC’s is in automotive braking components. For the past 50 plus years gray cast iron has been the choice material for automotive brake rotors. Cast iron has many benefits that include cost effectiveness, wear resistance, and fairly good thermal conductivity. However, these benefits come at the cost of weight. Ceramic-metallic IPC’s currently being developed possess similar wear properties and thermal resistance as cast iron, but are substantially lighter in weight. These advantages can improve overall performance, reduce life-cycle costs, and improve vehicle fuel consumption.[25] Though the initial cost to replace cast iron components with ceramic-metallic material might be high, the long-term savings due to reduced fuel usage and extended life-cycle is something that has piqued the interest of researchers and industry, alike.

A third potential market is in the field of military body and vehicle armor. Required body armor for a U.S. soldier weighs between 25 and 40 pounds depending on the amount of coverage.[36] Not only does the added weight decrease mobility, it can lead to long-term musculoskeletal and peripheral nerve injuries.[37] Weight also reduces the efficiency of military vehicles and weapons systems, which prevents rapid deployment of military contingencies.[38] IPC’s can offer similar or improved protection compared to traditional armor material, but with substantial weight savings. For example, it has been shown that SiC based ceramic armor weighs 55% less than steel plating of the same size.[36] Compared to lightweight, flexible body armors made from interwoven fibers, such as Kevlar®, IPC based armor does not suffer from moisture sensitivity and limited life-span.[39] A successful commercialization of such composites can expand their use to police and firefighting forces.[10]

2.3. The TCON Process

The materials studied in this report were produce by the TCON process, depicted in Fig 2-1. The TCON process is a unique reactive metal penetration (RMP) process developed by Fireline TCON Inc. (FTi) located in Youngstown, OH. It is similar to methods reported by George[26] and Breslin[34], but utilizes carefully controlled processing parameters to achieve high quality ceramic-metallic IPC's.[24] The TCON process involves submerging a ceramic preform into a molten metal or molten alloy bath for a given length of time. During submersion, chemical reactions transform the preform into a ceramic-metallic composite. An example of the TCON process is the transformation of clear fused quartz in an aluminum bath, described in Eq. 1-2. The process results in a net-shaped Al_2O_3-Al composite based on the original preform's dimensions and geometry. Both the Al and Al_2O_3 phases are continuous and interconnected throughout the three-dimensional network. For these particular materials the transformation rate is approximately 2mm/hr at 1200 °C.[8] The resulting microstructure is within the range of approximately 100 nm to several micrometers.[10]

The TCON process is not limited to the basic Al_2O_3-Al system previously mentioned. A variety of preform materials can be successfully transformed and can contain either reactive or inert additions, see Eq. 1-2. For example, polycrystalline silica or clay preforms can be used instead of clear fused quartz.[8] In addition, alloying elements added to the molten metal bath can change transformation rates and/or form intermetallic compound phases.[7,14] The capability of altering RMP parameters allows FTi to produce materials that have significantly different properties than traditional ceramic-metallic composites.

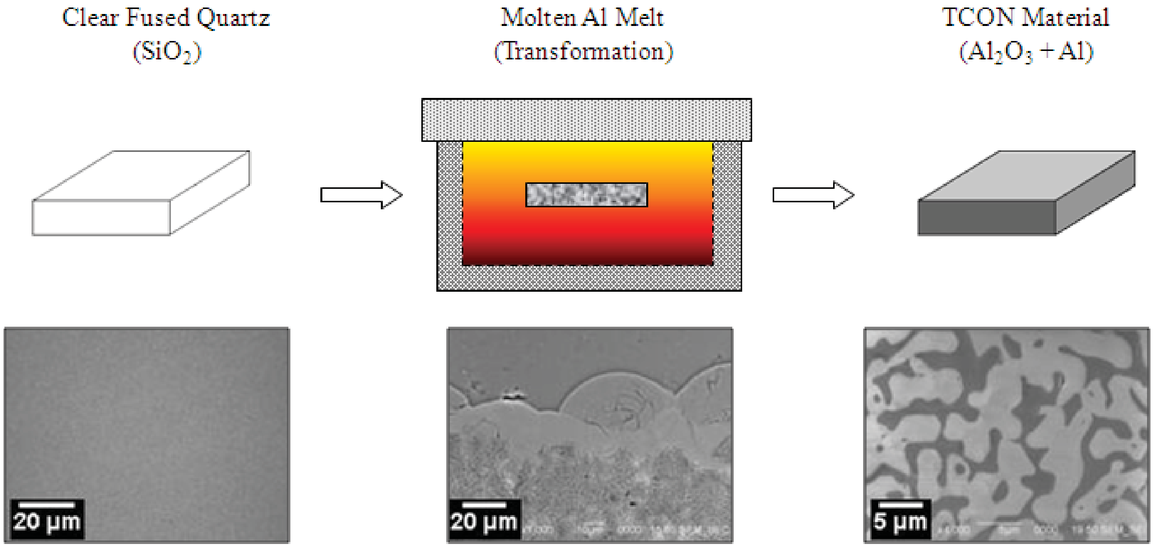

Fig. 2-1: An example of the TCON process showing the transformation of clear fused quartz into a ceramic-metallic IPC. The microstructure of the material at each stage is shown. The clear fused quartz preform originally has a homogeneous structure. The preform is submerged into a molten Al melt (≈1200 °C) and chemical reactions take place. The transformation rate is approximately 2mm/hr. After complete transformation, the materials are removed from the bath and allowed to cool to room temperature. The final product is a 3D interpenetrating network of Al_2O_3 and Al phases. Note that the product maintains the original geometry of the preform.

2.3.1. Conditions for IPC Formation

The reaction between aluminum and silicon dioxide that drives the TCON process is classified as a thermite reaction. Thermite reactions are highly exothermic and involve a metal reacting with a metallic or non-metallic oxide to produce a more stable oxide and the corresponding metal or non-metal from the reactant oxide, described by Eq. 1-1.[22] The ability to produce an IPC from a thermite reaction, such as the one between Al and SiO_2, is rare. Typically, the exothermic properties of a thermite reaction make it impossible to predict the structures or even the compositions of the final products.[23] In fact, the heat generated by most aluminum-oxide thermite reactions is enough to increase the temperature above the melting point of both products. For example, the reaction between aluminum and iron oxide (Fe_2O_3) produces a theoretical adiabatic temperature, which assumes no heat loss to the environment, of 3349 °C.[22] The Al-Fe_2O_3 reaction, which is commonly known as *the* thermite reaction, has been used as a welding technique for railroad joints,[40] in the treatment of steel by-products,[41] and to produce ceramic linings inside steel pipes via centrifugal force.[42] However, the speed and intensity of the reaction makes it extremely difficult to manage or form a product with a controlled microstructure.[43] By contrast, it is extremely difficult to produce any reaction between zinc oxide and molten aluminum.[44] The reaction between Al and SiO_2 is favorable for the formation of IPC's because it proceeds slowly and has an adiabatic temperature of 1487 °C,[22] which is lower than the melting point of Al_2O_3. This makes the Al-SiO_2 reaction more manageable than most thermite reactions, but is not the only reason it forms an IPC.

In 1996, a report by Lui and Köster[21] outlined the criteria for forming IPC's by the immersion of dense sacrificial oxide preforms into molten metal. The report lists three requirements for the formation of oxide-metal composites that contain interpenetrating microstructures: 1) the produced oxide must have a smaller volume than the sacrificial oxide, 2) the produced oxide must be more stable than the sacrificial oxide, which means that the free energy of formation, ΔG, of the product oxide must have a more negative value than that of the sacrificial oxide at the transformation temperature, and 3) the processing temperature must be higher than the melting point of the reductive metal but lower than its boiling point, and it must be lower than the melting point of both the sacrificial and product oxides. The report concludes that Al_2O_3-Al IPC's can be manufactured by reacting aluminum with a number of different oxides at 1273 K and 2073 K, and that several other ceramic-metal IPC combinations can be produced at the same temperatures. However, details including material properties, free energy of formation values, and calculations were not provided. The following shows that the Al-SiO_2 reaction will produce an IPC according to the above criteria.

Criterion 1

From Table 2-5, the molecular weight of SiO_2 = 60.08 g/mol, the molecular weight of Al_2O_3 = 101.96 g/mol, the density of SiO_2 = 2.2 g/cm^3, and the density of Al_2O_3 = 3.98 g/cm^3. Taking a 100 gram basis of SiO_2 and an excess of Al for the reaction in Eq. 1-2, the following calculations can be made:

Volume of SiO_2:

$$(100\ \mathrm{g\ SiO_2})\left(\frac{\mathrm{cm^3}}{2.2\ \mathrm{g\ SiO_2}}\right) = 45.5\ \mathrm{cm^3}$$

Volume of Al_2O_3:

$$(100\ \text{g SiO}_2)\left(\frac{1\ \text{mol SiO}_2}{60\ \text{g SiO}_2}\right)\left(\frac{2\ \text{mol Al}_2\text{O}_3}{3\ \text{mol SiO}_2}\right)\left(\frac{102\ \text{g Al}_2\text{O}_3}{1\ \text{mol Al}_2\text{O}_3}\right)\left(\frac{\text{cm}^3}{3.98\ \text{g Al}_2\text{O}_3}\right) = 28.5\ \text{cm}^3$$

Therefore, the volume of the product oxide (Al_2O_3) is smaller than the volume of the sacrificial oxide (SiO_2) and the first criterion is met.

Criterion 2

From Fig. 2-2 it is clear that the free energy of formation is more negative for Al_2O_3 than SiO_2 values given for the temperature range of 250 K and 2500 K. This meets the second criterion for all applicable temperatures.

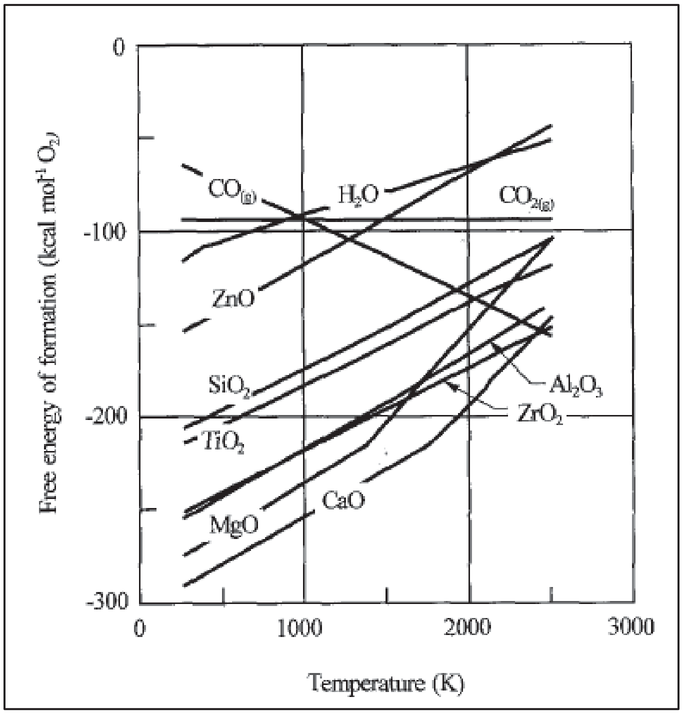

Fig. 2-2: Free energy of formation for oxides.[22]

Criterion 3

From Table 2-2, the melting points of Al, SiO_2, and Al_2O_3 are 660 °C, 1665 °C, and 2030 °C, respectively. From this data, the third criterion is met if:

$660\ °C < \text{Reaction Temperature} < 1665\ °C$.

2.3.2. Transformation Mechanisms

A mechanism explaining the formation of an interpenetrating network from the Al_2O_3-SiO_2 reaction has been proposed by Breslin *et al.*[19]. The mechanism states: 1) a thin layer of Al_2O_3 forms on the surface of the SiO_2 preform as it reacts with the molten aluminum. 2) Extensive cracking caused by the volumetric contraction of Al_2O_3 phase occurs after the layer reaches some critical thickness. 3) The cracking permits the molten aluminum to further penetrate the SiO_2 and continue the reaction. 4) The Si that is displaced diffuses away from the reaction front through the aluminum channels and into the surrounding bath. According to Breslin, the cracking produced by the volumetric contraction of the product oxide is responsible for the interconnected, three-dimensional microstructure.

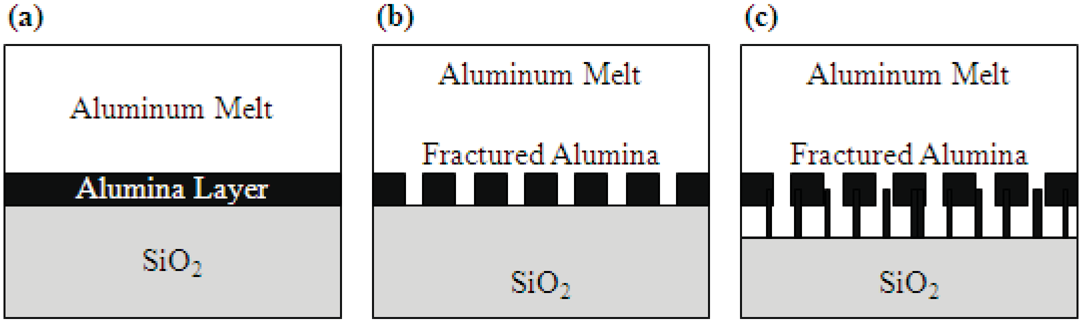

Fig. 2-3: An illustration of Breslin's proposed formation mechanism. (a) Liquid aluminum contacts the SiO_2 preform and an Al_2O_3 layer is formed. (b) At a critical thickness the Al_2O_3 layer cracks allowing liquid Al to transgress and continue the reaction. (c) The reactions continues such that the co-continuity of both phases results. (adapted from Breslin *et al.*[19])

In a study published in 1973, Rapp *et al.*[45] provided a theory to predict the product morphology for displacement reactions between metals and oxides at elevated temperatures (≈1000+ °C). The reaction is listed as $vMe + M_xO \rightarrow Me_vO + xM$, where M and Me are metals and M_xO and Me_vO are their lowest oxides. While the report does not directly address the Al-SiO_2 reaction, it offers an alternative approach to understanding why an IPC can be formed. Rapp provides a quantitative theory, which contains extensive calculations and therefore is not outlined in this body, for determining the arrangement of product phases. The theory states that a layered morphology, see Fig. 2-4(a), or an aggregated morphology, Fig. 2-4(b), will form depending on the limiting factor for the growth of the product oxide phase (Me_vO). According to the theory, the initial reaction interface is assumed to be uneven. Relating to Fig. 2-5, if the growth of the Me_vO phase is limited by the cation diffusion through the Me_vO phase, the flux of cations will reach point 1 before point 2. This will flatten the reaction interface and form a layered morphology. On the other hand, if the growth of the Me_vO phase is limited by the transport of oxygen through the metal phase (M), the flux of oxygen reaching point 2 will exceed that of point 1. In this case, the rapid growth at point 2 will cause a serrated interface and an aggregated morphology will form. In the report, Rapp's theory was used to successfully predict and experimentally prove that at 1000 °C Ni-Cu_2O and Co-Cu_2O reactions produce layered product phases. It also proved that at the same temperature Fe-Cu_2O and Fe-NiO reactions result in aggregated product phases. Furthermore, it was shown that the Fe-NiO reaction's main products, Ni-Fe alloy and FeO, were completely interwoven and continuous. In addition, selective etching and polarized light microscopy were used to detect a thin band of nickel ferrite, $NiFe_2O_4$, at the reaction front. Rapp classified this product morphology as the "interwoven-aggregate arrangement," a precursor to what is now known as an interpenetrating phase composite.

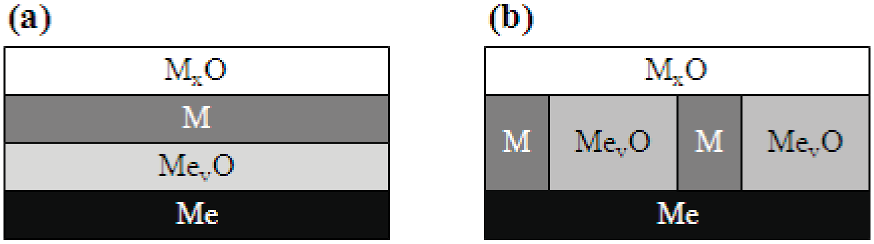

Fig. 2-4: (a) Illustration showing a layered morphology in which the phases form on top of each other. (b) Illustration of an aggregated morphology in which the phases form adjacent to one another. (adapted from Rapp *et al.*[45])

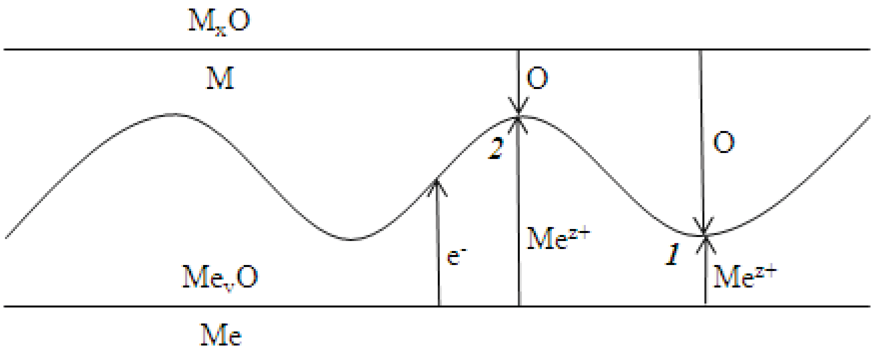

Fig. 2-5: Schematic showing the reaction interface between a metal (Me) and oxide (M_xO) that produces a product metal (M) and oxide (Me_vO). The reaction is assumed to have an uneven interface. If the reaction rate is limited by the diffusion of Me through Me_vO, then the Me^{z+} cations will reach point 1 first and a layered morphology results. If the reaction rate is limited by the transportation of O through the metal, then the flux of O arriving at point 2 is greater than at point 1 and an aggregated morphology results. (adapted from Rapp *et al.*[45])

2.3.3. RMP Temperature Considerations

Typically, the TCON process is conducted at approximately 1200 °C.[24] This temperature is chosen to ensure that the α-Al_2O_3 (corundum) phase will be the product ceramic phase. Corundum is the only stable Al_2O_3 phase at all temperatures below its melting point. Other phases of Al_2O_3 are either unstable or metastable.[47] Unstable phases are those that are thermodynamically and kinetically unstable and therefore decompose into other compounds. Metastable phases can be explained as being less thermodynamically stable than the stable state, but kinetically stable and maintaining an internal equilibrium under the conditions employed.[48] For example, the FeC phase in the Fe-C system will decompose into graphite and iron under conditions that are favorable for true equilibrium, but it exists as a metastable phase because the decomposition is kinetically hindered, *i.e.* it is so slow that it is imperceptible.[49]

Previous research has shown that RMP reaction temperatures above 1000 °C result in the desirable α-Al_2O_3 phase. At reaction temperatures below 1000 °C, an extremely fine microstructure of the metastable monoclinic θ-Al_2O_3 phase forms. The formation of θ-Al_2O_3 has a detrimental effect on the mechanical properties of the composite.[19] A transition of tetragonal γ-Al_2O_3 to α-Al_2O_3 in the temperature range of 1000-1050 °C has been observed in the synthesis of alumina powders by polymeric precursors.[50] Analytical calculations using the density functional theory have also shown that the metastable (γ, δ, θ)-Al_2O_3 phases transition to the α-Al_2O_3 phase at temperature in excess of 1000 °C.[51,52] The temperature range of 1200 °C was chosen for manufacturing TCON materials to avoid the formation of thermodynamically unstable Al_2O_3 structures.

Table 2-1: Stable and Metastable Alumina Phases

Phase	**Stability**	**Lattice Parameters (Å)**	**Space Group**	**Crystal Structure**
α[44]	Stable	a = 4.751 c = 12.92	$R\overline{3}c$	Trigonal
θ[47]	Metastable	a = 11.85 b = 2.904 c = 5.622 β = 103.8°	$C2/m$	Monoclinic
γ[47]	Metastable	a ≈ 7.9	$Fd\overline{3}m$	(Defect Cubic Spinel)
δ[53] (1)	Metastable	a ≈ 7.9 b ≈ 15.8 c ≈ 11.85	$P2_12_12_1$	Orthorhombic
δ[53] (2)	Metastable	a ≈ 7.9 c ≈ 23.7	$P4_1$	Tetragonal

2.4. Iron Additions to the RMP Process

As previously mentioned a third phase added to the basic Al_2O_3-Al system can contribute its own unique mechanical characteristics and/or alter the structure of the Al_2O_3-Al network. The effects of adding 7.5wt.% iron to the molten aluminum bath during RMP processing are studied in this work. A major reason to add Fe to the system is to increase overall strength at elevated temperatures. There are advantages Fe has over other metals for this task.[14] 1) Fe has a higher melting point than Al. 2) Fe has a lower affinity for O than Al and therefore does not hinder the reaction by forming an oxide itself. 3) Handling of molten Al and Fe is relatively easy compared to metals or alloys that require strict atmospheric control, such as Ti. 4) Fe is an abundant resource available at a comparatively low price.

Based on the known criteria for oxide/metal composite formation, Fe will not react with SiO_2 to form an oxide during the RMP processing.[21] However, iron is likely to react with the displaced silicon within in the aluminum channels to form Al-Fe-Si intermetallic compounds. It is widely accepted that Fe is the most common impurity in Al-Si foundry alloys.[54-58] Iron contamination in Al-Si systems can lead to both stable and meta-stable phases. Some stable Fe-containing compounds known to form during Al-Si alloying include Al_3Fe, Al_8Fe_2Si, and Al_5FeSi.[59] Since the TCON process provides an environment abundant in Al and Si at elevated temperatures, it is possible that adding Fe to the system will form these or other Al-Fe-Si intermetallic compounds within the structure. It is also possible that Fe additions will have an either desirable or detrimental effect on the overall Al_2O_3-Al structure. The lack of research regarding this topic emphasizes the importance of this work in understanding the effect alloying Fe has on the RMP process.

2.4.1. Literature Relating to Al/Al-Fe alloy-Al_2O_3 IPC's

There are few documented attempts to add iron or iron-aluminum phases to the Al_2O_3-Al co-continuous structure. Some attempts to create in-situ IPC composites containing Al, Al_2O_3, and Al-Fe alloys by means of reactive sintering have been reported.[13,60,61] However, studies using reactive sintering are extremely limited in their usefulness for understanding TCON materials because the mechanisms of RMP processing are drastically different. Currently, there are few documented studies that use Fe as an alloying agent in the TCON or other RMP processes.

A study examining metal-ceramic composites consisting of Al-Fe alloy and Al_2O_3 was performed by Yoshikawa *et al.* in 2003.[14] Composites were created via reactive metal penetration by immersing SiO_2 rods into metal baths containing various concentrations of iron and aluminum. The reaction temperatures were set at 1200 °C and 1300 °C. The resulting materials were reported as co-continuous ceramic composites (C^4) containing an Al_2O_3 ceramic phase and Al/(Al-Fe-alloy) metal phase. Compared with similarly transformed Al/Al_2O_3 composites, an increase in starting Fe content produced a decrease in growth rate and a finer microstructure. It is suggested that the growth rate is slower because the addition of Fe increases the viscosity of the molten Al. Therefore, it cannot flow as rapidly through the Al_2O_3 network to continue the reaction. Yoshikawa also suggests that the rate Si diffuses away from the reaction interface decreases because of an interaction between Si and Fe, though there is little evidence to support this claim. EDS analysis showed that that the Si is segregated in the Fe-rich regions. It was also suggested that the finer Al_2O_3 network restricts the flow of Al to the reaction interface, though there was no conclusion as to why the network became finer. Yoshikawa's attempt to make intermetallic composites containing high volumes of FeAl or Fe_3Al was largely unsuccessful due to a poor growth rate and low final Fe content. It was proposed that a two step immersion process in which a SiO_2 perform is first converted into an Al/Al_2O_3 composite and then into a $Fe\text{-}Al/Al_2O_3$ composite would produce the desired results.

Ryan Paul's master's thesis, conducted at Youngstown State University and published in 2007,[8] studied IPC's produced using TCON's RMP process. Five 10 mm diameter clear fused quartz rods were transformed in molten metal baths that contained varying amounts of Al, Si, and Fe. All five samples were transformed at 1200 °C for 20 to 22 hours under the same the same processing conditions. Two of the five composites contained iron in the molten bath, both of which maintain the basic Al_2O_3 structure. The first was transformed in an 85wt.%Al-15wt.%Fe metal bath. The resulting microstructure contained two distinct regions, an inner core approximately half the diameter of the rod and a surrounding outer case. The inner core appeared to have a coarser microstructure, while the outer case had a radially orientated Al_2O_3-Al structure. Both regions contained intermetallic-compounds that formed long vermicular formations in the metal fraction of the composite. The second material was transformed in a 66.5wt.%Al-26wt.%Si-7.5wt.%Fe metal bath. The microstructure contained no variations or layers and was similar to that of the inner core of the first iron-containing sample. The intermetallic-compound formations observed in the first sample were present. No observed orientation of the phases was reported for this sample. Powder XRD analysis showed the presence of intermetallic-compounds in the first iron containing sample but could not confirm the exact compound or compounds. The diffraction pattern for the second sample matched an Al_9FeSi_3 intermetallic-compound.

In a 2010 report released by Oak Ridge National Laboratory in coordination with Fireline TCON, Inc., Hemrick *et al.*[10] investigated nine TCON materials including two that are identical to the ones studied in this thesis. The other TCON materials varied in preform material, metal bath composition, and transformation time. Four-point bending tests were used to determine the mechanical properties of the composites. It was determined that the clear fused quartz preform transformed in Al-7.5wt.%Fe possessed the greatest flexural strength, approximately 240 MPa with a standard deviation of 34.74 MPa. The flexure strength of the standard Al transformation is reported as approximately 170 MPA with a standard deviation of 24.77 MPa. TEM analysis of this sample showed micron sized alumina grains and Al-Fe intermetallic phases with nano-scaled features. Since the materials in question are identical, this body of work looks to confirm and expand upon the information provided by Hemrick *et al.*

2.4.2. Alloying Aluminum with Iron and Silicon

It is well known that iron is the most common impurity in aluminum. Intentional additions of iron to aluminum alloys are usually less than 1% and are used to increase strength and creep characteristics at moderately elevated temperatures. Iron is also known to reduce grain size in wrought products. At high temperatures iron is highly soluble in molten Al, but at room temperature the solubility is very low (~0.4%).[62] Alloys that are Al-rich are most often characterized by the eutectic reaction: L → Al + Al_3Fe,[59] see Fig. 2-6. It is important to note that Al_3Fe has become analogous to $Al_{13}Fe_4$ in the literature and the two are often used interchangeably.[63,64] In rapidly cooled alloys, a metastable Al_6Fe compound is produced.[58]

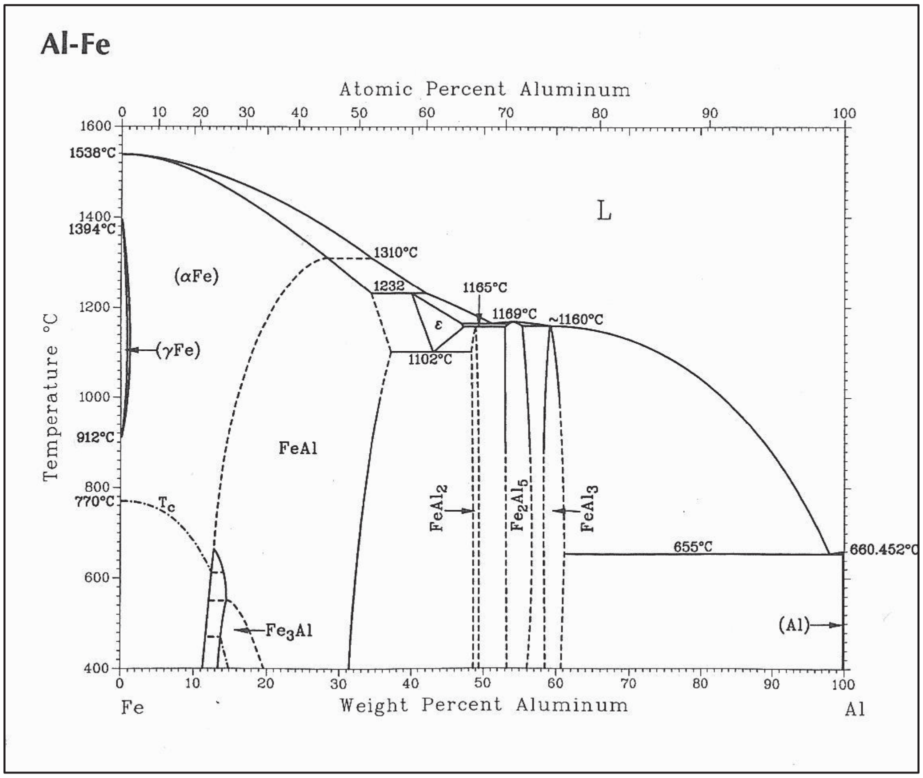

Fig. 2-6: Al-Fe binary phase diagram.[48]

Silicon is the second most common impurity in aluminum. Si additions to Al increase corrosion resistance and can reduce cracking when alloyed with other elements.[62] Al-Si alloys have excellent flow characteristics and are used for forging complex shapes.[57] At 577 °C, which according to Fig. 2-7 is the systems eutectic temperature, the maximum solubility of Si in Al is approximately 1.5 ± 0.1 at.% and solubility decreases with temperature.[63] At 300 °C, the solubility of Si in Al is only 0.05 at.% resulting in the precipitation of essentially pure Si particles.[56] As pure Al cools it undergoes a 6.6% volumetric contraction. In Al-Si alloys, the addition of Si has been shown to reduce the overall volumetric contraction of the system. For example, the volumetric contraction of Al-12wt.%Si alloy during solidification is 3.8%.[65]

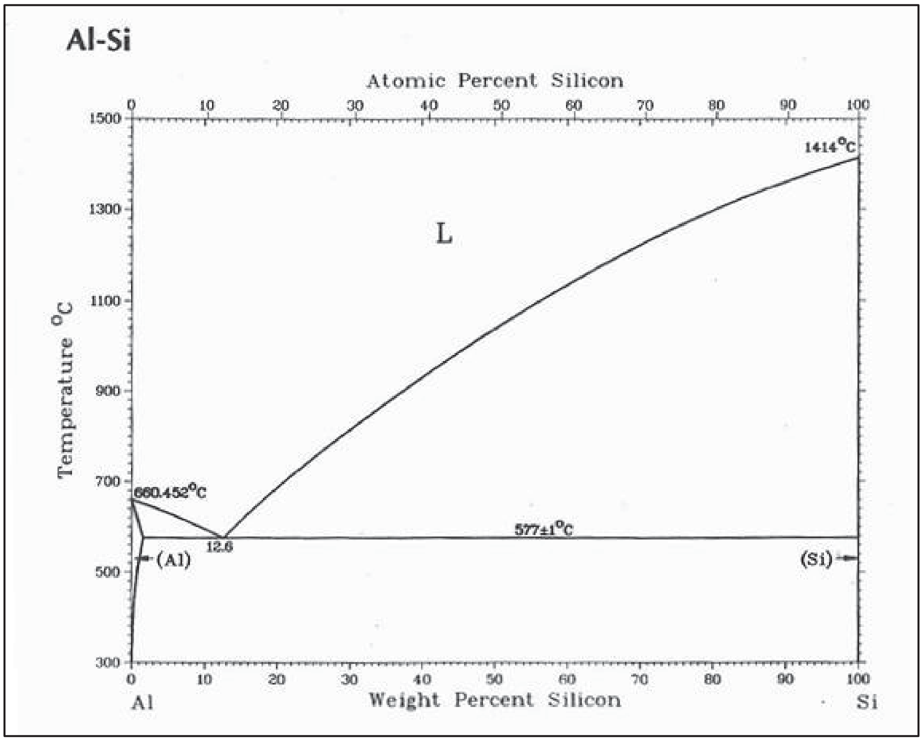

Fig. 2-7: Al-Si binary phases diagram.[48]

The Al-Fe-Si ternary system is very complex and not fully understood. Most of the related research focuses on the effects of Fe and Si impurities during aluminum processing. In dilute Al-Fe-Si alloys, it has been shown that θ-$Al_{13}Fe_4$ is the dominant precipitate at slow cooling rates.[56] The most widely accepted stable ternary compounds are the α-Al_8Fe_2Si and β-Al_5FeSi phases, though their exact composition are debatable.[66] Most commercially produced alloys are not in equilibrium and several phases, such as Al_6Fe, Al_3Fe, Al_8Fe_2Si, Al_6FeSi, Al_4FeSi_2, and Si, are produced and coexist with one another.[59] Composition and lattice parameters of pure Al, Fe, and Si are given in Table 2-2 and several known intermetallic Al-Fe-Si binary and ternary compounds are given in Tables 2-4 and 2-5.

Table 2-2: Crystal Structure and Lattice Parameters of Pure Metals (Room Temperature)

Phase	**wt.%Al**	**wt.%Fe**	**wt.%Si**	**Space Group**	**Lattice Parameters (Å)**
PURE METALS					
Al[62]	100	0	0	$Fm\overline{3}m$	a = 4.04958
Fe[62]	0	100	0	$Im\overline{3}m$	a = 2.8665
Si[62]	0	0	100	$Fd\overline{3}m$	a = 5.4310

Table 2-3: Crystal Structure and Lattice Parameters of Common Al-Fe and Al-Si Binary Phases

Phase	**wt.%Al**	**wt.%Fe**	**wt.%Si**	**Space Group**	**Lattice Parameters (Å)**
Al-Fe BINARY					
Al_6Fe[67]	≈13 to ≈20	≈80 to ≈87	0	*Cmcm*	a = 6.49 b = 7.44 c = 8.79
ε[48]	≈40 to ≈47	≈53 to ≈60	0	-	-
AlFe[68]	12.8 to ≈37	68	0	$Pm\bar{3}m$	a = 2.895
Al_5Fe_2[69]	53 to 57	43 to 47	0	*Cmcm*	a = 7.65 b = 7.41 c = 4.22
Al_3Fe[70]	58.5 to 61.3	38.7 to 41.5	0	*C*2/*m*	a = 1.549 b = 8.08 c = 12.48 β = 107.72°
Al-Si BINARY					
(Si doped) Al[48,62]	98.4 to 100	0	0 to 1.6	$Fm\bar{3}m$	a = 4.0496
(Al doped) Si[48,62]	0 to 0.01	0	99.99 to 100	$Fd\bar{3}m$	a = 5.4310

Table 2-4: Crystal Structure and Lattice Parameters of Common Al-Fe-Si Ternary Phases

Phase	**at.%Al**	**at.%Fe**	**at.%Si**	**Space Group**	**Lattice Parameters (Å)**
$Al_{4.5}FeSi$[68] [β or τ_6]	69.2	15.4	15.4	*A*2/*a*	a = 12.404 b = 6.175 c = 20.813 β = 90.42°
$Al_2Fe_3Si_3$[68] [τ_1]	25.0	37.5	37.5	$P\overline{1}$	a = 4.6512 b = 6.3261 c = 7.499 α = 101.375° β = 105.923° γ = 101.237°
$Al_{2.7}FeSi_{2.3}$[68] [δ or τ_4]	45.0	16.7	38.3	*I*4/*mcm*	a = 6.07 c = 9.50
Al_2FeSi[68] [τ_{23}]	50.0	25.0	25.0	*Cmma*	a = 7.995 b = 15.162 c = 15.221
$Al_2Fe_3Si_4$[68] [τ’]	22.2	33.3	44.4	*Cmcm*	a = 3.6687 b = 12.385 c = 10.147
$Al_4Fe_{1.7}Si$[68] [τ’’]	59.7	25.4	14.9	*P*6$_3$/*mmc*	a = 7.509 c = 7.594

2.5. Physical and Mechanical Properties of Select Materials

Table 2-5: Mass and Thermal Properties of Select Compounds

	Aluminum[62]	**Iron**[62]	**Silicon**[62]	**Fused Silica**[72]	**99.9% Al_2O_3**[72]
Atomic Weight (g/mole)	26.91541	55.847	28.08	60.08	101.96
Density (g/cm^3)	2.6989	7.87	2.329	2.2	3.98
Melting Point (°C)	660.4	1538	1414	≈1665	2072
Boiling Point (°C)	2494	2870	3145	2230	2977
Thermal Conductivity (W/m K)	247	80.4	185.7	1.4	39

Table 2-6: Mechanical Properties of Select Materials at Room Temperature

	Al-1100[72] (99.0% Al min)	**Al-4032**[62] (12.2% Si, 1% Mg, 0.9% Cu, 0.9% Ni)	**Al-356.0**[72] (7% Si, 0.3% Mg)	**Fused Silica**[72]	**99.9% Al_2O_3**[72]
Yield Strength (MPa)	117 H14 temper	315 T6 temper	124 As cast	-	-
Tensile Strength (MPa)	124 H14 temper	380 T6 temper	164 As cast	104	282-551
Percent Elongation	15 H14 temper	9 T6 temper	6 As cast	-	-
Modulus of Elasticity (GPa)	69	79	72.4	380	73
Poisson's Ratio	0.33	0.33	0.33	0.17	0.22

H14 – strain-hardened by cold working
T6 – heat treated using solution and artificial aging

Chapter 3: Experimental

3.1. Material Acquisition

Fireline TCON, Inc. provided two ceramic-metallic IPC materials for detailed analysis. The samples were manufactured at the TCON facility (Youngstown, OH) using their unique RMP process. Clear fused quartz preforms with dimensions 2 in. × 2 in. × 0.25 in. were reacted in separate molten metal baths. The first was transformed in commercially pure (>99.9wt.%) aluminum for 6 hours, and the other in an aluminum alloy containing 7.5 percent iron by weight for 4.63 hours. Both metal baths were freshly prepared, meaning they were not used for any previous transformations. The reaction temperature was set at approximately 1200 °C for both materials. After the transformations were complete the samples were removed from the baths and allowed to cool at room temperature. Information regarding the reaction parameters is displayed in Table 3-1.

Table 3-1: Transformation Conditions for Primary TCON Samples

Name	**Starting Material**	**Metal Bath**	**Transformation Time**	**Reaction Temperature**
Al	Clear fused quartz (2 in. × 2 in. × 0.25 in)	Pure Al	6 hours	1200 °C
Al-7.5wt.%Fe	Clear fused quartz (2 in. × 2 in. × 0.25 in)	Al - 7.5 wt.% Fe alloy	4.63 hours	1200 °C

Three supplementary samples were provided by FTi for examination. Information pertaining to these samples is displayed in Table 3-2. The first material is a piece of Al-7.5wt.%Fe alloy melt collected from the RMP process used to transform the Al-7.5wt.%Fe sample, see Fig. 3-3(a). The sample is residual alloy that was removed from the surface of the Al-7.5wt.%Fe sample during cooling. The melt sample is an approximate 3.5 cm × 3 cm × 1 cm volume that is flat on the side that was in contact with the Al-7.5wt.%Fe sample. The second sample is a TCON material manufactured by the same RMP process as the Al and Al-7.5wt.%Fe samples. In this case, a 2 in. × 2 in. × 0.25 in. clear fused quartz preform was reacted in an aluminum alloy containing 25 percent silicon by weight for 6 hours. The third sample is a TCON material that was stopped short of complete reaction, shown in Fig. 3-3(b). For the third sample, a 150 mm × 8 mm × 6 mm clear fused quartz preform was transformed in commercially pure Al for 2 hours. This left the sample approximately 90 percent transformed. Again, the same RMP procedure was employed.

Table 3-2:Supplementary Materials

Name	**Description**	**Starting Material**	**Metal Bath**	**Reaction Parameters**
Melt	Residual Al-7.5wt.%Fe alloy	N/A	N/A	N/A
Al-25wt.%Si	TCON Material	Clear fused Quartz (2 in. × 2 in. × 0.25 in)	Al – 25 wt. % Si alloy	Temp = 1200 °C Time = 6 hr
Al(2hr)	TCON Material	Clear fused Quartz (120 mm × 8 mm × 6 mm)	Pure Al	Temp = 1200 °C Time = 2 hr

3.2. Sectioning and Polishing

Samples for various analytical techniques were cut from the original materials. Large specimens were sectioned using a high-speed MARK V CS600-A saw. Subsequent sectioning was performed using a variable speed Buelher IsoMet® 1000 Precision Saw. Both saws were equipped with diamond-impregnated cut-off wheels and cooled with water. For comparative purposes, the Al and Al-7.5wt.%Fe materials were sectioned similarly. Fig. 3-1 shows the samples' relative size and the area from which they were acquired. Photographs of the actual samples are displayed in Fig 3-2. In response to the material's unique three-dimensional microstructure, an x-y-z coordinate system was established to document results.

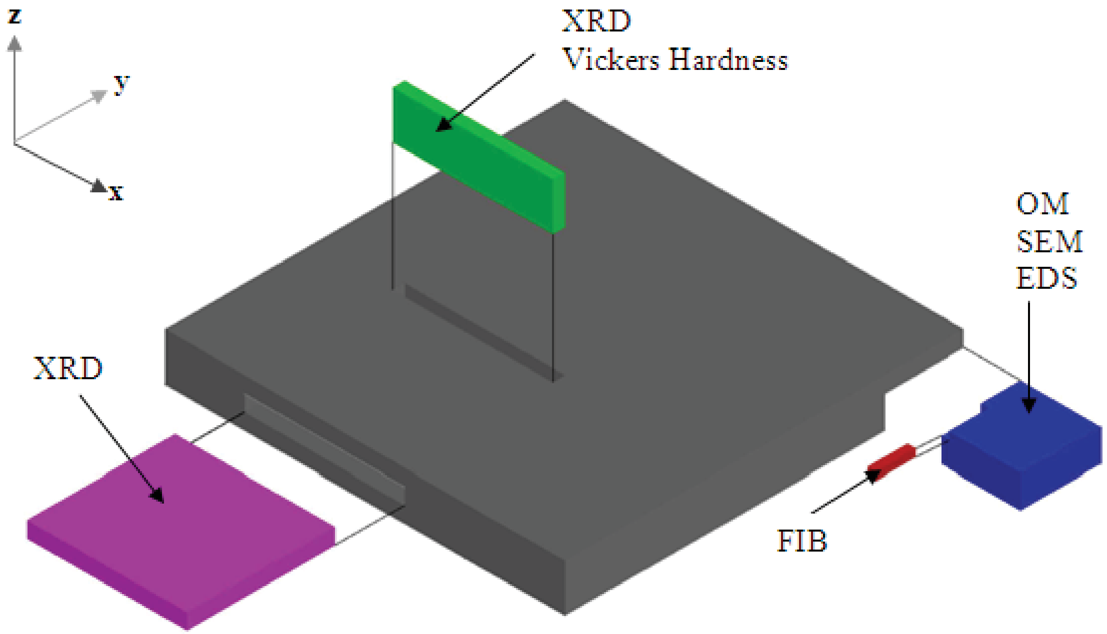

Fig. 3-1: A visual representation of the sectioned Al and Al-7.5wt.%Fe samples. The areas analyzed by OM (blue), SEM (blue), EDS (blue), XRD (green and violet), Vickers indentation hardness (green), and FIB (red) are depicted. The x-y-z coordinate system shown in the upper left hand corner was adopted to better report and interpret results. The x-y-z coordinates relative to this image are referenced frequently throughout this document.

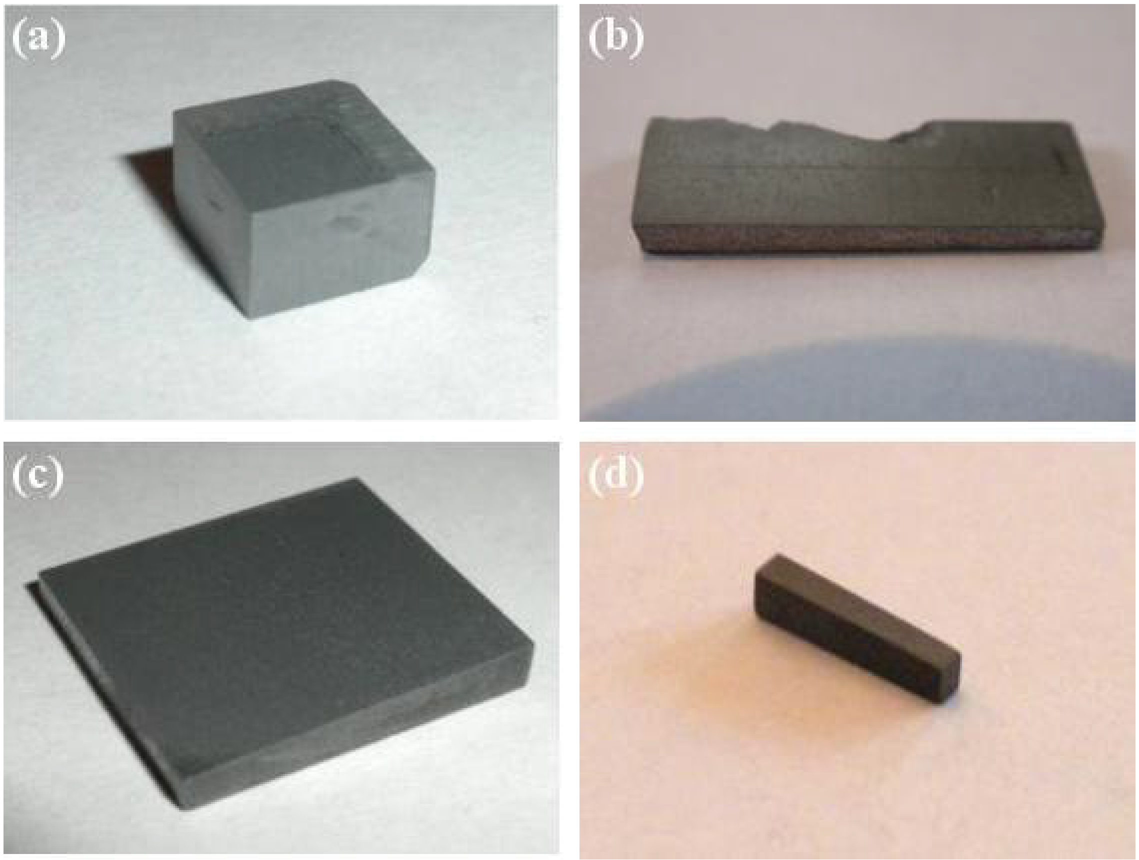

Fig. 3-2: (a) Section from the Al sample showing the three polished surfaces (x-y, x-z, and y-z planes) examined by OM, SEM, and EDS. (b) Section from the Al-7.5wt.%Fe sample showing the polished surface (x-z plane) examined by XRD and tested by Vickers indentation hardness. (c) Section of the Al-7.5wt.%Fe sample showing the polished surface (x-y plane) examined by XRD (d) section of the Al sample showing the polished surfaces (x-y and x-z planes) prepared for FIB techniques.

The supplementary samples were sectioned using the same equipment. For the examination of the melt sample, a piece was cut and ground into a 9 mm × 7 mm × 7 mm section, shown in Fig. 3-3(c). Grinding was accomplished using a water cooled mechanical polishing wheel and 120 grit SiC paper. A single sample from the Al-25wt.%Si was obtained for OM, SEM, and EDS analysis. The sample was cut from the corner of the original material similar to the other OM/SEM/EDS samples illustrated in

Fig. 3-1. The Al(2hr) sample was sectioned to reveal the reaction interface between the transformed material and the clear fused quartz preform, shown in Fig. 3-3(d).

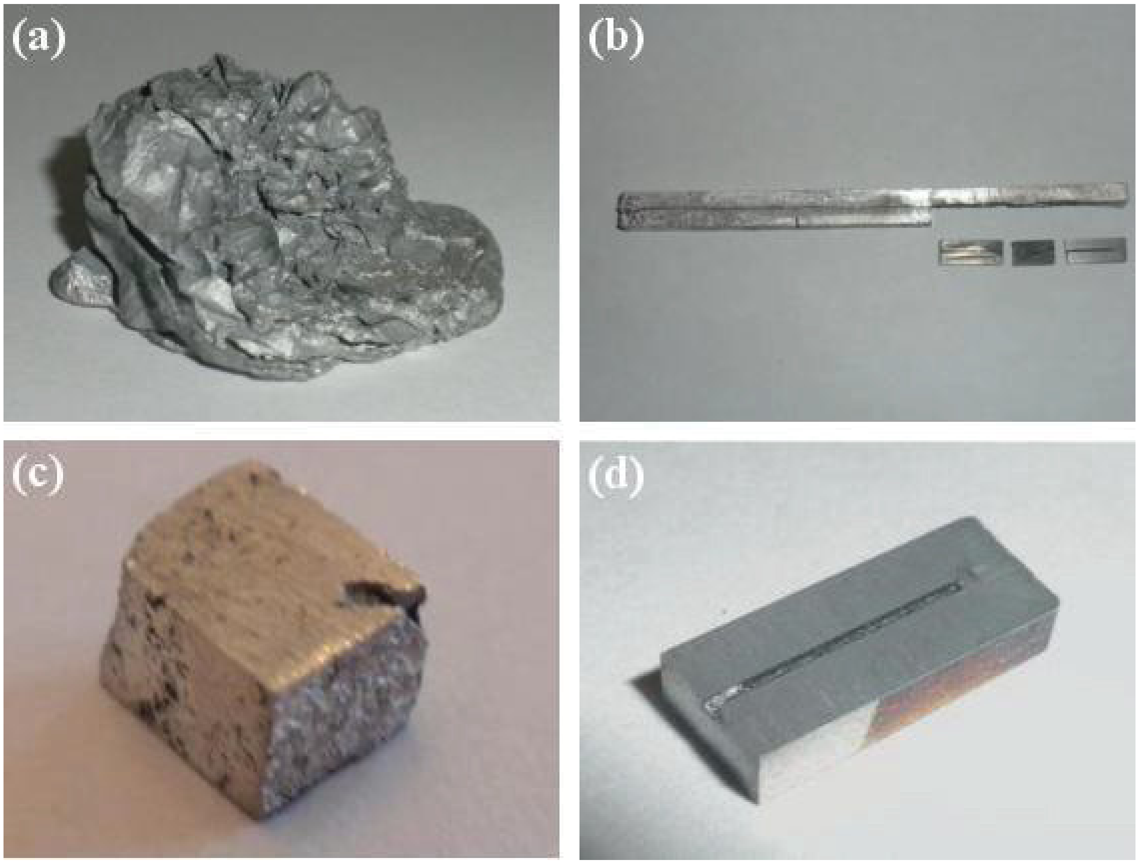

Fig. 3-3: The melt sample (a) is shown with its flat surface facing down. The melt was cut and ground into a 9 mm × 9 mm × 7 mm section (c) for OM, SEM, and EDS analysis. The Al(2hr) sample (b) is shown after initial sectioning. A piece of the Al(2hr) sample (d) was cut to reveal the transition between transformed material and the clear fused quartz preform for OM, SEM, and EDS analysis.

Fine polishing reveals a material's microstructure as well as defects and other intricate details. It is an important process necessary to achieve high quality optical and scanning electron micrographs. Due to the high hardness of the ceramic phases, diamond impregnated disks and compounds were used to grind and polish the materials. To ensure accuracy and consistency for all analytical techniques, every examined surface was ground and polished using a mechanical polishing wheel according to the steps enumerated in Table 3-3. First, the sectioned samples were ground to a flat, even surface using diamond impregnated disks. Next, diamond suspensions and corresponding cloths were used to polish the samples. A final polish was accomplished using a finishing cloth and colloidal silica suspension. To reduce scratching the samples were thoroughly cleansed with soap and rinsed with water between steps, which prevents particle contamination among polishing disks. Due to the porous nature of some samples, a brief ultrasonic cleansing was employed to further reduce contamination.

Table 3-3: Grinding/Polishing Procedure

Step	Disk Type	Suspension	Lubrication
Grinding 1	Struers Diamond Piano 120 grit	None	Water
Grinding 2	Struers Diamond Piano 600 grit	None	Water
Polish 1	Struers DP-Plan Cloth	Struers 6 µm diamond DP-Suspension	Struers DP-Lubricant Blue
Polish 2	Struers DP-Dac Cloth	Struers 3 µm diamond DP-Suspension	Struers DP-Lubricant Blue
Final Polish	Struers OP-Chem Cloth	Struers colloidal silica OP-Suspension	Water for final 30 seconds

3.3. Instrumentation

3.3.1. Optical Microscopy

Samples to be examined by reflected light or incident light optical microscopy were rinsed with alcohol to remove surface contamination. The samples were mounted on glass slides using reusable adhesive putty and were pressed to provide level surface. Macroscopic features were investigated using a Nikon SMZ800 stereo optical microscope. A ZEISS Axiophot compound light microscope was employed for brightfield and polarized light microscopy. Both models were equipped with PixeLink® CCD cameras for image acquisition.

The main difference between stereo and compound optical microscopy is that stereo microscopes use two separate light paths to generate an image, whereas compound microscopes use a single light path. In stereo microscopy, the two paths of light are generated from slightly different angles and focused through two separate series of optical lenses and mirrors. This results in a 3D image in which the depth of a sample can be observed. While this is useful for a number of applications, such as specimen manipulation, the resolution is limited. Stereo microscopes can typically achieve magnification levels between ×5 and ×50, although some advanced models can reach up to ×400 magnification. On the other hand, compound microscopes, which are often referred to simply as microscopes, use a single path of light focused through a series of optical lenses and mirrors. In a microscope, the light path can be viewed through a monocular or split and viewed through a binocular. The resulting image is 2D, but magnification levels between ×5 and ×1000 can be achieved.[73]

For this experiment it was mentioned that brightfield and polarized light microscopy techniques were employed. Reflected brightfield observation is the simplest and most common microscopy technique used in metallurgy. In brightfield microscopy, the reflected light is returned to the viewer unaltered. Contrast is achieved by the partial or complete absorption of white light by surface features. In polarized light microscopy, a polarizing filter is placed between the sample and light source and an analyzer is placed between the reflected light and observation tube. Polarized light microscopy is especially useful for viewing the crystalline structure of anisotropic materials. Isotropic materials, such as liquids, most glasses, and cubic structures, have the same optical properties no matter what direction they are viewed. Light passing through an isotropic material is reflected at a constant angle and at a constant velocity. Anisotropic materials, which comprise 90 percent of all solid substances, have optical properties that vary according to the incident angle of the light path and the crystallographic axes. As polarized light passes through anisotropic materials, it is refracted into two rays. Both rays travel at different velocities and are polarized with vibration directions orientated at right angle to one another. The analyzer recombines these rays using constructive and destructive interference, which is useful for providing crystallographic information about a sample.[74]

3.3.2. Scanning Electron Microscopy (SEM)

A JEOL JIB 4500 Multi-beam System was utilized for scanning electron microscopy analysis. SEM samples were thoroughly cleaned in an ultrasonic bath followed by an alcohol rinse to remove any contamination. The samples were secured to the sample holder using two-sided conductive carbon tape. An additional piece of conductive copper tape was bridged from the holder to the sample surface in order to increase conductivity. Secondary and backscatter electron micrographs were collected.

SEM uses a highly focused electron beam to scan a sample surface and generate an image based on the interaction at each point. The electron beam, which is less than 10 nm in diameter, is focused through a series of electromagnetic condensers and objectives and scanning is controlled by electromagnetic coils. An accelerating voltage between 1 and 30 kV can be used and a magnification range between ×10 and ×300,000 can be achieved. Unlike light microscopy, SEM produces a large depth of field which allows the micrographs to be in focus at all points across a rough surface. Also, SEM does not suffer from the problem of light reflecting off at odd angles and being lost from view.

The interaction between the electron beam and sample surface can generate two types of electrons for imaging. Secondary electrons are generated from the top 10 nm of the surface and are most commonly used to produce micrographs. Inelastic scattering causes the energy from the beam electrons to partially or completely transfer to the sample. This causes weakly bound electrons with energies less than 50 eV to be emitted.

These secondary electrons can then be analyzed by a detector and used to generate a micrograph. Backscatter electrons are associated with elastic scattering, which means that they change direction without losing velocity or energy. Back scattering occurs when a beam electron collides with the nucleus of an atom and exits the sample in roughly the same direction from which it came. Backscatter electrons are generated up to 1000 nm below the sample surface. Backscatter micrographs contain gray level variations that are dependent on atomic weight, with brighter areas corresponding to heavier atoms, and can offer some indication of the compositions and their locations within a sample.[75]

Figure 3-4 illustrates the depth and relative size, known as interaction volume, from which secondary and backscatter electrons may be produced. It also shows the interaction volume from which characteristic x-rays utilized in EDS may emanate. Only electrons or x-rays that escape the sample can be detected. Therefore, the low energy secondary electrons can only be detected from the top layers while the high energy backscatter electrons can be detected from greater depths. The enlargement of the backscatter signal source reduces resolution, which is why secondary electrons are most often used to produce images.[76]

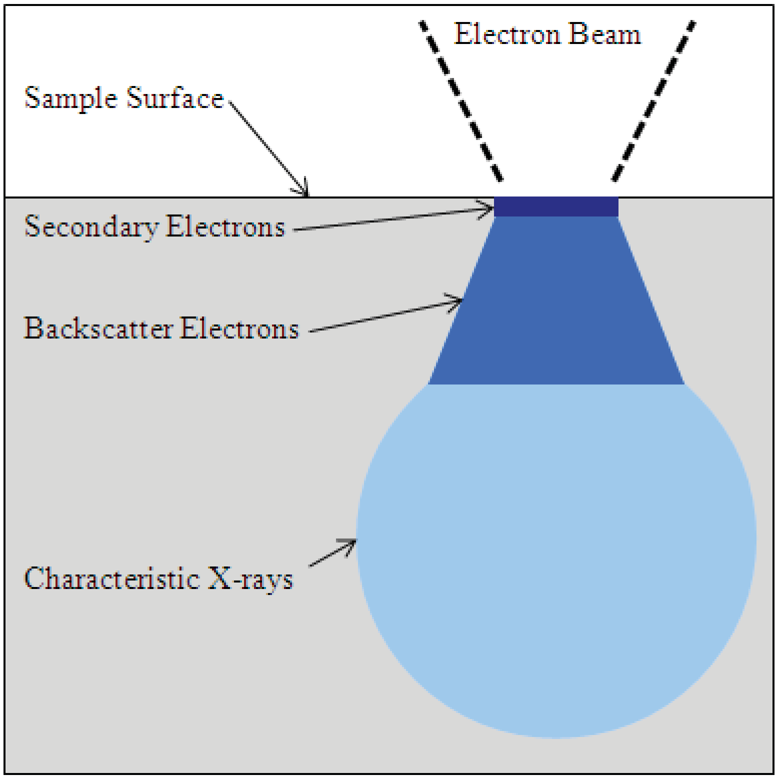

Fig. 3-4: Representation of electron beam interaction volume during SEM analysis. Volumes depicting the source of secondary electrons, backscatter electrons, and characteristic x-rays are labeled.

3.3.3. Energy Dispersive Spectroscopy (EDS)

An EDAX™ Apollo SDD EDS detector coupled with the JEOL JIB-4500 Multi Beam System was used to collect energy dispersive spectroscopy data. The same samples prepared for SEM were also used for EDS analysis. Both EDS spectra and elemental maps were collected. Phase Cluster Analysis (PCA) was performed on select maps using EDAX™ Genesis software.

EDS is used to indentify the chemical compositions and distributions of compounds within a sample. In EDS, the electron beam from a SEM column is used to bombard a sample and knock out inner shell electrons from atoms near the surface. The removal of an inner shell electron puts an atom in an excited state causing an outer shell electron to move into the vacancy. For example, a K shell electron void may be filled by electrons from the L, M, or N shells. During the atomic relaxation, the energy difference between the inner and outer shell electrons is released as characteristic x-rays. The energies of the characteristic x-rays are unique to each element. Therefore, these events can be plotted as discrete peaks that can be used to identify elements. An EDS spectrum is a plot of x-ray energy versus intensity. From an EDS spectrum it is possible to identify elements present in a specific location of a sample.[76]

EDS elemental maps can be used to show the distribution of elements for a specific area of a sample. The signal produced by the characteristic x-rays for a given element is modulated such that areas of greater concentration appear brighter on the micrograph. In other words, bright areas indicate the strong presence and dark areas indicate the absence of a given element in an EDS map. Areas that exhibit differences in intensity can be correlated to the topography shown in an SEM micrograph of the same area.[75] Phase cluster analysis (PCA) can be applied to such maps. In PCA, each pixel in the micrograph is assigned a color based on the EDS spectrum collected for that point. For example, alumina contains both aluminum and oxygen in its EDS spectrum. Every pixel that contains the aluminum-oxygen ratio associated with alumina can be assigned a color and its distribution can be monitored. PCA can be used to enhance the understanding of phase distribution within a material.

Quantitative analysis using EDS is possible, but is very difficult to perform with a high degree of accuracy. While many modern instruments are factory calibrated and include software with preprogrammed correction factors, another underlying issue remains. Relating to Fig. 3-4, characteristic x-rays that are generated by electron beams come from the largest depths and have the poorest resolution.[76] The limited resolution prevents quantitative analysis of materials that have very small phases or three-dimensional overlap of phases, such as TCON products. For example, in a TCON material the spectrum of an alumina phase might also include characteristics x-rays from a neighboring aluminum phase. The resulting quantification will show a greater amount of aluminum than is actually present in the alumina. For this reason, quantitative EDS analysis was excluded from this report.

3.3.4. Focused Ion Beam (FIB)

A JEOL JIB-4500 Multi-beam System equipped with a gallium ion source was used for focused ion beam techniques. The FIB was used to produce micrographs, ultra fine surface polishes, and TEM samples. Samples for FIB techniques were prepared and mounted identically to those examined by SEM and EDS. The system is outfitted with an Omniprobe^{TM} OMP-AUTOPROBE 200.1 nanomanipulator for TEM sample removal and mounting. Carbon and tungsten gas deposition systems marketed by JEOL aided in the manufacturing of TEM samples.

FIB techniques involve bombarding a sample with a finely focused beam (≈5 nm) of heavy ions, typically Ga^+ ions. The interaction between the ions and sample surface produces a transfer of energy that can result in ion reflection (backscattering), electron emission, electromagnetic radiation, atomic sputtering, ion emission, sample damage, and sample heating. Much like in the SEM, low energy electrons emitted near the sample surface can be used to generate micrographs. Ion beams are not as finely focused as electron beams and generally offer lower resolution. However, ion interaction offers better channeling contrast from crystals than electron interaction. Therefore, grain structure that is normally not observed by SEM imaging can be viewed by FIB imaging. The degree of contrast depends on the orientation of the crystal planes and the incident angle of the ion beam, see Fig. 3-5. For example, if the ions channel along the crystalline planes there is less interaction with surface atoms. Tilting the sample to change these parameters can induce different contrast effects.[77]

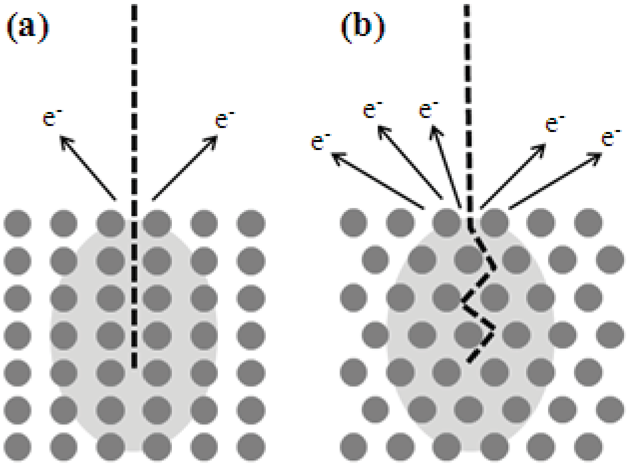

Fig. 3-5: Different contrast effects are produced during FIB imaging depending on the angle of the incident beam relative to the orientation of the crystal planes. If the ion beam channels along the crystal planes (a) there is less interaction with surface atoms and less secondary electrons produced. When crystal planes are orientated so that there is significant interaction with surface atoms (b) more secondary electrons are produced.

The ion beam can also be used to sputter, or mill, atoms from a material. The collision between the beam ions and the sample can cause atoms to be dislodged from their initial sites. If an atom absorbs enough energy to be removed from its original site, it can also collide with other atoms creating a cascade effect. If these displacements are near the sample surface the atoms may be emitted and sputtering occurs.[77] In this experiment, FIB sputtering has been used for two different applications. The first was to provide an ultra fine polish on the surfaces of the Al and Al-7.5wt.%Fe samples. This was accomplished by tilting the samples so that the ion beam was perpendicular to an edge, depicted in Fig. 3-6 with examples shown in Figs. 3-7 and 3-8. Sputtering techniques were used to polish a 30 μm × 40 μm area parallel to the ion beam, which was then investigated using SEM and FIB imaging. A second application is for the manufacturing of TEM samples. For this experiment, a TEM sample was prepared from the Al-7.5wt.%Fe sample. Fig. 3-9 illustrates the steps of this process, with an actual example depicted in Fig. 3-10. The final dimensions of the sample were approximately 10 μm × 5 μm × 0.01 μm.

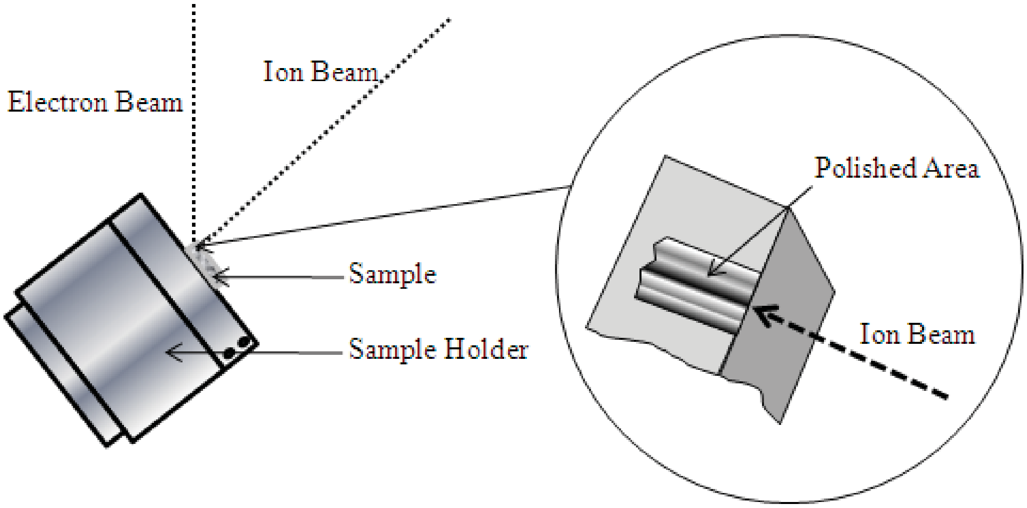

Fig. 3-6: Illustration showing the FIB polishing technique used to create ultra fine surface polishes.

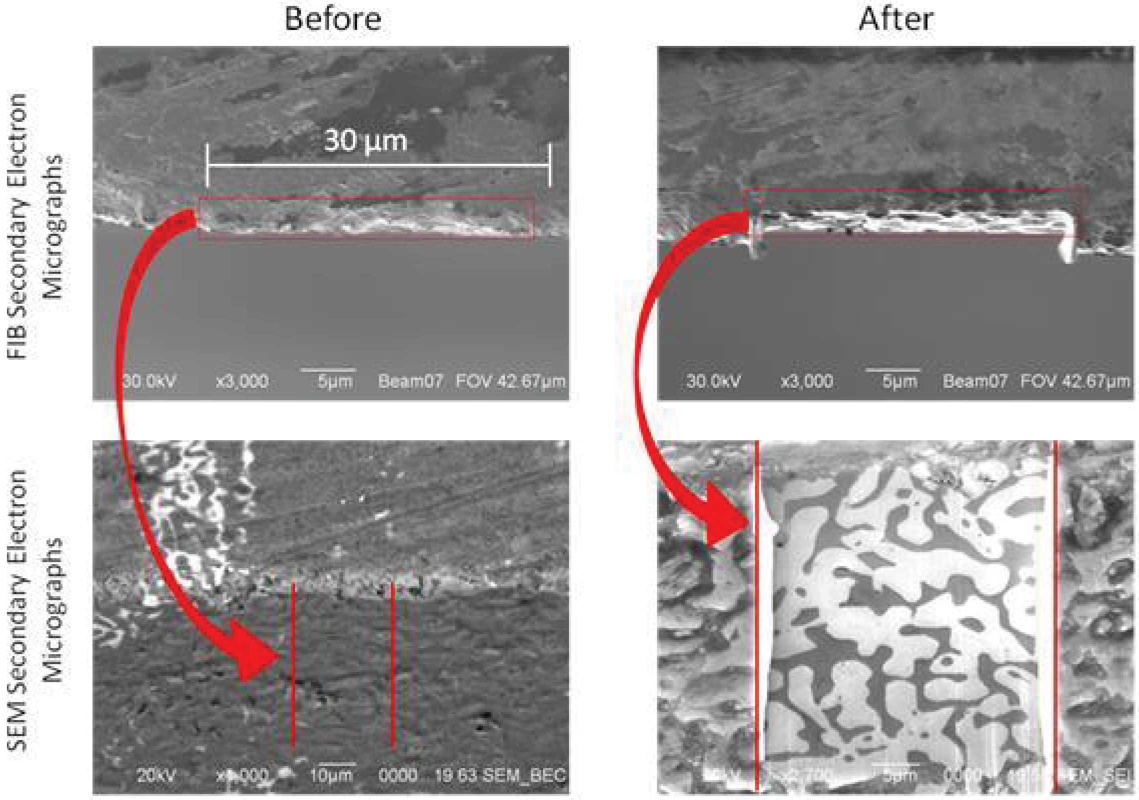

Fig. 3-7: Micrographs showing FIB polished areas of the Al-7.5wt.%Fe sample before (left) and after (right) ion milling. The FIB secondary electron micrographs on the top show the edge of the sample that is perpendicular to the ion beam. The SEM secondary electron micrographs on the bottom show the same area from the vantage point of the electron beam.[3]

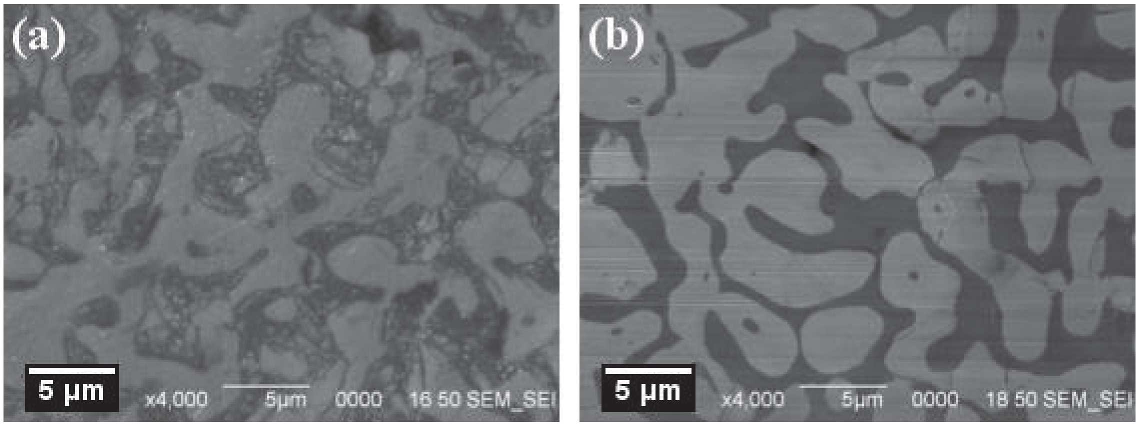

Fig. 3-8: Comparison of a mechanically polished surface (a) versus a FIB polished surface (b).[3]

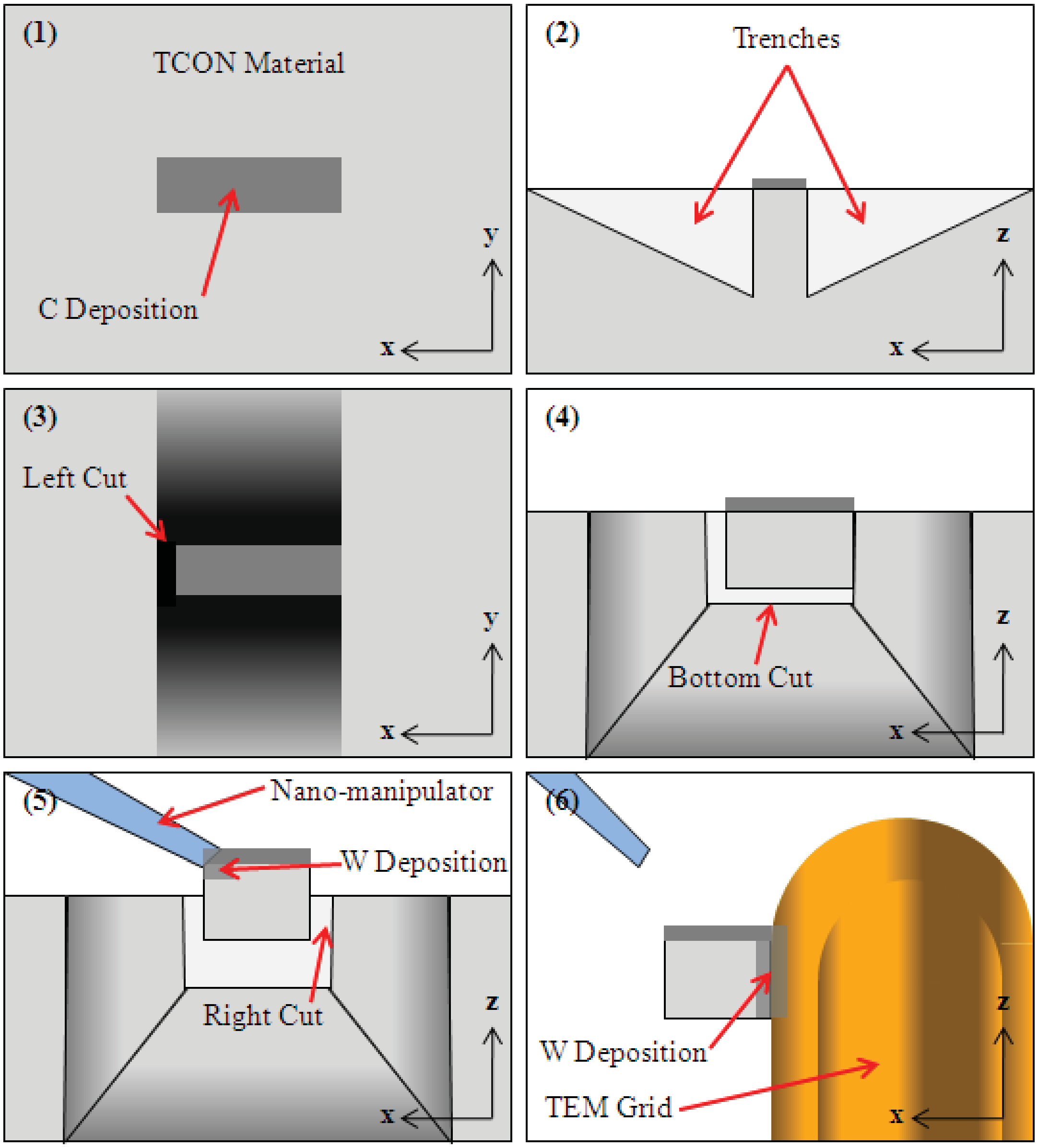

Fig. 3-9: The steps used to manufacture a TEM sample using the FIB are illustrated. (1) A 15 µm × 3 µm carbon deposition is made on the surface of the area to be removed. The carbon deposition creates a smooth milling surface that reduces defects. (2) Atomic sputtering is used to mill trenches along the length of the designated sample. (3) The left side of the designated sample is cut free via sputtering. (4) The ion beam is aligned parallel to the trenches and the bottom of the sample cut free. (5) The nano-manipulator is attached to the sample by a tungsten deposition, the right side is milled to completely free the sample, and the sample is lifted out. (6) The sample is attached to the TEM grid by a tungsten deposition, sputtering is used to remove the nano-manipulator, and the sample is thinned to a thickness that is electron transparent (less than 100 nm).

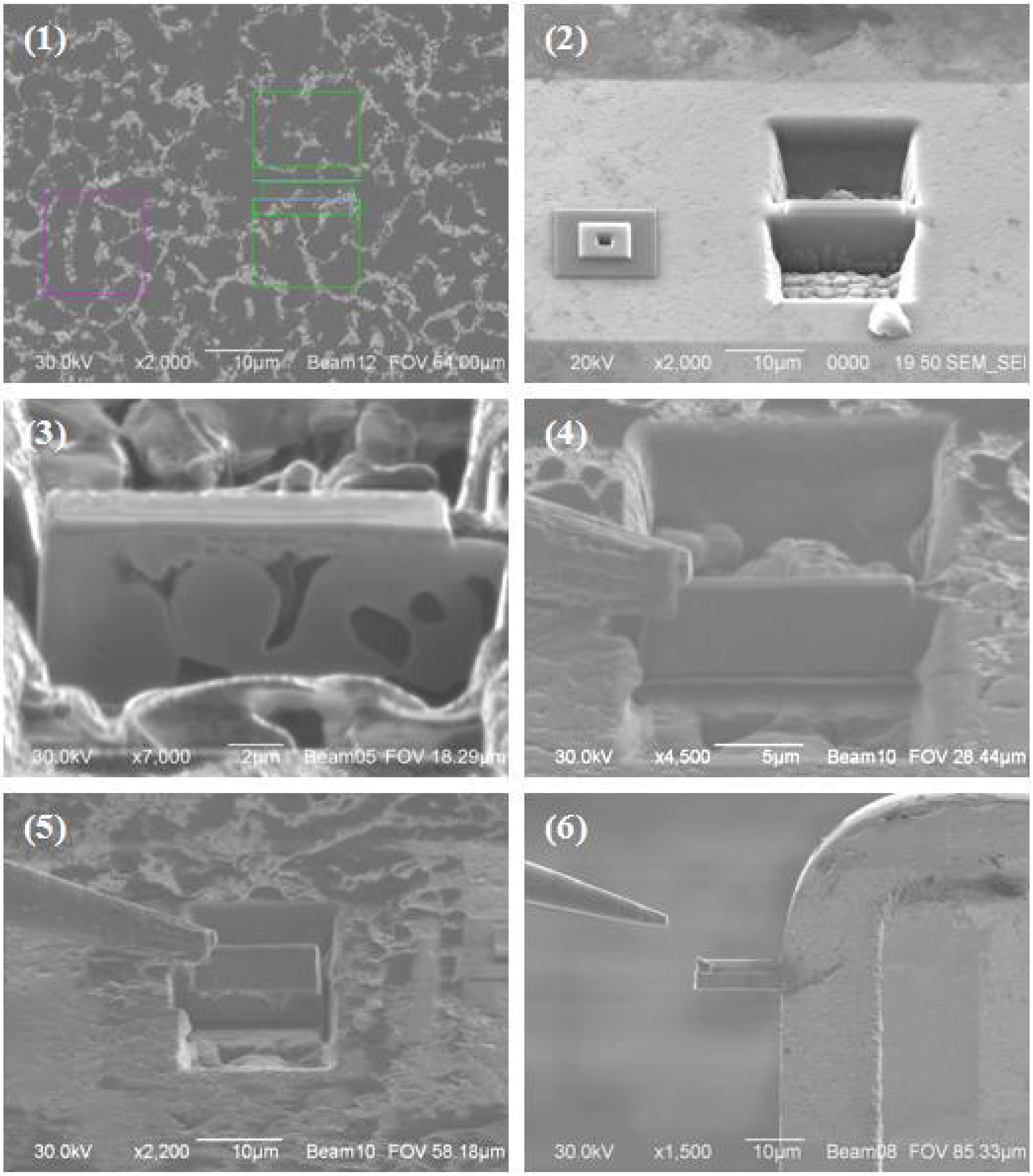

Fig. 3-10: SEM and FIB secondary electron micrographs depicting the preparation of a TEM sample according to the steps in Fig. 3-9.[3]

3.3.5. Transmission Electron Microscopy (TEM)

A JEOL JEM-2100 Scanning/Transmission Electron Microscope equipped with an EDAX^{TM} Genesis 2000 energy dispersive spectrometer was used for TEM analysis. The instrument was set to operate at its maximum accelerating voltage of 200 kV. TEM images are created by the diffraction/interference of an electron beam passing through the sample. Therefore, “electron transparent” samples should be used to obtain a micrograph. An “electron transparent” TEM sample for a 200 kV beam generally should be less than 100 nm thick. FIB techniques were employed to prepare a TEM sample from the Al-7.5wt.%Fe material. The scanning transmission electron microscopy (S/TEM) function was utilized to collect darkfield S/TEM micrographs and EDS spectra.

TEM uses a highly focused electron beam that is passed through a sample, hence transmission, to produce extremely high resolution micrographs. Magnifications in excess of one million times can be achieved with resolutions of 0.1 nm. These capabilities allow the observation of material ultrastructures, including the individual atoms that comprise the material. Accelerating voltages for TEM systems can range between 50 and 400 kV. Greater accelerating voltages enable the beam to transmit through thicker samples. The beam is focused on the sample using a series of electromagnetic lenses, coils, and apertures. As the electron beam is transmitted through the sample it is projected onto a phosphorescent screen for viewing. Modern TEM microscopes are equipped with specially designed CCD cameras for image acquisition.[75]

A well equipped TEM can be operated in several modes, or combination of modes, to obtain different information. Some of these operational modes include high contrast, high resolution, brightfield, darkfield, and diffraction. The JEOL JEM-2100 model used in this experiment is also equipped with scanning/transmission electron microscopy (S/TEM) capabilities. In this experiment, S/TEM and darkfield TEM methods were combined to produce micrographs and corresponding EDS spectra. The S/TEM mode rasters the finely focused electron beam across a selected area of the sample, which is ideal for collecting EDS data. Darkfield micrographs are obtained from the scattered electrons rather than direct beam electrons. Darkfield is often used to increase contrast between different phases or crystallographic regions.[78] The combined technique is ideal for viewing the different phases within the TCON material while simultaneously collecting EDS data to identify their compositions.

3.3.6. X-ray Diffraction (XRD)

Powder X-ray diffraction patterns were collected using a Bruker D8 Advance diffractometer with Cu-K_α radiation. The data were collected at room temperature in reflective mode in Bragg-Brentano geometry. Al and Al-7.5wt.%Fe XRD samples were affixed to open sample cups using wax. The data were analyzed and fitted to the database patterns using the EVA Application 7.001 software of SOCABIM (1996-2001), distributed by Bruker AXS.

XRD is a powerful analytical technique that provides information about the compositional and crystallographic structure of materials. XRD directs a beam of x-rays at a sample. If the sample is crystalline, the x-ray beam will be diffracted by the atomic planes. The diffraction of the x-ray beam can be measured and related to Bragg's equation, Eq. 3-1, which can be used to solve for interplanar spacing. XRD can be performed for single crystals or multi-crystalline powders. The data obtained from single crystals provide detailed information about the lattice structure, including unit cell dimensions, atomic positions, bond lengths, bond angles, and site ordering. Refinement of single crystal XRD data can provide the exact crystal structure of the material.[79]

$$n\lambda = 2d \sin \theta \qquad \text{(Eq. 3-1)}$$

d = interplanar spacing of atomic planes
θ = incidence angle of the x-ray beam
λ = wavelength of x-ray
n = integer (1,2,..n) relating to the order of diffraction

For this experiment, powder XRD was performed on the samples. Powder XRD can be performed on either powders or solid samples that are multi-crystalline. A diffraction pattern, which is a plot of intensity versus 2θ, is the output of powder XRD experimentation.[79] Literally hundreds of thousands of compounds have been studied by powder XRD and their diffraction patterns catalogued according to their d-spacings obtained from Bragg's equation. Tabulations of d-spacings and relative peak intensities for many materials have been published by the International Center for Diffraction Data (ICDD). Compounds examined by powder XRD can be identified by comparing experimental diffraction patterns to those catalogued by ICDD. Of course, it is useful to have some prior knowledge of a sample's elemental composition to narrow the search. Further refinement of diffraction patterns can lead to information pertaining to the lattice parameters, crystallite size, and percent composition of phases.

While powder XRD is an extremely useful tool for identifying phases, it does have some limitations. Since amorphous materials do not have diffraction patterns they might not be suspected if XRD were the only technique used. For example, powder mixtures that contain both crystalline and amorphous material are not good candidates for XRD analysis. Another issue is the fact that XRD patterns are representative of randomly orientated crystals. If a sample contains phases that are preferentially orientated, meaning that their original crystallites are aligned along certain planes, the peak intensities will not match the theoretical intensities. Preferential orientation can complicate the identification and refinement of diffraction patterns.[80]

A diagram of a Bragg-Brentano geometry diffractometer as used in this research is shown in Fig. 3-11. An x-ray beam is generated by the x-ray tube and diffracted by a bent monochromator crystal. The monochromator for this particular system allows only the $K_{\alpha 1}$ radiation to pass through to the sample. The beam is focused onto an area of the sample by a slit and diffraction takes place. The diffracted x-rays are converged by an anti-scattering slit and strike the detector.

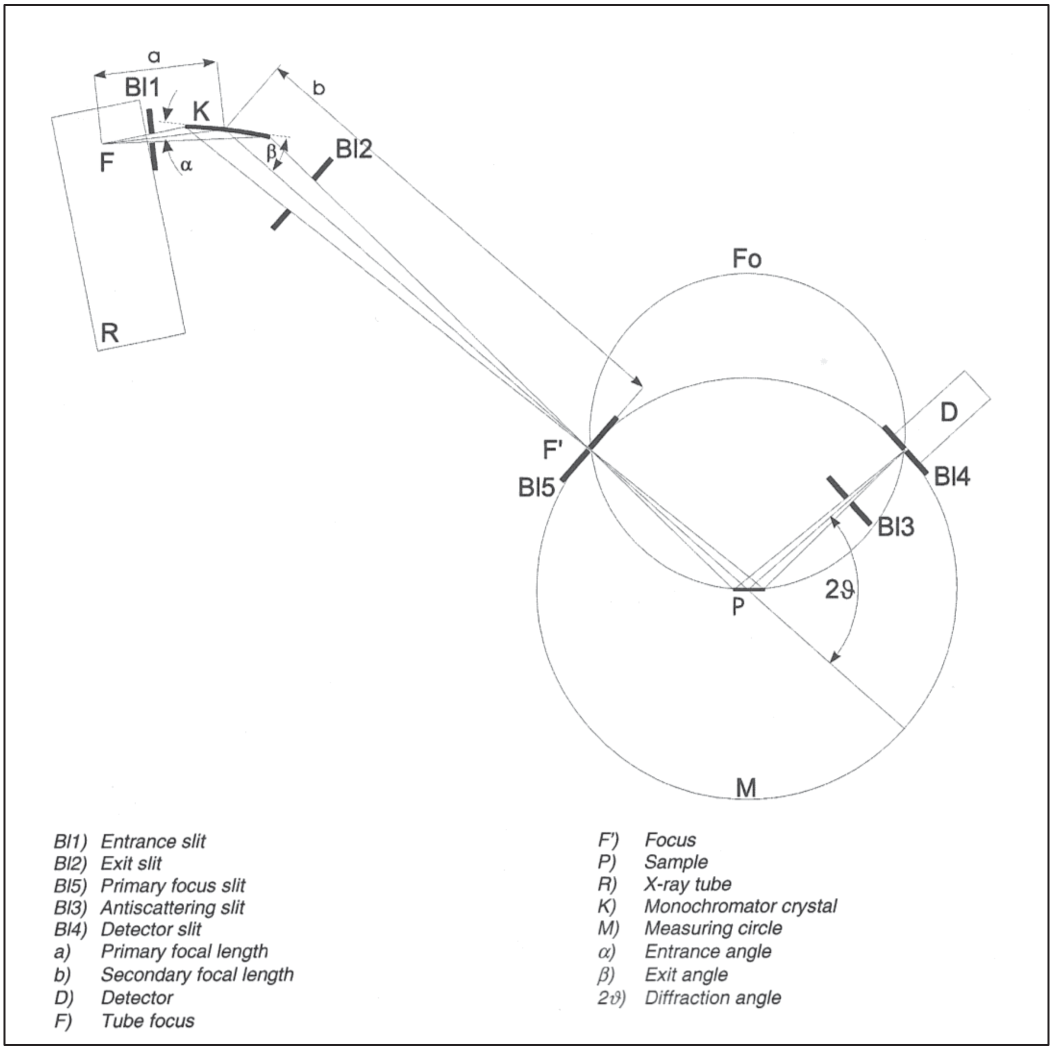

Fig. 3-11: Schematic of a Bragg-Brentano diffractometer.[81]

3.3.7. Vickers Indentation Hardness Testing

Hardness measurements can be used to test a material's resistance to permanent plastic deformation. Vickers hardness testing uses a pyramid shaped diamond to make indentations in a material. The indenter is pressed into the sample surface at 90° under a known load, which can range between 1g and several kilograms. Indentation sizes are on the micron scale and vary depending on the load. The diagonals of the diamond shaped indentation can be measured to determine the relative hardness of a material. It is important to note that there are several hardness tests that can be performed, including Brinell, Knoop, Rockwell, and variations of each. Each hardness test uses a different type of indenter and load specification.[82] Most hardness values are unit-less numbers and are used only for comparative purposes. Conversions tables have been developed to translate among different hardness scales, but generally there is no accepted method to do so accurately.[83]

Vickers hardness testing was performed using an indentation hardness tester marketed by the Wilson Company on the Al and Al-7.5wt.%Fe samples according to ASTM standard C1327 – 08.[83] The machine was calibrated using a standard reference block prior to experimentation. The samples were cleaned with alcohol to remove surface contaminations. A test load of 9.80665 N was used to make 25 indentations in each sample. Testing was performed at room temperature. Indentations were made in staggered parallel lines beginning at the outside edge and working towards the center of the sample, as shown in Fig. 3-12. Spacing between consecutive indentations is equidistant in the z-direction. Porous areas were avoided by shifting the indention a minimum distance in the x or y direction. Indentations deemed unacceptable due to excessive cracking, spalled edges, ragged edges, etc. were excluded from the results. Indentation sizes were measured using the SEM features of a JEOL JIB-4500 Multi Beam System. Vickers hardness numbers (HV) were computed according to Eq. 3-2, where P is the load (kgf) and d is the average length (mm) of the diagonals d_1 and d_2. The unit kgf (kilogram-force) is defined as the magnitude of force exerted on a 1 kg mass by the gravitational field, *i.e.* 1 kgf equals 9.80665 N. Statistical analysis of the results was performed with Minitab® 16 software.

$$HV = 1.8544(P/d^2) \tag{Eq. 3-2}$$

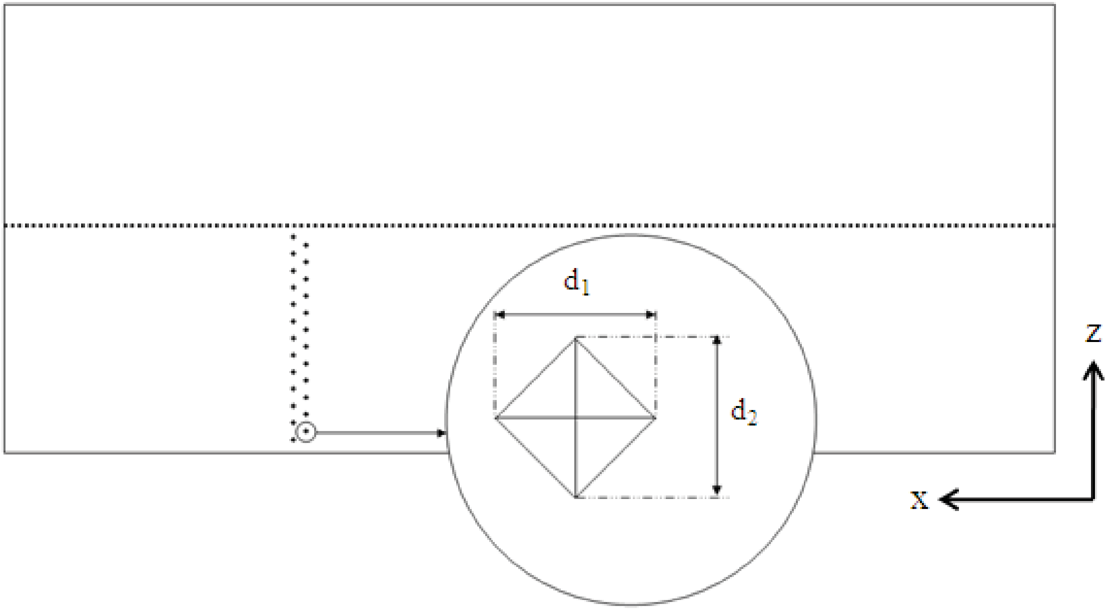

Fig. 3-12: Method used to measure the Vickers hardness values of the Al and Al-7.5wt.%Fe samples. Two columns of indentations were made beginning at the edge of the sample and working towards the center. The distance between consecutive indentations in the z-direction is equidistant. The length of each diagonal, d_1 and d_2, was measured in the SEM.

Chapter 4: Results

4.1. Macroscopic Observation

Stereo optical micrographs revealing macroscopic features of the Al and Al-7.5wt.%Fe samples are shown in Fig. 4-1. Initial observation of the polished cross-sections reveals that both samples contain a distinct Y-shaped boundary feature that is positioned symmetrical relative to the edges and corners of the sample. The Y-shape appears more uniform in the Al-7.5wt.%Fe sample as compared to the Al sample. An illustration depicting the boundary feature is shown in Fig. 4-2.

Macroscopic observation also shows striations throughout the Al-7.5wt.%Fe sample that are absent in the Al sample. In the stereo microscope, the striations appear as dark lines that are generally orientated parallel to each other. The width of the striations ranges between 5 and 100 μm and they can reach several hundred microns in length. Another interesting feature are bright columns that form perpendicular to the outer edges. The columns can be observed by tilting the sample in light and are accentuated by manipulating the light source of the stereo microscope, which induces different contrast effects. The columns have different widths, typically on the order of hundreds of microns, and are between 0.5 and 3 mm in length. The directions of both the dark striations and bright columns intersect at the Y-shaped boundary. Since the clear fused quartz preform was homogeneous, it is reasonable to assume that these features are a result of RMP processing.

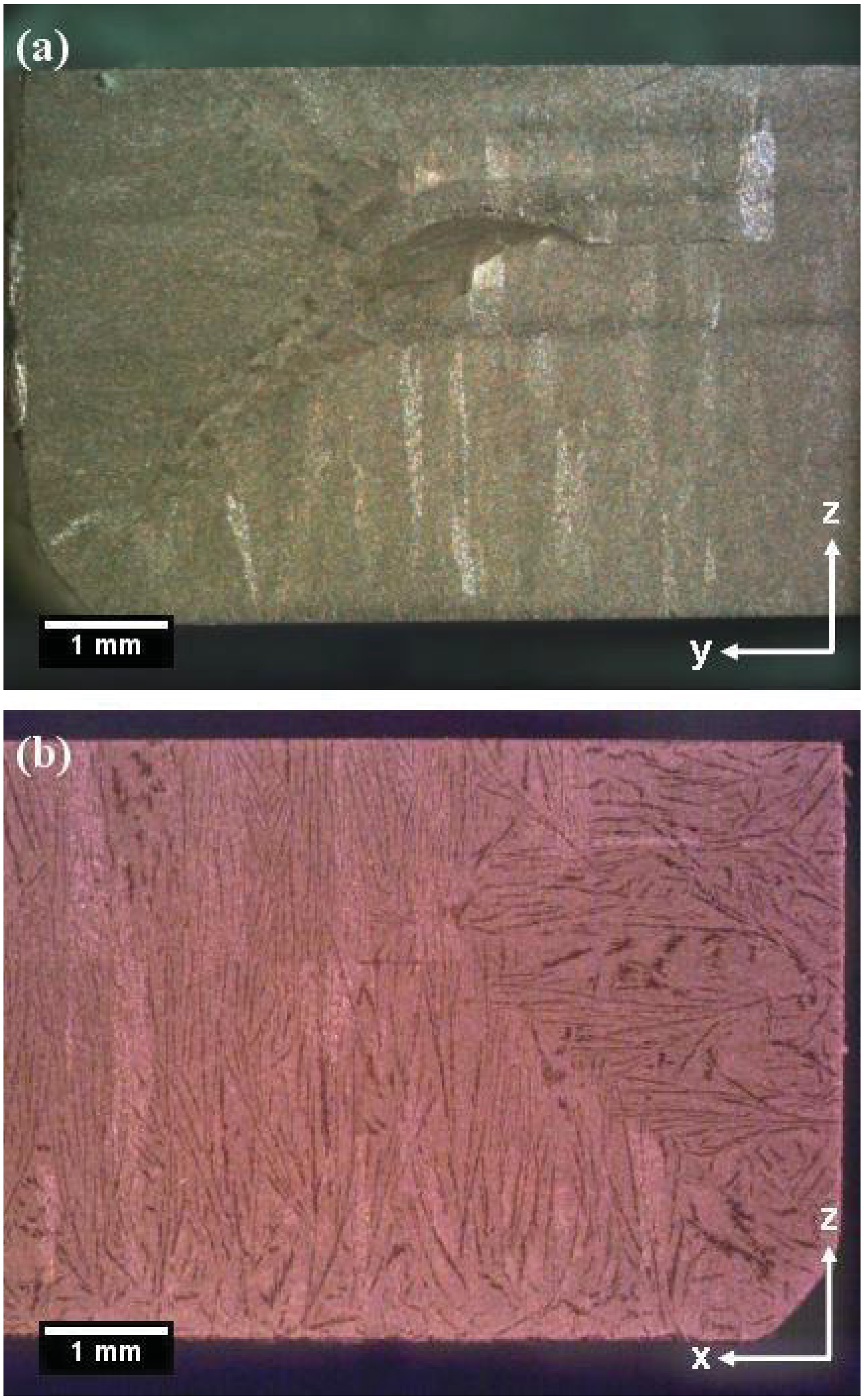

Fig. 4-1: Stereo-OM micrographs showing the polished cross-sections of the Al (a) and Al-7.5wt.%Fe (b) samples. The micrographs reveal a Y-shaped feature symmetrically positioned relative to the corners and edges of the samples. The symmetry is partially broken due to the fact that the top of the sample at the z-end was cut off during sectioning. Bright columns perpendicular to the sample edges are also observed in both samples. Dark striations consistent throughout the bulk of the Al-7.5wt.%Fe sample are not present in the Al sample.

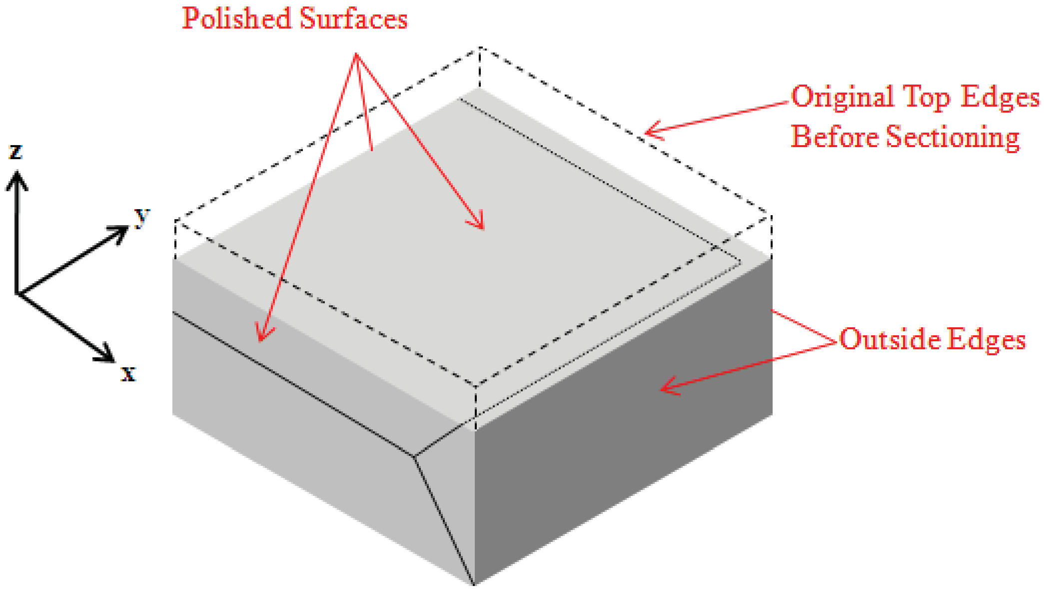

Fig. 4-2: Illustration depicting the Y-shaped boundary (black lines) observed in the Al and Al-7.5wt.%Fe samples designated for OM/SEM/EDS analysis. The boundary extends continuously throughout the material. The top of the sample was cut at the z-end during sectioning thus breaking the symmetry of the "Y" in the x-z and y-z planes. For information regarding how the sample was obtained from the original material refer to Fig. 3-1.

4.2. Microscopic Observation

Brightfield optical micrographs taken in the x-y-plane of the Al sample are shown in Fig. 4-3. Isolated voids of various sizes (indicated by arrows) are apparent throughout the sample. The optical micrograph in Fig. 4-3(b) shows a homogenous structure that contains two co-continuous phases, later identified as aluminum and alumina by EDS and XRD analysis. The backscatter electron micrographs in Fig. 4-4 were taken of the same area as the optical micrographs. Elemental contrast achieved by backscatter electron imaging confirms the presence of the two phases. Fig. 4-4(b), which was taken at a higher magnification, clearly shows the Al_2O_3-Al network. It is evident that mechanical polishing preferentially removed the softer Al phases causing a “dishing effect”. This effect is difficult to avoid because of the large difference in hardness between the alumina and aluminum. From microscopic observation in the x-y plane, it appears that the Al_2O_3 phase occupies a larger volume than the Al phase. This is consistent with previous findings.[1,2,13] The width of Al_2O_3 grains are on the order of a few microns (typically 3-5 μm). They appear to branch randomly in all directions, at least in the x-y plane.

Brightfield optical micrographs of the Al-7.5wt.%Fe sample and backscatter electron micrographs from the same area are displayed in Figs. 4-5 and 4-6, respectively. Based on microscopic observation, it appears that there are a greater number of voids in the Al-7.5wt.%Fe sample as compared to the Al sample. Further testing is necessary to determine unambiguously that the Al-7.5wt.%Fe in fact contains a greater volume of porosity. The Al_2O_3-Al network observed in the Al sample is also present in the Al-7.5wt.%Fe sample, but with the addition of the striated regions previously observed by stereo optical microscopy. The striations, which appear as bright areas in the optical and electron microscopes, were determined to be Fe-rich by EDS and XRD analysis. From the scanning electron micrographs it is clear that the striations are interconnected with the other phases. Based on microscopic observation, it appears that the dimensions and directions of the Al_2O_3 grains were not significantly affected by the iron addition.

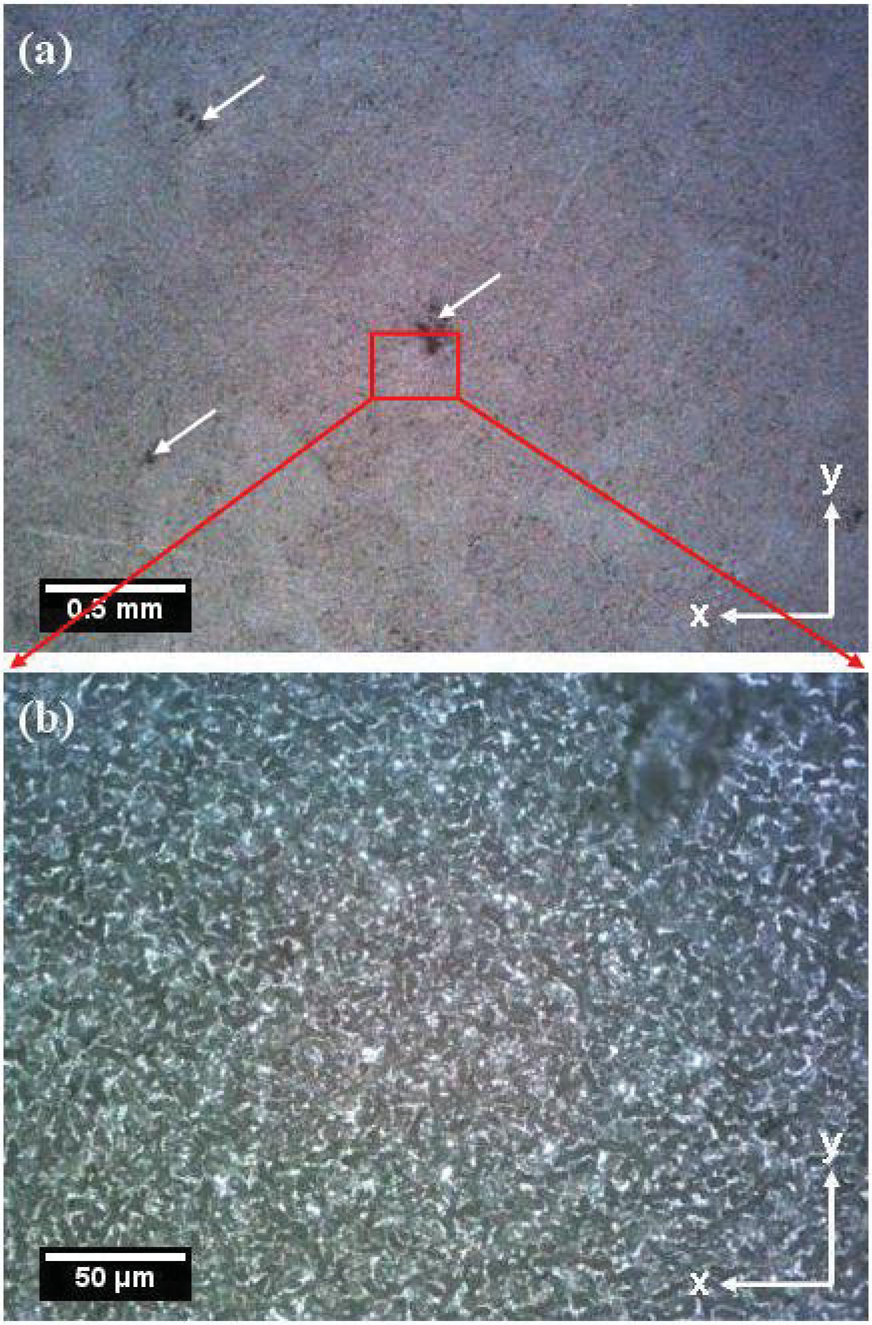

Fig. 4-3: Brightfield-OM micrographs showing the Al sample at low (a) and high (b) magnifications.[1] The micrographs reveal a homogenous structure consisting of two phases and some porosity, which appear as black spots. Some of the larger pores are indicated by arrows.

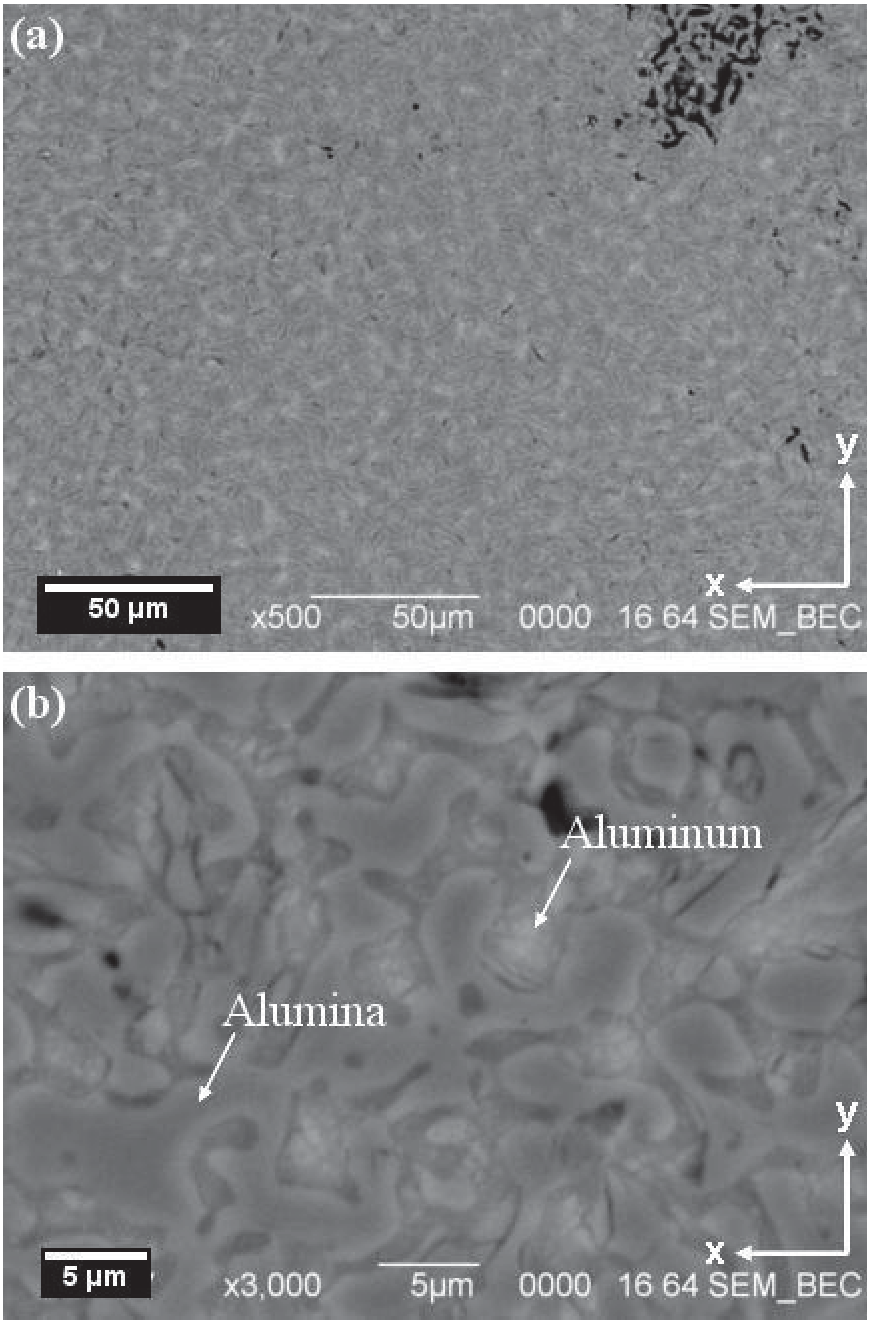

Fig. 4-4: SEM backscatter micrographs of the Al sample at ×500 (a) and ×3000 (b). The micrographs show an interconnected network of Al (light gray) and Al_2O_3 (dark gray) phases. They also reveal some porosity (black).

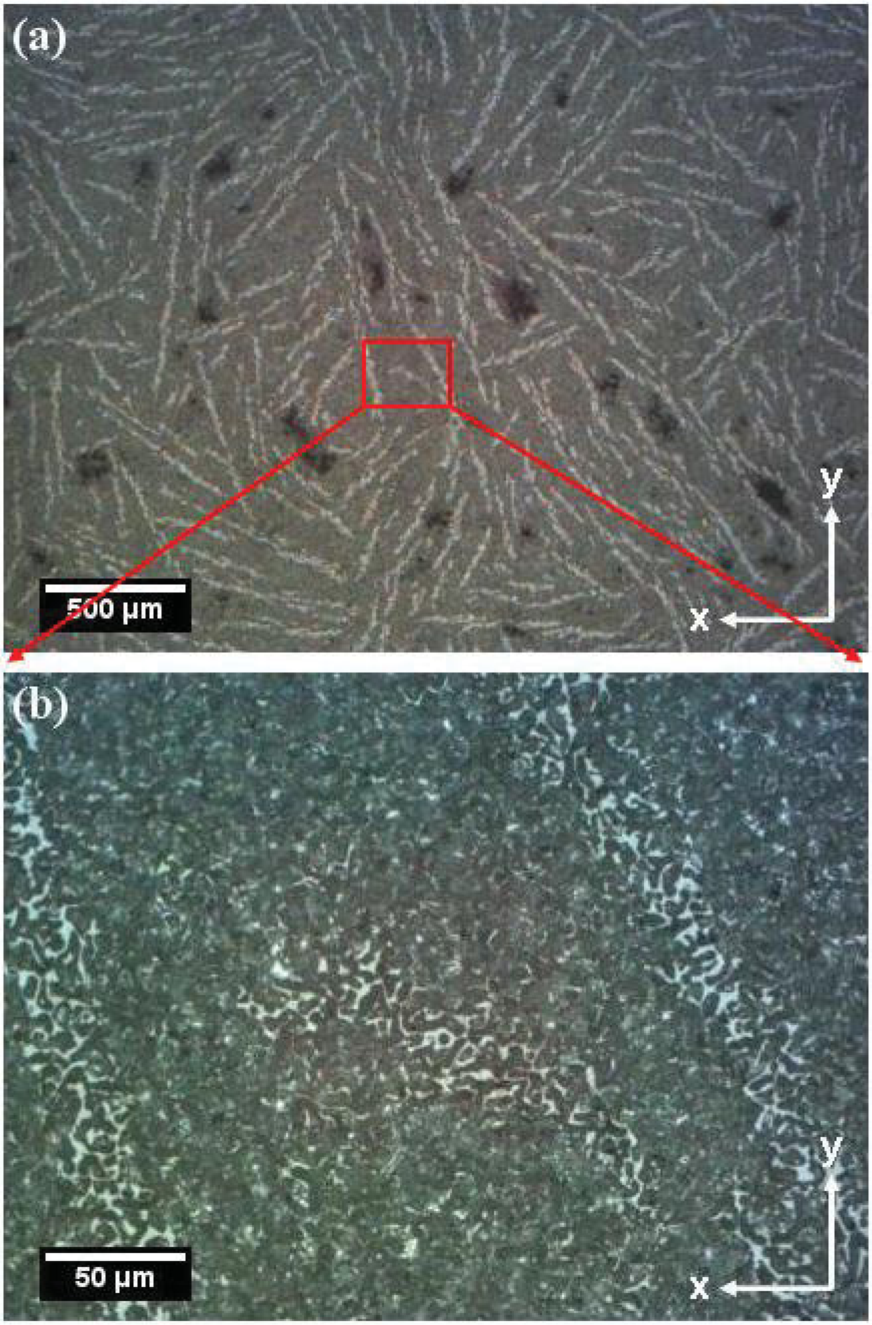

Fig. 4-5: Brightfield-OM micrographs showing the Al-7.5wt.%Fe sample at low (a) and high (b) magnifications.[1] The micrographs reveal bright striations and porosity throughout the sample. The porosity, indicated by black spots, is more prevalent than in the Al sample. At higher magnification, it is clear that the striations are not continuous, but are interconnected with two additional phases.

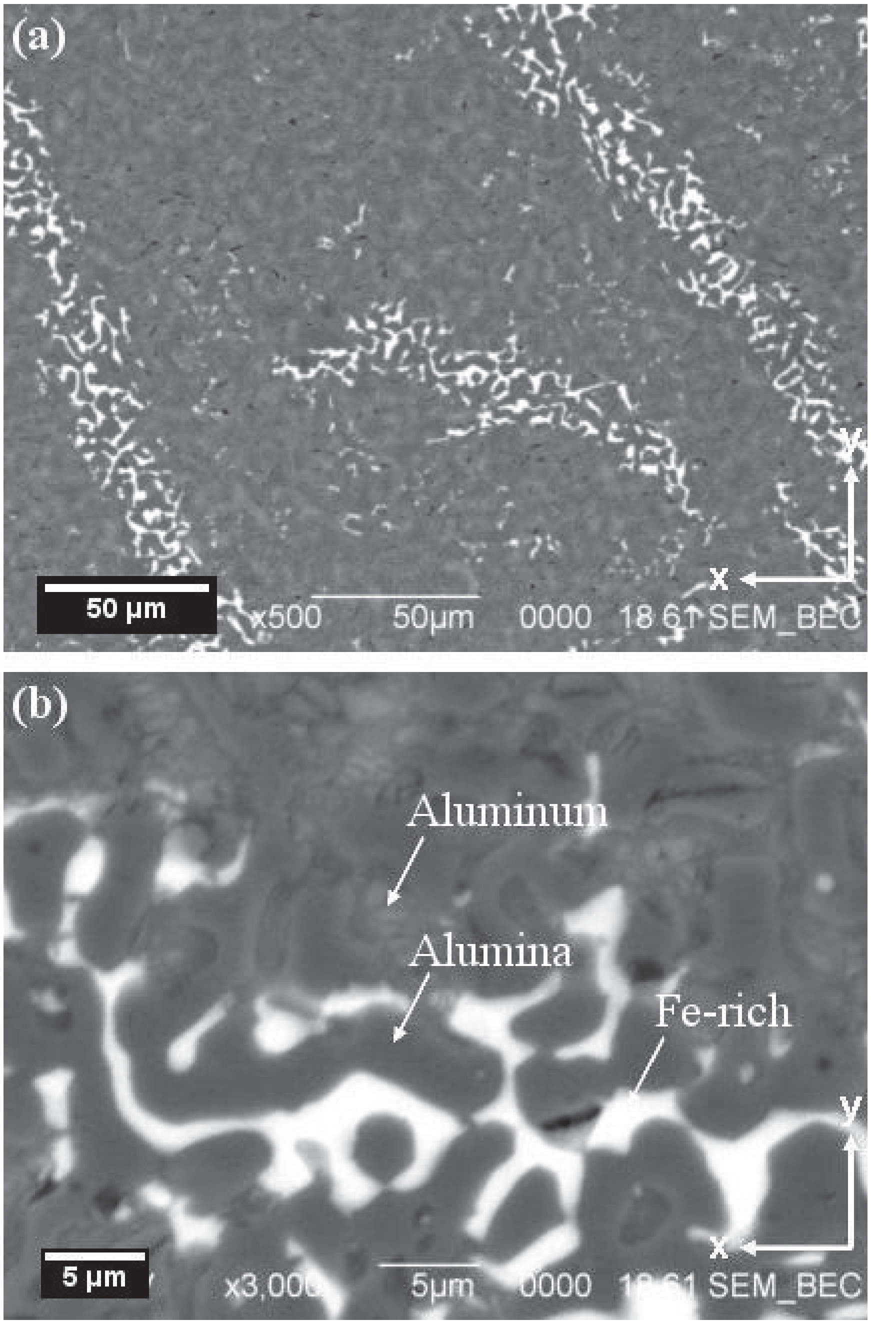

Fig. 4-6: SEM backscatter micrographs of the Al-7.5wt.%Fe sample at ×500 (a) and ×3000 (b). The micrographs show striations comprised of an Fe-rich (white) phase interconnected with the network of Al (light gray) and Al_2O_3 (dark gray). Some porosity (black) can be observed.

Fig. 4-7 is a three-dimensional reconstruction of the Al-7.5wt.%Fe sample using backscatter micrographs from the x-z, y-z, and x-y planes. It shows that the striations are actually plate-like features that, in this volume, contain the z-axis within their mean planes. Orientation with respect to x and y varies within the sample. The 3D reconstruction denotes a microstructural growth in the z-direction.

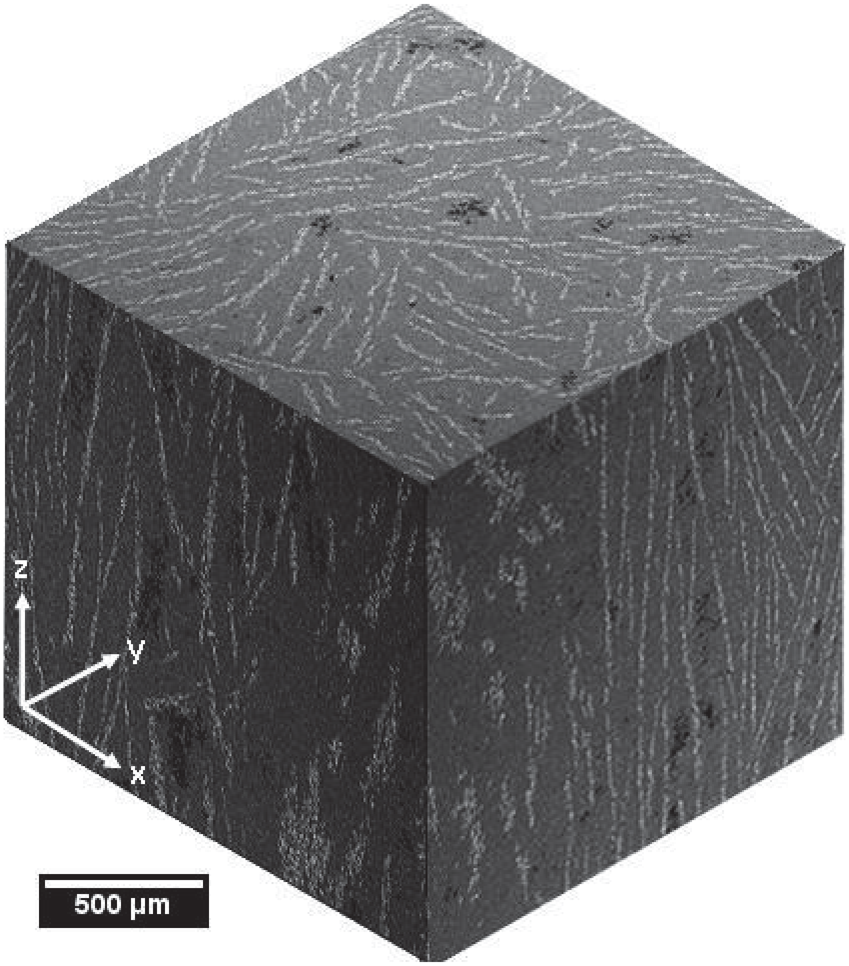

Fig. 4-7: A 3D reconstruction representing an approximate 1.5 mm × 1.5 mm × 1.5 mm volume of the Al-7.5wt.%Fe sample compiled from SEM backscatter micrographs, ×50 magnification.[1] The Fe-rich (white) phases are plate-like features that stretch in the z-direction. Orientation with respect to x and y varies within the sample. These features are characteristic of areas where penetration is unidirectional (i.e. areas away from the sample corners).

4.3. Phase Indentification

4.3.1. Energy Dispersive Spectroscopy (EDS)

Energy dispersive spectroscopy was used to identify the chemical composition of the observed phases. It is important to note that the resolution of EDS is limited by the three-dimensional nature of the materials. Depending on the material, characteristic x-rays can be generated as deep as 1000 nm below the sample surface. Therefore, it is possible to have an overlap of phases. Fig. 4-8 displays the EDS spectra collected from the light gray, dark gray, and white phases in the Al-7.5wt.%Fe sample. The light gray phase contains mostly aluminum and a small amount of oxygen. The oxygen may be due to the previously explained overlap of phases or to the oxidation of aluminum in air. Aluminum and oxygen were detected in the dark gray phase suggesting that it is alumina. The white phase, which represents the plate-like features, contains aluminum, iron, and a small amount of oxygen. Again, the oxygen may be from overlapping phases or oxidation from exposure to air.

An EDS elemental map showing the distribution of Al, O, Fe, and Si in the Al-7.5wt.%Fe sample is shown in Fig. 4-9. The silicon is a product of the reaction between Al and SiO_2 during processing. Although most of the silicon diffuses away from the reaction front and into the metal bath, from the elemental map it is clear that some of it remains trapped within the microstructure. It is interesting to note that the silicon precipitates in areas that do not contain iron as concisely defined particles, but is dispersed in the Al-Fe phases and directly bordering them.

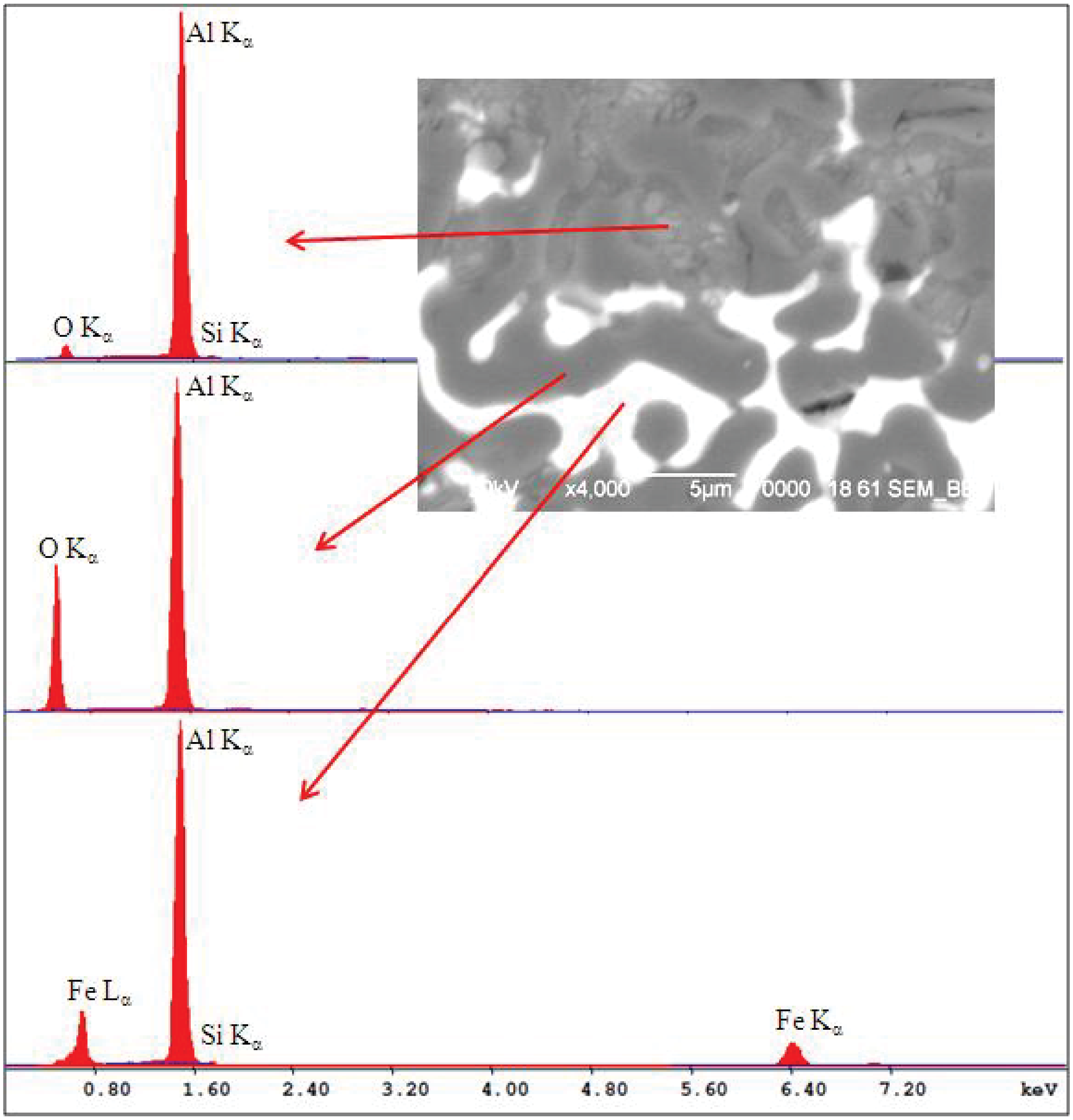

Fig. 4-8: EDS spectra from the light gray (a), dark gray (b), and white (c) regions of the Al-7.5wt.%Fe sample. The characteristic x-ray peaks indicate an Al metal phase, Al_2O_3 phase, and an Al-Fe-intermetallic phase. Trace amounts of Si are detected in the Al and Al-Fe spectra.

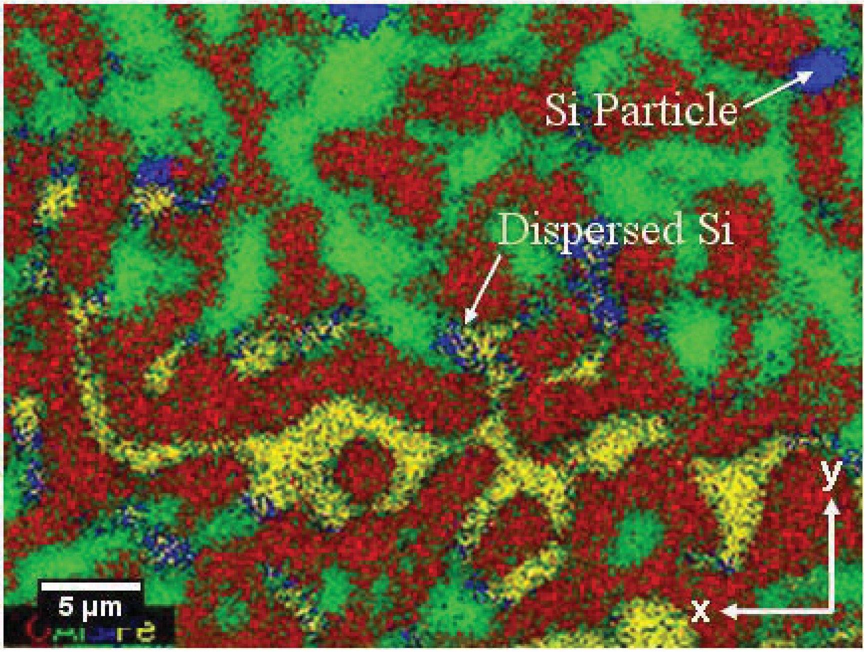

Fig. 4-9: EDS elemental map of the Al-7.5wt.%Fe sample relating to Fig. 4-6(b). The map shows the distribution of O - red, Al - green, Fe - yellow, and Si - blue.

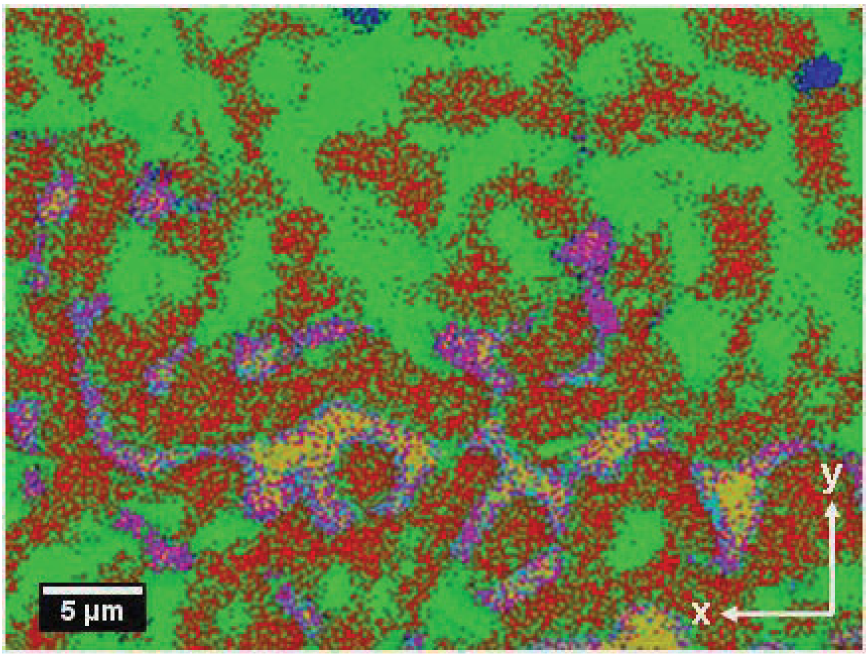

Fig. 4-10: Phase cluster analysis (PCA) using EDAX^{TM} software of the elemental map shown in Fig. 4-9. Al_2O_3 - red, Al - green, Si - blue, Al-Fe - yellow, Al-Fe-Si – cyan, and Al-Fe-Si-O - magenta phases were identified.

In an attempt to better understand this distribution, phase cluster analysis (PCA) was performed on the map and is displayed in Fig. 4-10. Al_2O_3, Al, and Si phases were identified with a high degree of confidence. However, the phases in Fe-rich regions are more complicated. PCA suggests the formation of an Fe-Al intermetallic surrounded by smaller, nano-scale Fe-Al-Si and Fe-Al-Si-O phases. The existence of such phases cannot be confirmed by SEM/EDS, which has limited resolution at the nano-scale. The distribution of Si in the iron-rich regions suggests that some interaction occurs between the displaced Si and the Al-Fe melt. A plausible explanation is that an Fe-Al-Si intermetallic forms in the melt, and upon cooling a low-Si Fe-Al precipitates first followed by the eventual crystallization of a high-Si Fe-Al-Si phase around the intitial low-Si phase.

4.3.2. X-ray Diffraction (XRD)

Powder XRD patterns from the x-y plane of the Al sample and the x-y and x-z planes of the Al-7.5wt.%Fe sample are shown in Fig. 4-11. XRD confirmed the presence of Al_2O_3, Al, and Si in both samples. In the Al-7.5wt.%Fe sample, additional diffraction peaks point to the existence of Al-Fe-alloy phases, but determination of the exact phase or phases is difficult based on the diffraction pattern alone. An $Al_{13}Fe_4$ (ICDD entry number 00-050-0797)[80] has tentatively been selected as the best fit, but other Al-Fe-alloys with different compositions showed similar agreement with experimental peaks. XRD did not show the additional phases suggested by PCA, probably due to the poor resolution of XRD at the nano-scale. The mismatch between experimental and theoretical peak intensity for the Al_2O_3, and to a lesser extent, for the Al phase can be explained by preferential orientation of the phases. In the case of the Al sample, the Al_2O_3 peaks are well defined but the intensity mismatch is obvious for almost all of the peaks. The mismatch in Al peak intensity can be observed, but is less obvious compared to the Al_2O_3 phase. In the Al-7.5wt.%Fe sample, the degree of disparity in peak intensity of Al_2O_3 is different depending from which plane the diffraction pattern was taken. This also supports the claim of preferential orientation as the cause for the intensity discrepancy. Again, the mismatch of Al peaks in the Al-7.5wt.%Fe sample is not as apparent as in the Al_2O_3. No preferential orientation of Si was detected in either sample.

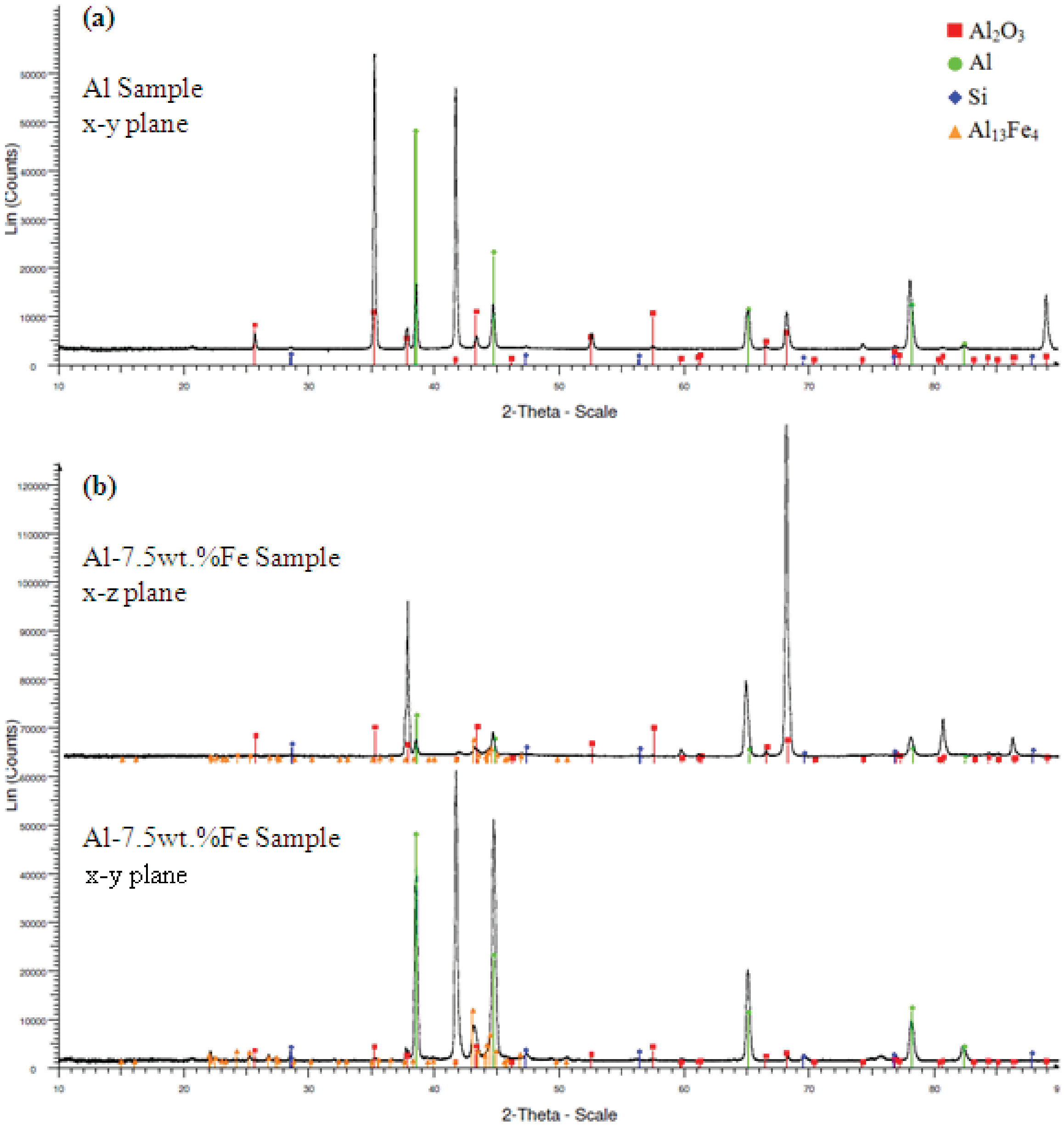

Fig. 4-11: Powder XRD patterns from the Al (A) and Al-7.5wt.%Fe (B) samples.[1] The Al sample was examined in the x-y plane and Al-7.5wt.%Fe sample was examined in the x-y (bottom) and y-z (top) planes. Both samples show preferential orientation of Al_2O_3 (■ ICDD: 00-010-0173, trigonal $R\bar{3}c$, a: 4.758Å, c: 12.991Å)[84] and Al (● ICDD: 00-004-0787, cubic $Fm\bar{3}m$, a: 4.049Å).[85] The data also show the presence of small amounts of Si (♦ ICDD: 04-001-7247, cubic $Fd\bar{3}m$, a: 5.429Å)[86] in both samples. The pattern suggests the presence of $Al_{13}Fe_4$ (▲ICDD: 00-050-0797, orthorhombic Bmmm, a: 7.751Å, b: 23.771Å, c: 4.034Å)[87] in Sample 2, but other Fe-Al alloys showed similarly well fitting patterns and further analysis is needed for an unambiguous assignment of the type of Fe-Al alloy.

4.3.3. Transmission Electron Microscopy

Preliminary research using transmission electron microscopy was performed on the Al-7.5wt.%Fe Sample. The darkfield STEM micrograph in Fig. 4-12(a) shows a TEM sample prepared by focused ion beam (FIB) techniques. The nano-scale interpenetration of the ceramic and metallic phases can be observed. The darkfield S/TEM micrograph taken at increased magnification focuses on an Fe-rich region, Fig. 4-12(b). Phases that contain both micro and nano-scale features are detected. EDS determined that the micro-sized phase is an Al-Fe intermetallic. The phases that have nano-scale features are identified as Al-Fe-Si and Al-Fe-Si-O. These smaller phases collect near the outer edges of the larger Al-Fe grains, which supports the findings of PCA. The formation of nano-scale phases may contribute to the superior flexural strength reported by Hendrick *et al*.[8] Future work utilizing high resolution TEM combined with the collection of electron diffraction patterns will be used to determine the exact composition and structure of these phases.

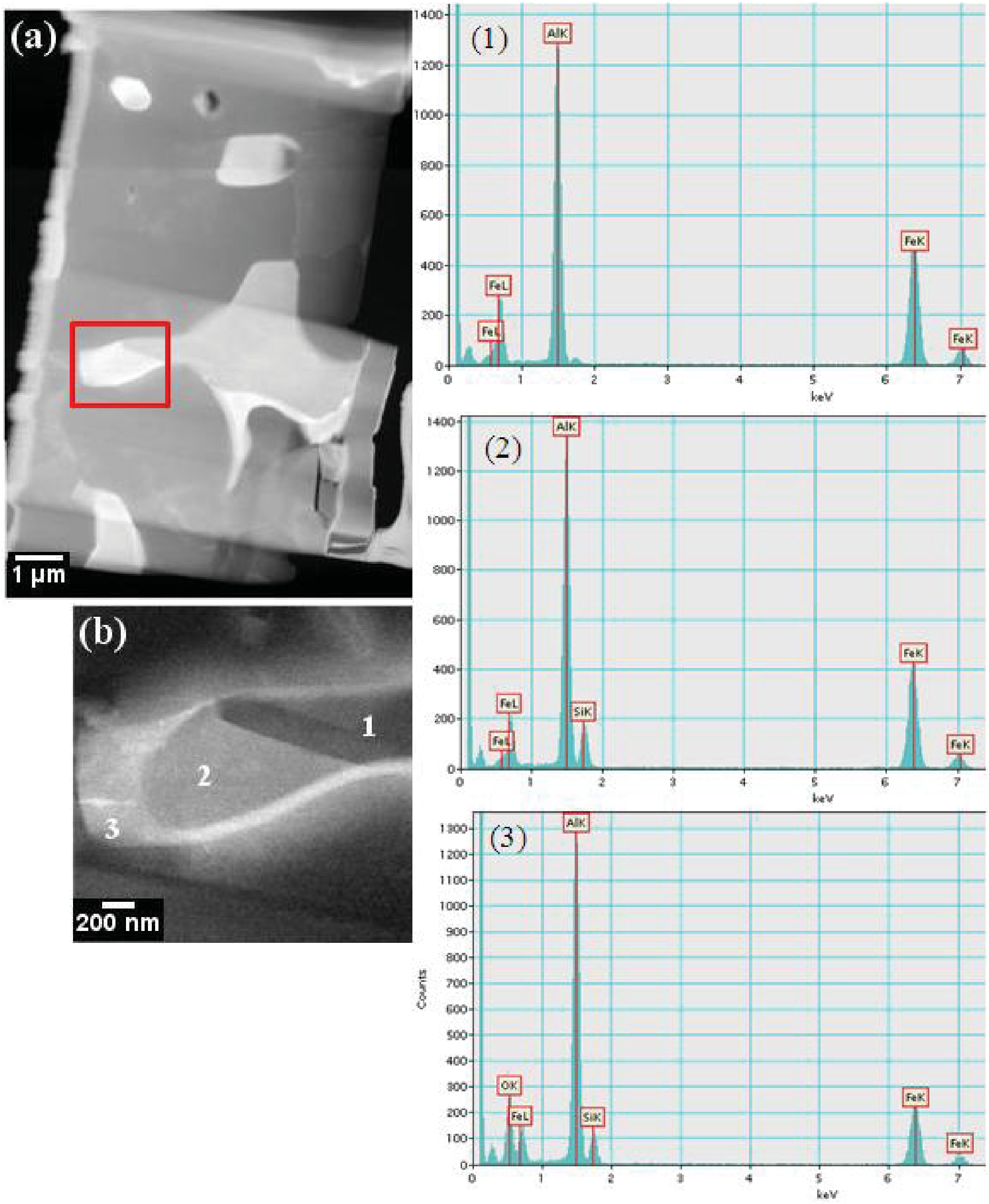

Fig. 4-12: (a) S/TEM darkfield micrograph showing the TEM Al-7.5wt.%Fe sample prepared by focused ion beam (FIB).[5] The change in contrast across the sample relates to differences in thickness. The bright regions represent Fe-rich phases. (b) STEM darkfield micrograph depicting an Fe-rich region at high magnification. The numbered phases were examined using EDS and their corresponding spectra are shown on the right. The Al-Fe (1) phase belongs to a larger micron-sized grain. The Al-Fe-Si (2) and Al-Fe-Si-O (3) phases possess nano-scale features and form along the outer edges of the larger Fe-Al grains.

4.4. Investigation of Observed Features

4.4.1. Al_2O_3 Colonies

To better understand the structural properties of the materials, the bright columns observed by stereo-OM were further investigated using SEM. Fig. 4-13 depicts seven enumerated regions that correspond to these columns in the Al sample. The columns' unique reflective properties can be attributed to different orientations of the Al_2O_3 phase, which is correlated with the findings of XRD. It appears that the RMP process produces Al_2O_3 colonies that are characterized by the orientation of their grains. The colonies propagate with the reaction front, or perpendicular to the edges, but are not perfectly parallel. From the two-dimensional micrographs, it is difficult to determine if the early termination of some colonies is due to the intersection with other colonies or if the path continues along a three-dimensional vector. The same discrepancy applies to colonies that appear to initiate in the middle of the sample. 2D observation of the 3D structure also limits the ability to determine the colony dimensions and the degree by which they vary.

The enumerated colonies from Fig. 4-13 are examined more closely in Fig. 4-14. With increased magnification, the different orientations among the Al_2O_3 colonies become evident. The Al_2O_3 phases stretch mainly in the direction perpendicular to the sample edges and exhibit some branching. This is the mechanism of formation that gives the material its three-dimensional structure. Relating to the 3D reconstruction in Fig. 4-7, the manner in which the Al_2O_3 phase forms forces the metallic features to be elongated in the z-direction, paralleling the elongated Al_2O_3 colonies. Regions 2-7 are similar in structure, though comparison is limited by 2D observation. Region 5 contains some alumina grains that have slightly larger widths than those found in the other regions. Region 1 is a smaller feature and has a microstructure unlike the other six regions. Structures similar to region 1 do not exist in the Al-7.5wt.%Fe sample and are found along the Y-shaped boundary feature near the corners of the Al sample. In region 1, the Al_2O_3 phase is finer and does not exhibit branching as observed in the other regions.

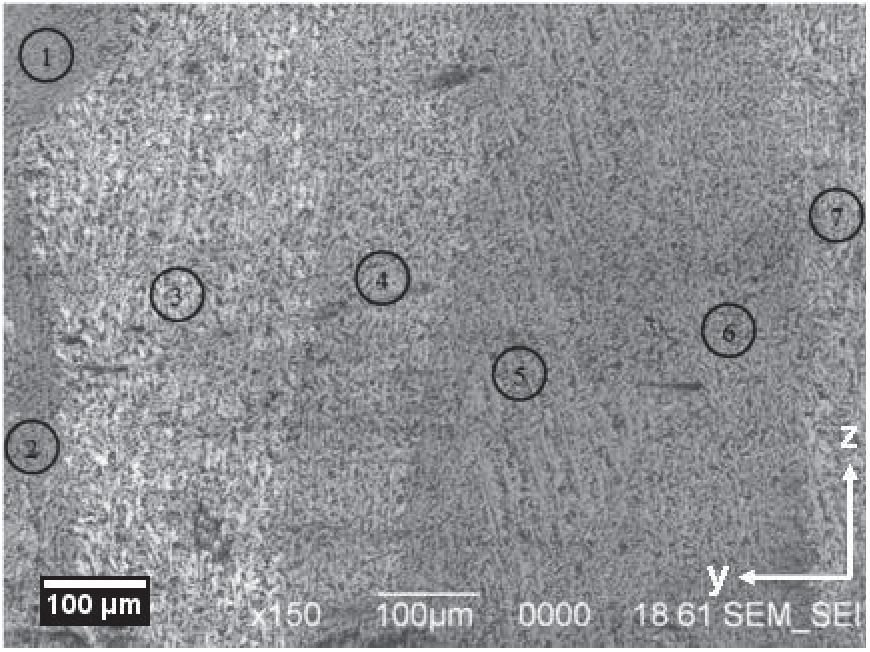

Fig. 4-13: SEM secondary electron micrograph showing the Al sample at ×150 magnification. Seven different regions corresponding to the bright columns observed in stereo-OM are numbered. The columns are related to the orientation of the Al_2O_3 grains. Regions 2-6 have similar microstructures with an overall growth in the z-direction. Region 5 contains some Al_2O_3 grains that are wider than those from the other regions. Region 1, which is near the Y-shaped border, has a finer microstructure and a different growth direction.

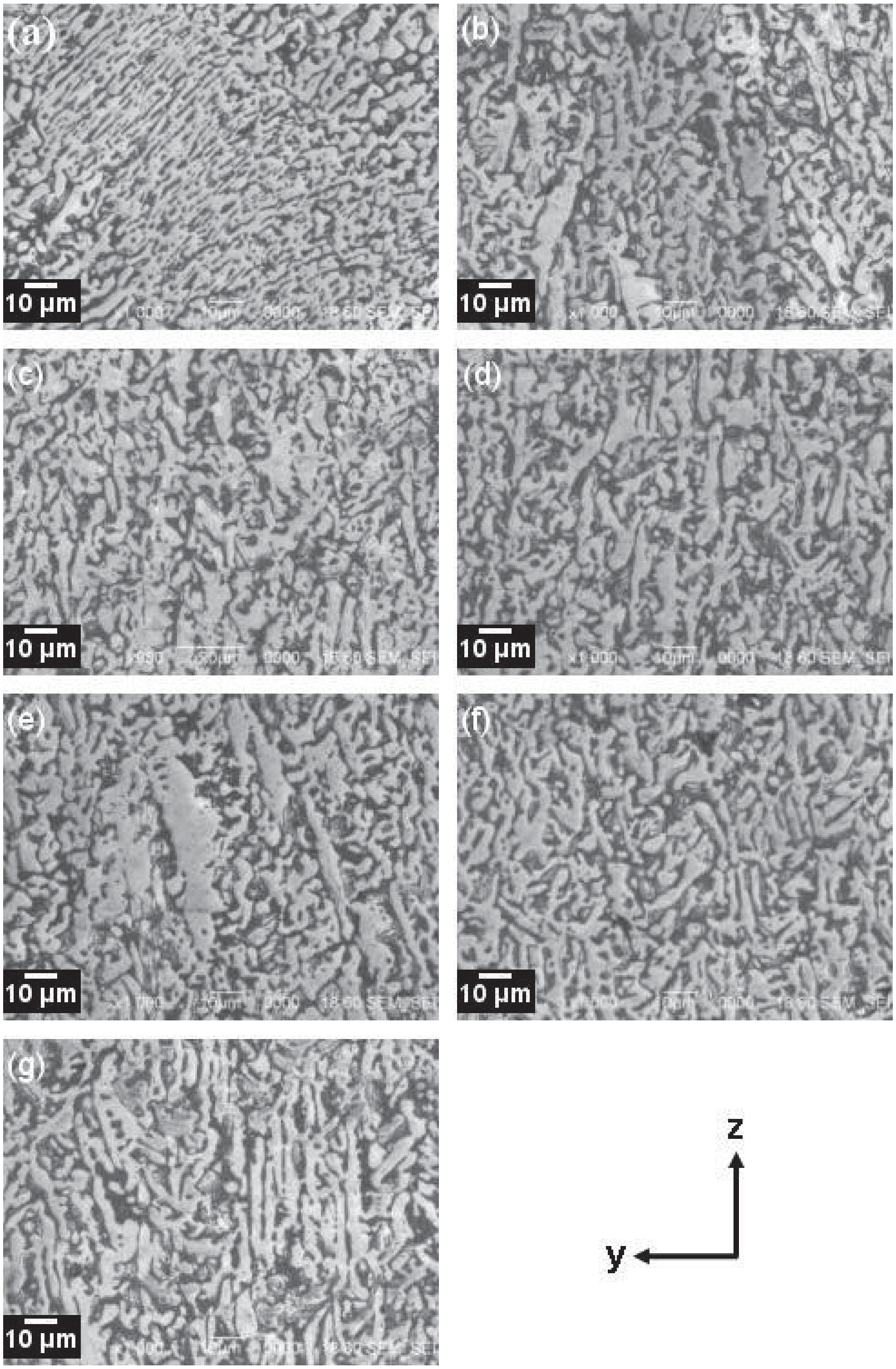

Fig. 4-14: SEM secondary electron micrographs, ×1000 magnification, showing the seven regions in Fig. 12. Regions 2 through 7, (b)-(g) respectively, have similar microstructures but with slightly different orientation. Region 1 (a) is near the Y-shape and has a structure that is dissimilar to the other six regions. The Al_2O_3 phase (light gray) has an overall growth in the z-direction with some branching in the x and y directions.

4.4.2. Y-shaped Boundary

Scanning electron microscopy was also utilized to investigate the Y-shaped boundary features originally discovered by stereo-OM. In both samples, the Y-shaped feature is quite uniform in areas away from the sample corners. It is primarily formed by the interface among Al_2O_3 colonies meeting at the intersection of the reaction front. The feature is accentuated by a continuous series of voids, illustrated in Fig. 4-15. At an increased magnification, see Figs. 4-15(c) and (d), it is apparent that the voids are not completely empty but contain an interconnected network of some phase or phases. In other words, the porous regions seem to missing one of the usually found two co-continuous phases, leaving a porous single phase network. The plate-like Fe-rich features in the Al-7.5wt.%Fe sample transverse the boundary indicating a fluid flow of molten metal during processing.

In the Al-7.5wt.%Fe sample, the boundary feature near the sample's corners is consistent with the findings in the bulk of the sample, shown in Fig. 4-17. The Y-shape is formed by the interface among Al_2O_3 colonies and emphasized by a series of voids. In the case of the Al sample, the boundary feature is considerably different near the sample's corners. Fig. 4-18 demonstrates that the Y-shape in the Al sample exhibits extensive cracking and high porosity. As eluded to in section 4.4.1., features formed along the Y-shaped boundary that have significantly different grain structure compared to the rest of the material. These features contain a dense alumina phase that stretches linearly and does not exhibit the typical branching associated with the three-dimensional network. The features are largest near the intersection of the boundary lines and become increasingly smaller towards the outer corners. Since the homogeneity of the material is compromised, the features are considered defects.

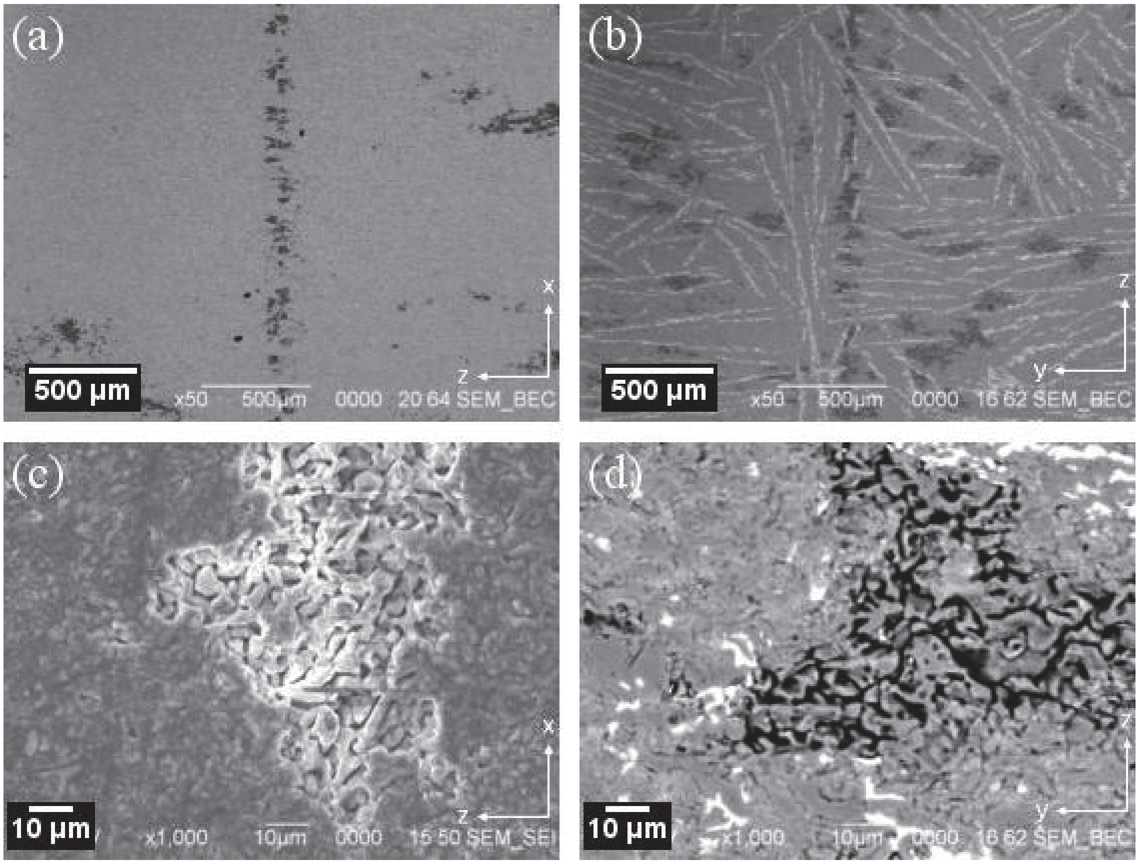

Fig. 4-15: SEM backscatter micrographs, ×50 magnification, showing the series of voids along the boundary feature in the Al (a) and Al-7.5wt.%Fe (b) samples. At ×1000, the SEM secondary electron micrograph of the Al sample (c) and SEM backscatter micrograph of the Al-7.5wt.%Fe sample (d) shows that that the “voids” are not entirely empty but contain an interconnected network of some phase or phases.

The SEM micrograph in Fig. 4-19 reveals an interface between two defect features along the Y-shape. The left-hand feature contains an elongated Al phase compared to the shorter more round Al phase in the right-hand feature. This indicates that the dense Al_2O_3 structure grew in different directions. Based on the location of the features, and considering the method by which the sample was sectioned and examined, the formation of these features can be related to the intersection of the three growth directions. A more thorough understanding of the formation mechanism may offer better insight into why these features exist only in the Al sample.

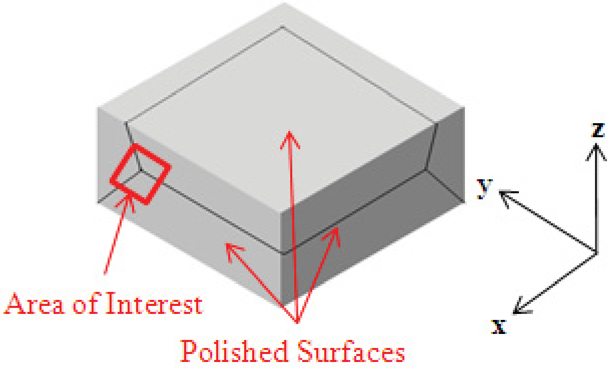

Fig.4-16: Illustration depicting the area examined in Figs. 4-17, 4-18, 4-19.

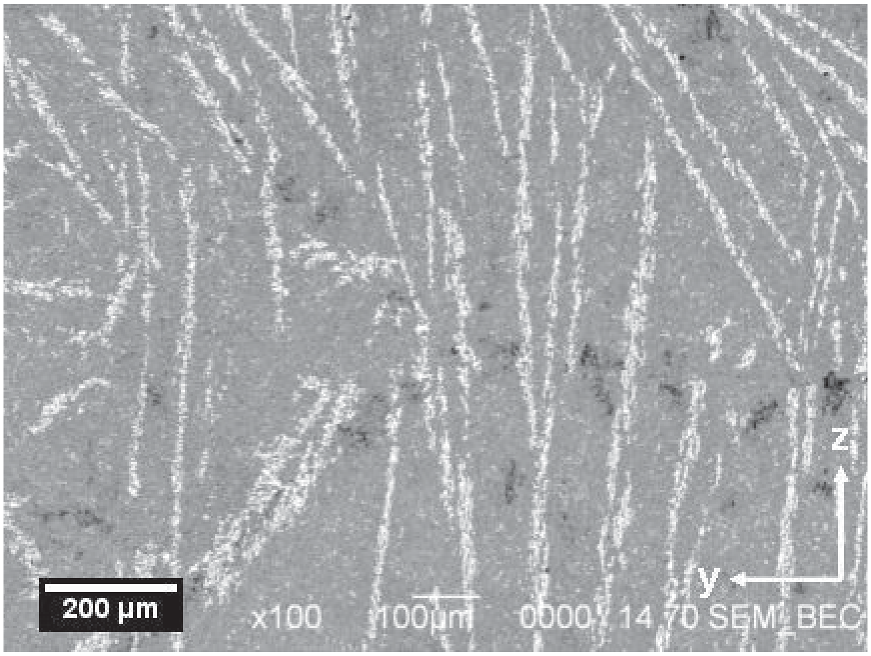

Fig. 4-17: SEM secondary electron micrograph, ×100 magnification, showing the Y-shaped boundary feature near a corner of the Al-7.5wt.%Fe sample. The boundary feature, accentuated by a series of voids (black), is uniform throughout the entire sample.

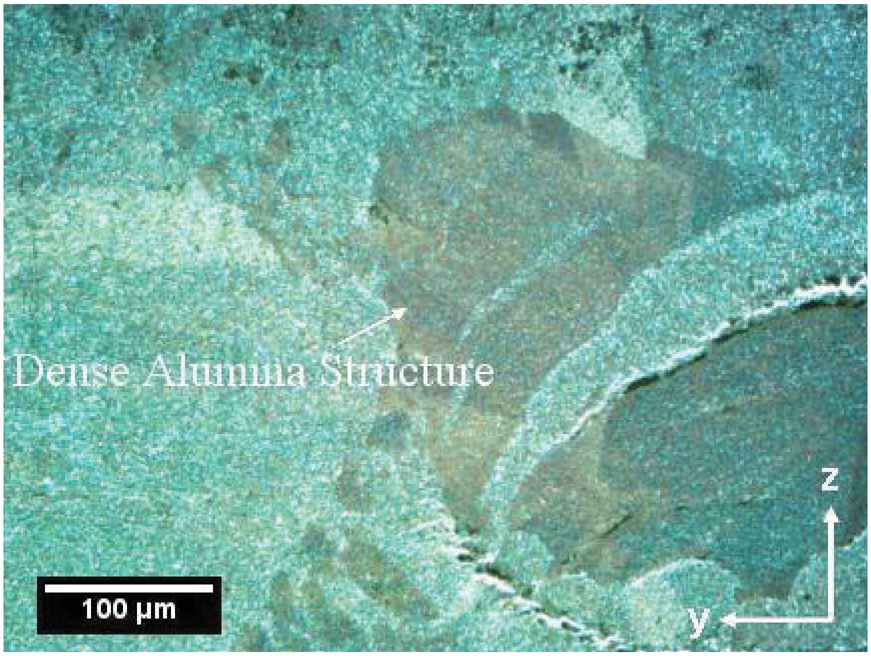

Fig. 4-18: Brightfield OM micrograph showing the Y-shaped boundary feature near a corner of the Al sample. Near the corners, the boundary feature exhibits defects, cracking, and features that exhibit dense Al_2O_3 microstructures.

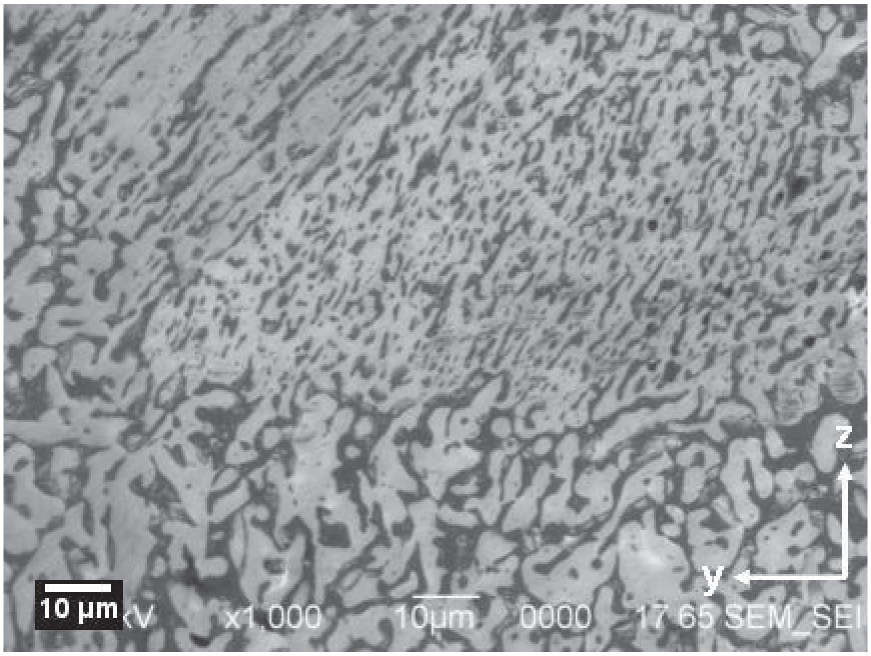

Fig. 4-19: SEM secondary electron micrograph at ×1000 magnification showing the intersection of two dense Al_2O_3 phases (light gray) along the Y-shaped boundary of the Al sample. The microstructure of these features is vastly different than the rest of the material.

4.5. Focused Ion Beam Polishing

Ultra fine polishes of the Al and Al-7.5wt.%Fe samples accomplished by ion milling are shown in Fig. 4-20. The FIB polish exposed fine details that otherwise could not be observed with mechanical polishing, including precipitated Si particles, micro-scale cracking, and grain boundaries. Because the FIB polished area is relatively small, it is not possible to make concrete correlations between the two samples. Both samples exhibit precipitated silicon particles, which are elongated in the Al sample and compact in the Al-7.5wt.%Fe sample, demonstrated by the micrographs in Fig. 4-21 and 4-22. EDS was used to confirm the elemental composition of the phases in the Al-7.5wt.%Fe sample. The large Al peak in the Si-containing spectrum may be attributed to an overlap of phases or an indication that a metastable Al-Si intermetallic has formed. Cracking in the alumina phase is revealed in the FIB secondary electron micrograph shown in Fig. 4-23. Since aluminum has partially filled the crack, it logically follows that the cracking occurred during the RMP process. The cracking is not noticeable in the FIB polished area of the Al-7.5wt.%Fe sample, though more areas would need to be examined to determine if this is a consistent characteristic. Fig. 4-24 is a FIB secondary electron micrograph that has been slightly tilted to induce ion channeling effects. The contrast achieved by titling the sample reveals grain boundaries in the aluminum phase. Grain boundaries are not observed in the alumina phases, which signifies that the alumina grains may be continuous or at the very least are larger than the aluminum grains.

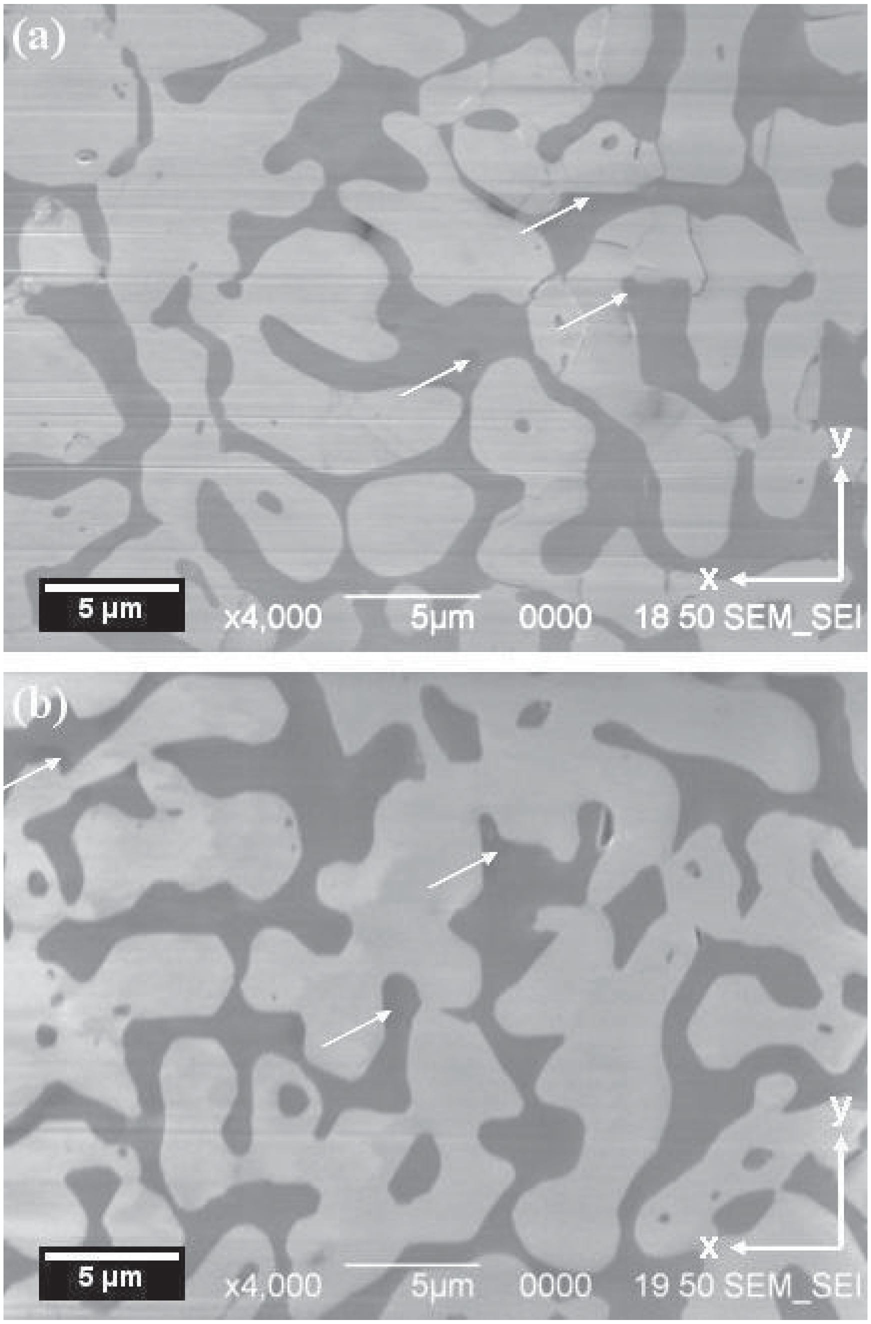

Fig. 4-20: SEM secondary electron micrographs, ×4000 magnification, showing FIB polished areas of the Al sample (a) and an iron-less region of the Al-7.5wt.%Fe sample (b). The Al (gray) - Al_2O_3 (light gray) network contains small particles of precipitated Si (dark gray) that are barely visible at this magnification. Some of the Si particles are marked by arrows. The horizontal lines are defects created during the ion milling process.

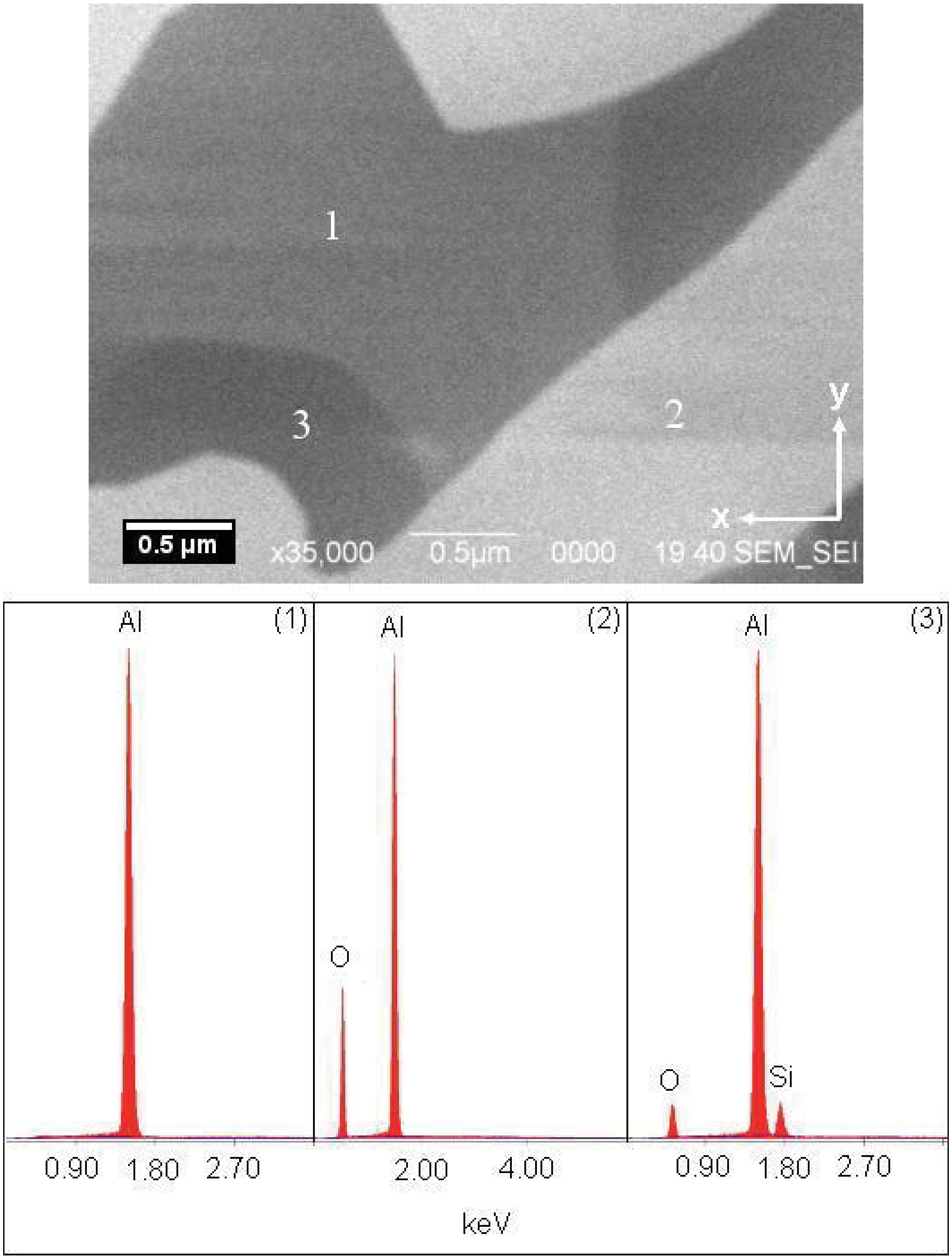

Fig. 4-21: (Top) SEM secondary electron micrograph, ×35,000 magnification, showing an area of the FIB polished Al-7.5wt.%Fe sample that contains precipitated Si particles. (Bottom) EDS analysis identified an Al phase (gray), Al_2O_3 phase (light gray), and a Si-rich phase (dark gray).

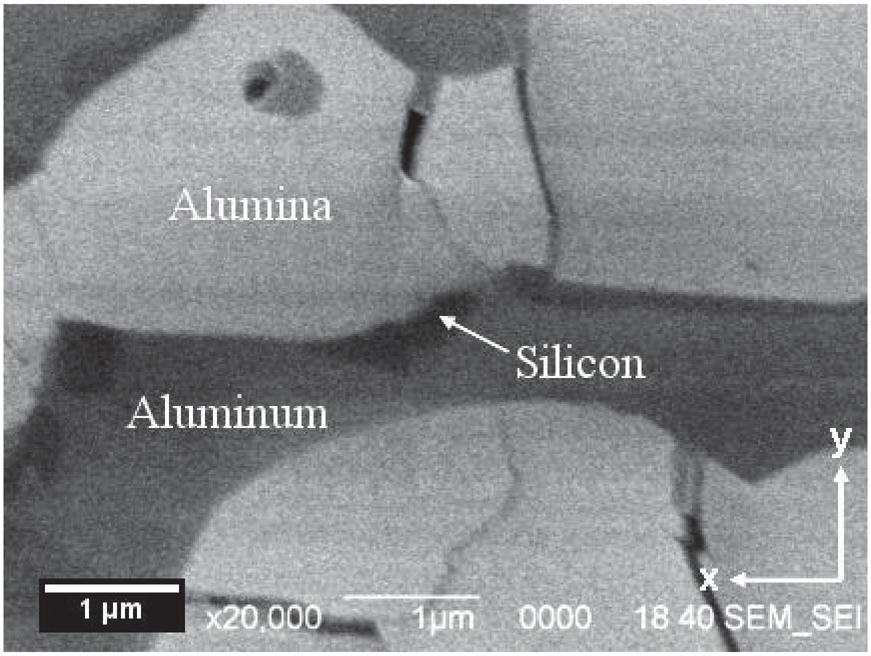

Fig. 4-22: SEM secondary electron micrograph, ×20,000 magnification, of a FIB polished area from the Al sample. The Al_2O_3 phase (light gray) shows extensive cracking. Precipitated Si particles (dark gray) are contained within the Al phase (gray).

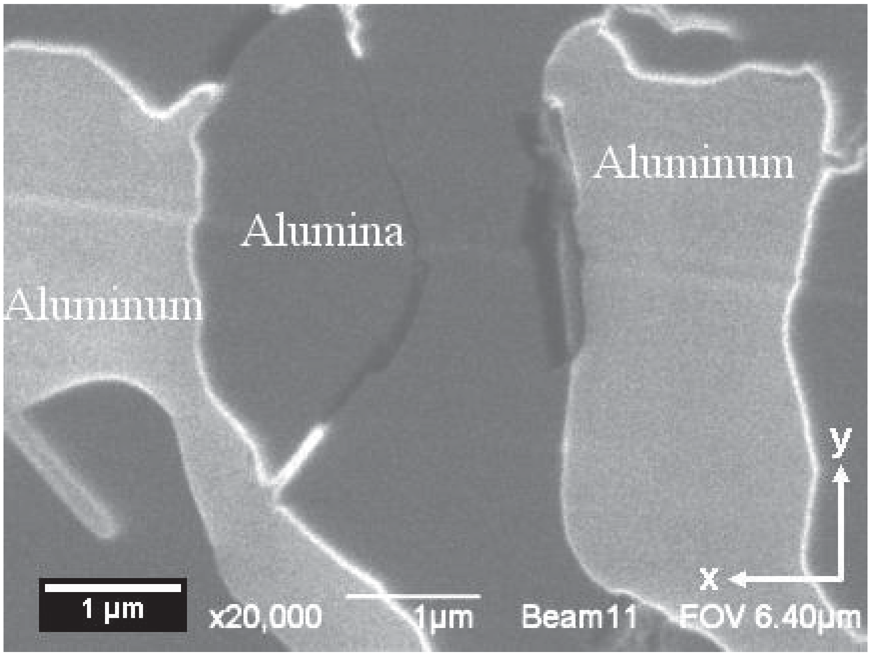

Fig. 4-23: FIB secondary electron micrograph, ×20,000 magnification, showing Al partially filling a crack in the Al_2O_3 phase. This indicates that the cracking observed in the Al_2O_3 phases occurred during the RMP processing.

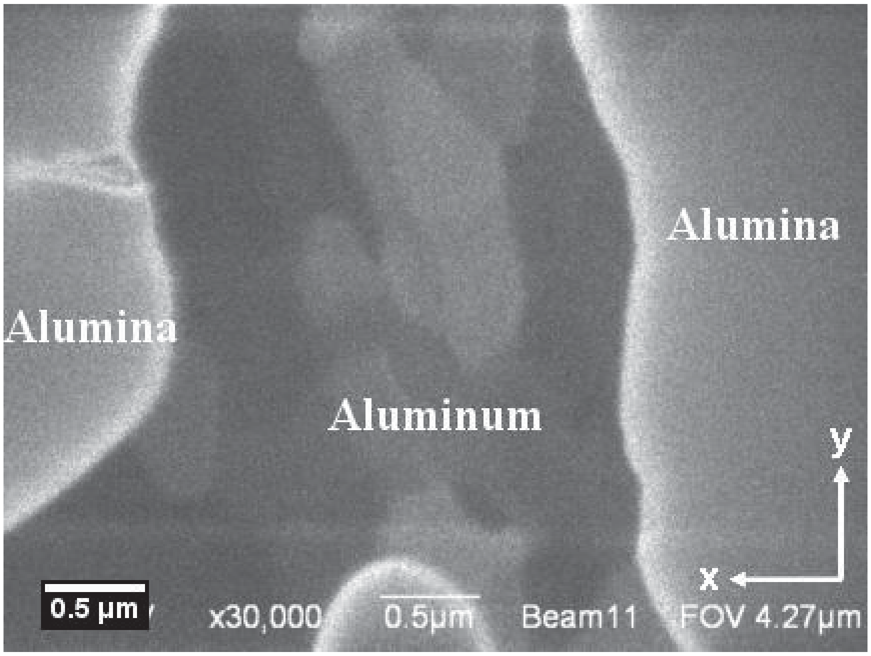

Fig. 4-24: FIB secondary electron micrograph of the FIB polished Al sample tilted to induce ion channeling. Ion channeling exposed submicron-sized grains in the Al phase.

In an attempt to better understand the distribution of phases, the FIB polished SEM micrographs in Fig. 4-25 have been converted into grayscale images. The Al_2O_3 and Al phases and voids are each represented by a gray-level. Histograms of the images were calculated using Image-J software[88] and were used to approximate the volume of the three components. The results from the image analysis are shown in Table 4-1. In both samples, the percent area of Al_2O_3 and Al is about 65% and 35%, respectively. This relates well to the expected volumetric distribution.

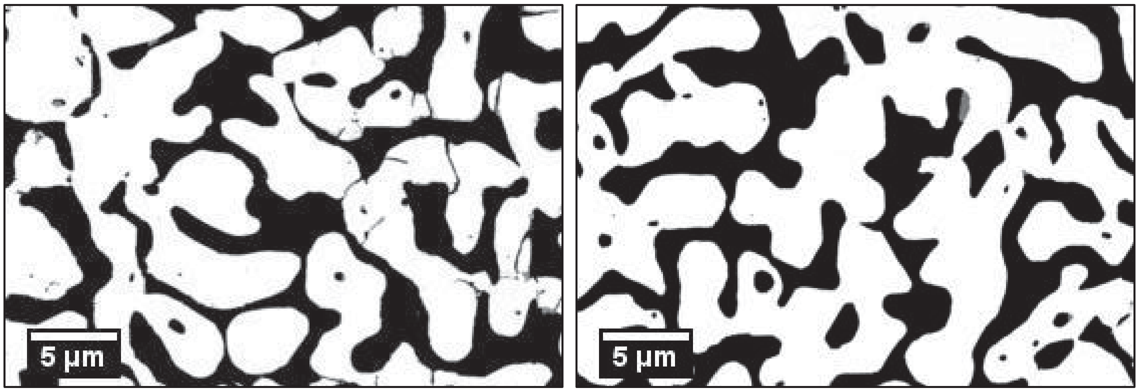

Fig. 4-25: 8-bit color images of the FIB polished surface from the Al (left) and Al-7.5wt.%Fe (right) samples representing the distribution of Al_2O_3 (white), Al + Si (black), and voids (gray).

Table 4-1: Image Analysis

	White (Al_2O_3)	**Black (Al + Si)**	**Gray (Voids)**	**Total**
Al Sample				
Counts	727233	391843	2204	1121280
Percent Area	64.9	34.9	0.2	100.0
Al-7.5wt.%Fe Sample				
Counts	7303160	386425	1979	1118720
Percent Area	65.3	34.5	0.2	100.0

4.6. Vickers Indentation Hardness

The results of the Vickers hardness testing are displayed in Table 4-2. The average hardness of the Al and Al-7.5wt.%Fe samples is 468.2 HV and 485.5 HV, respectively. The large standard deviations, 41.2 for Al and 63.2 for Al-7.5wt.%Fe, make the averages statistically indistinguishable, though it was expected that the Al-7.5wt.%Fe have a slightly higher hardness due to the iron rich phases. The hardness is an average of the combined phases since the indentation is much larger than the individual grains, illustrated in Fig. 4-26. There was no attempt to include or exclude the iron-rich regions in the Al-7.5wt.%Fe sample; therefore, the hardness value represents random sampling. Of the 25 indentations made in each sample, 3 in the Al sample and 2 in the Al-7.5wt.%Fe were deemed unacceptable due to either excessive cracking or an asymmetrical indentation. Statistical analysis was performed on the calculated HV values. As a result, one additional indentation was excluded from each sample because they were statistical outliers, as demonstrated by the boxplots in Fig. 4-27. Histograms showing the distribution of data are displayed in Fig. 4-28. Fig. 4-29 plots the hardness values versus their distance from the outer edge. The graph indicates that the materials have a slightly lower hardness less than 1 mm from the edge, while the bulk of the sample contains a more uniform distribution. A common flaw during mechanical polishing is a slight rounding of the sample edges. If this occurred, the resulting uneven surface can explain the decrease in hardness near the edges.

Table 4-2: Vickers Indentation Hardness Results

	Al	**Al-7.5wt.%Fe**
Mean	468.2	485.5
Standard Deviation	41.2	63.2
Minimum	397.2	332.5
Maximum	538.1	573.7
Range	140.9	241.2
Satisfactory Indentations	21	22
Total Indentations	25	25

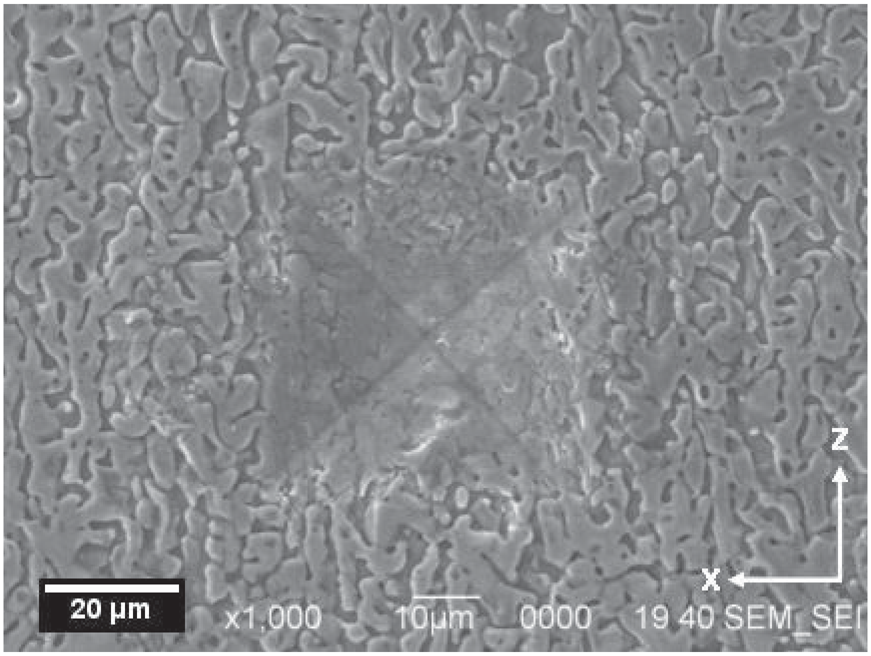

Fig. 4-26: SEM secondary electron micrograph, ×1000 magnification, showing a Vickers hardness indentation. The hardness represents an average of the entire material since the indentation is much larger than the individual phases.

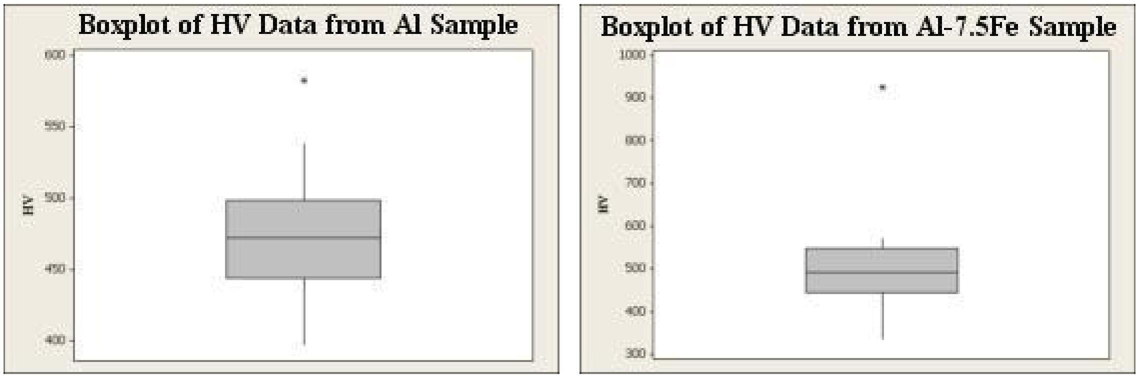

Fig. 4-27: Boxplots from Vickers indentation hardness (HV) data. The outliers, indicated by a dot, were omitted from the calculations.

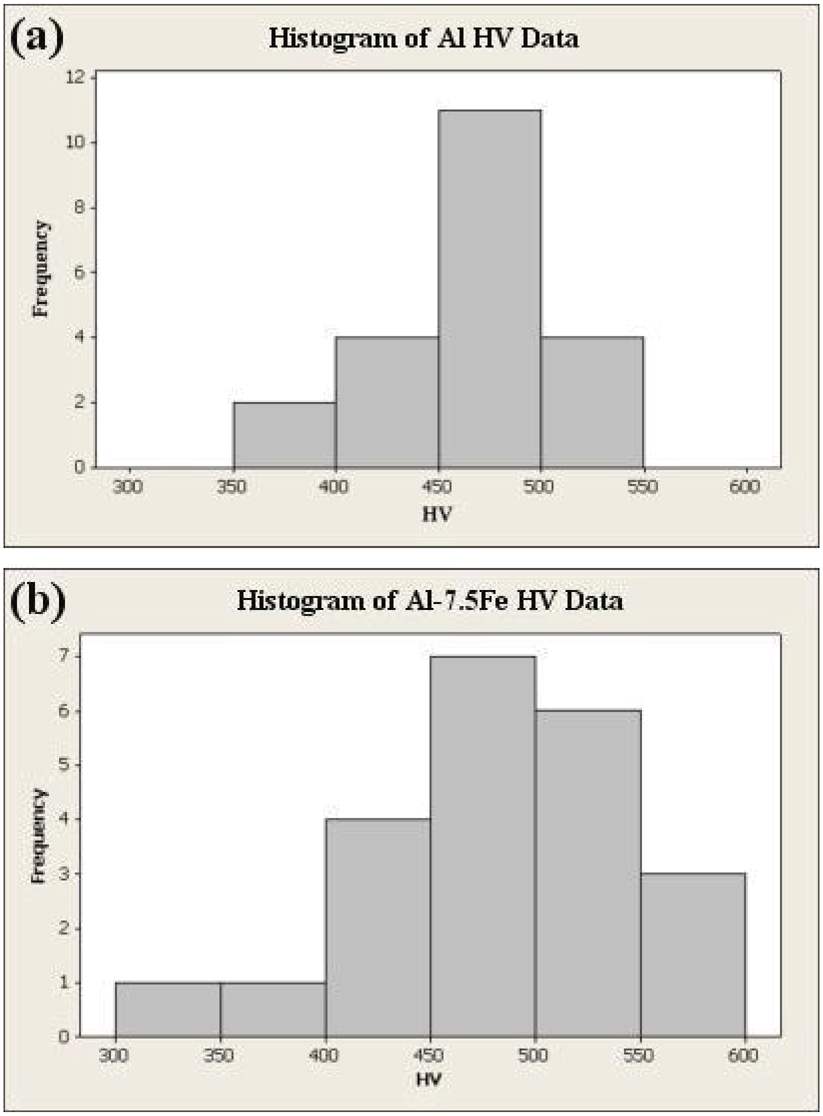

Fig. 4-28: Histograms showing the distribution of Vickers indentation hardness data for the Al (a) and Al-7.5wt.%Fe (b) samples.

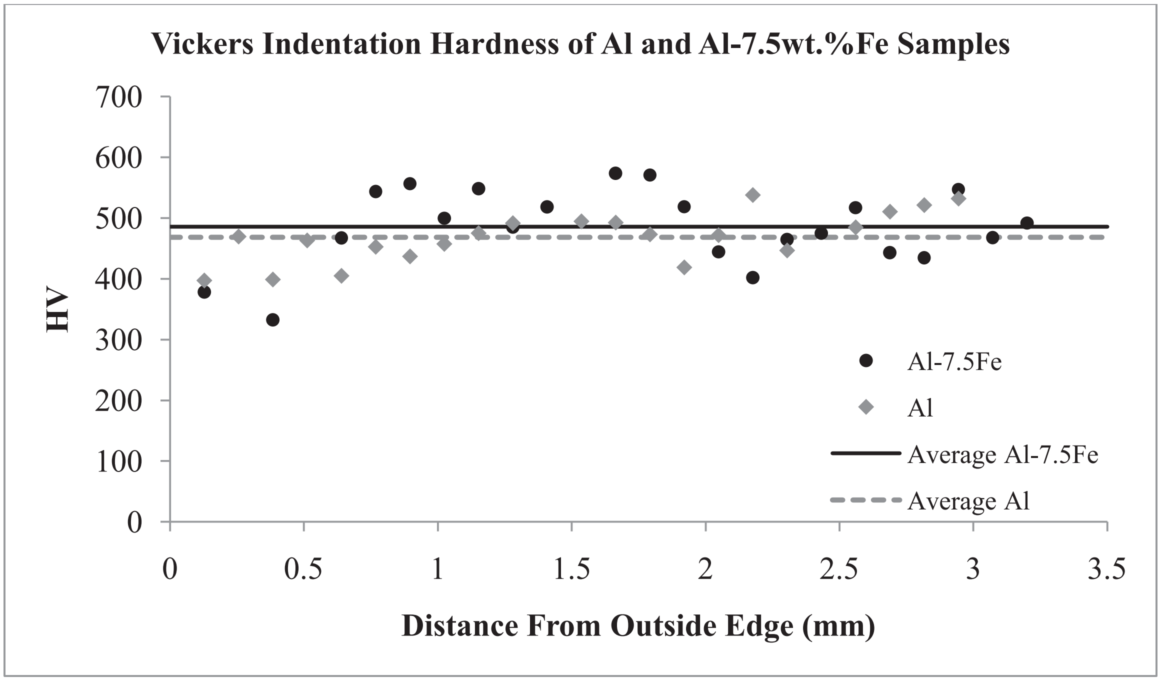

Fig. 4-29: Graphical representation of the HV measurements taken from the Al and Al-7.5wt.%Fe samples. The data indicate that in both samples the hardness is slightly less near the edges compared to the bulk.

4.7. Supplementary Materials

4.7.1. Al-7.5wt.%Fe Melt Sample

The melt sample pertaining to the Al-7.5wt.%Fe transformation was examined using SEM, Fig. 4-30 and EDS, Fig. 4-31. The SEM micrograph in Fig. 4-30(a) shows that large needle-shaped Fe-rich phases exist in an Al matrix. At increased magnification, shown in Fig. 4-30(b), smaller Fe-rich phases and particles of Si can be observed. This confirms that Si is diffusing away from the reaction front and into the metal bath. The Si particles are small, so it cannot be determined if the Al peak in the EDS spectrum belongs to the neighboring metal or if an Al-Si intermetallic has formed.

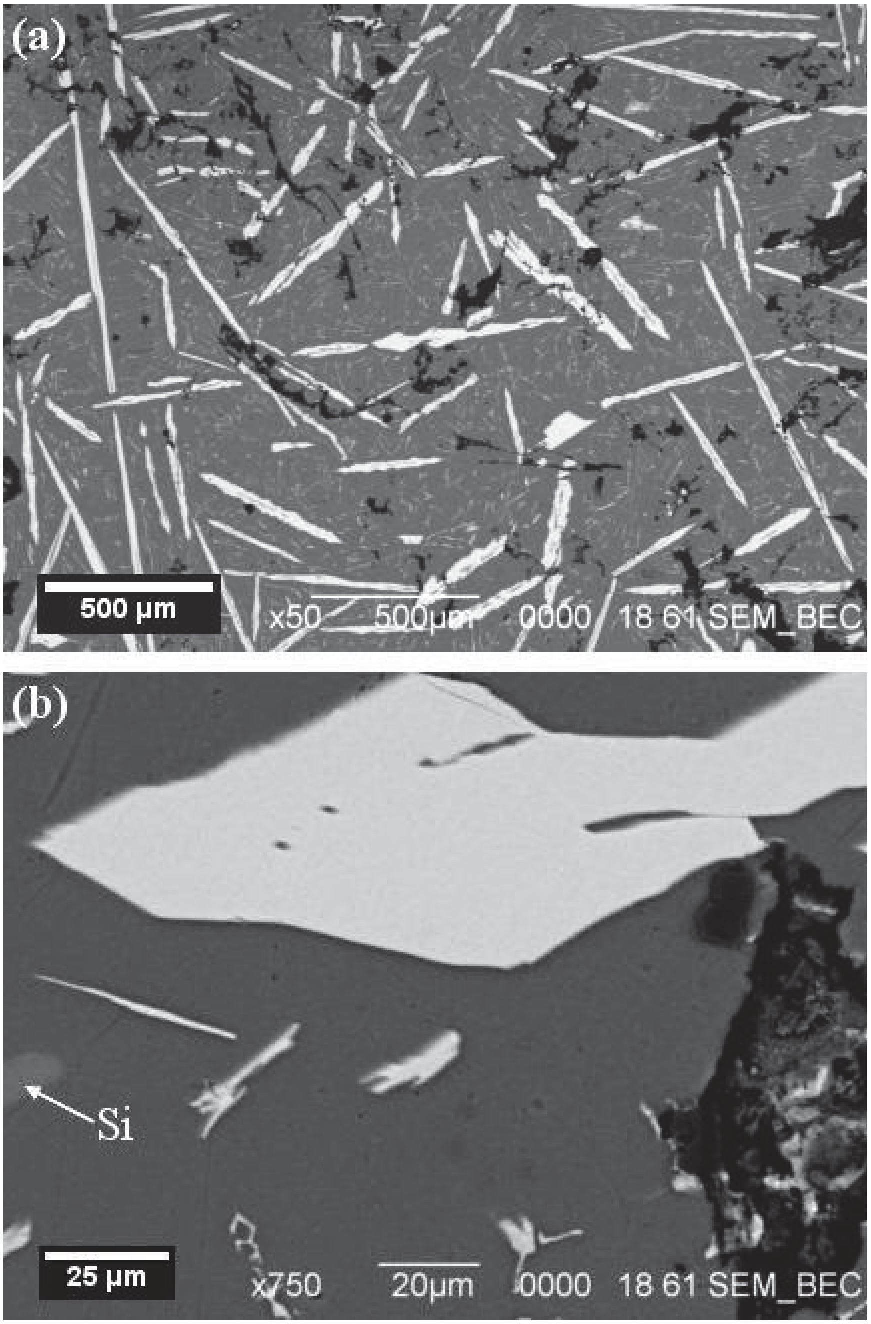

Fig. 4-30: (a) SEM backscatter micrograph, ×50 magnification, showing large Fe-rich (white) needle shaped phases. (b) SEM backscatter micrograph, 750× magnification, showing smaller similarly shaped Fe-rich (white) phases and precipitated Si particles (labeled). The large black areas are voids.

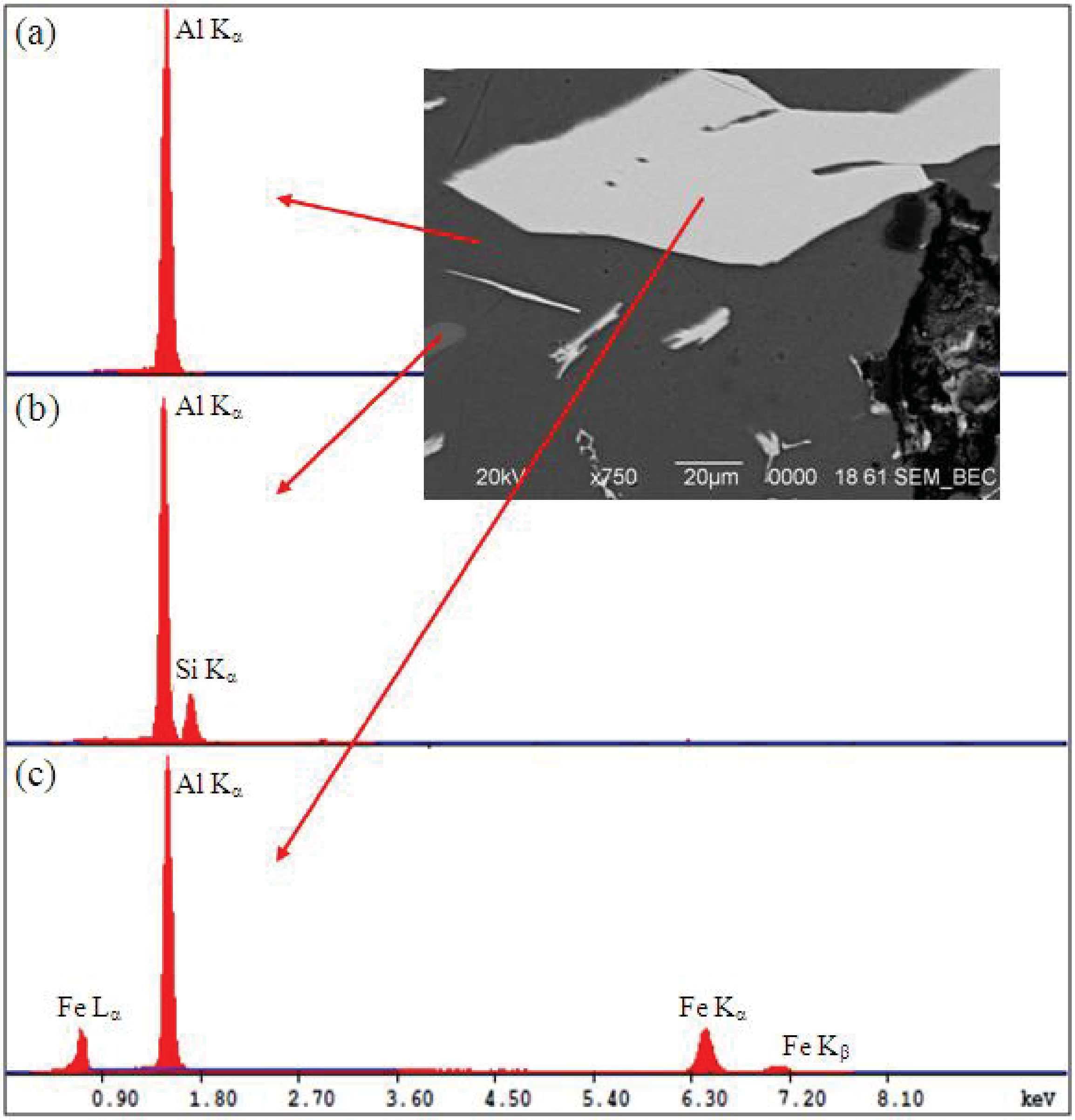

Fig. 4-31: EDS spectra from the dark gray (a), light gray (b), and white (c) regions of the Al-7.5wt.%Fe melt sample. The characteristic x-ray peaks indicate an Al metal phase, a Si-rich phase, and an Al-Fe-intermetallic phase.

4.7.2. Al-25wt.%Si Sample

To offer a third comparison to the Al and Al-7.5wt.%Fe samples, a brief investigation of the Al-25wt.%Si sample was conducted. The stereo optical micrograph,

Fig. 4-32, shows that the Y-shaped boundary feature and Al_2O_3 growth colonies observed in the first two samples are also exhibited in the Al-25Si sample. In addition, dark clusters can be observed throughout the sample bulk. Examination of the Y-shaped feature shows that the series of voids along the boundary lines reported in the other samples is absent. Instead, the boundary feature is formed solely by the borders of the Al_2O_3 colonies, as illustrated by Fig. 4-33. Based on microscopic analysis, the Al-25wt.%Si sample contained significantly less porosity than the Al and Al-7.5wt.% samples. EDS elemental mapping, seen in Fig. 4-34, shows that the clusters observed by stereo optical microscopy are Si-rich. It is likely that these clusters contain essentially pure Si since solubility of Si in Al is extremely low at room temperature.

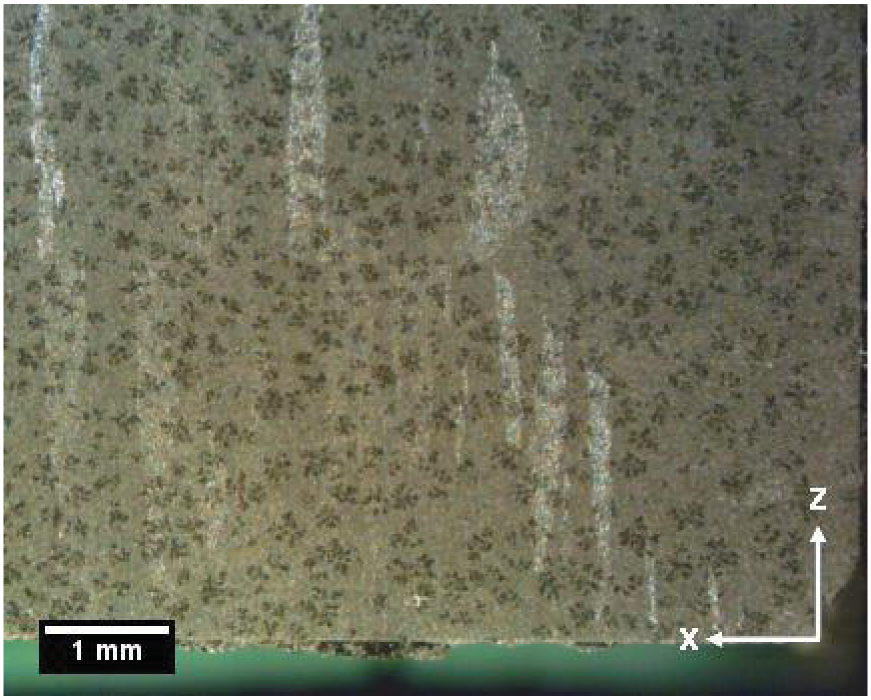

Fig. 4-32: Stereo-OM micrographs showing a polished cross-section of the Al-25wt.%Si sample revealing the Y-shaped boundary feature and bright columns, which were also detected in the Al and Al-7.5wt.%Fe samples. Dark clusters consistent throughout the sample bulk can be observed.

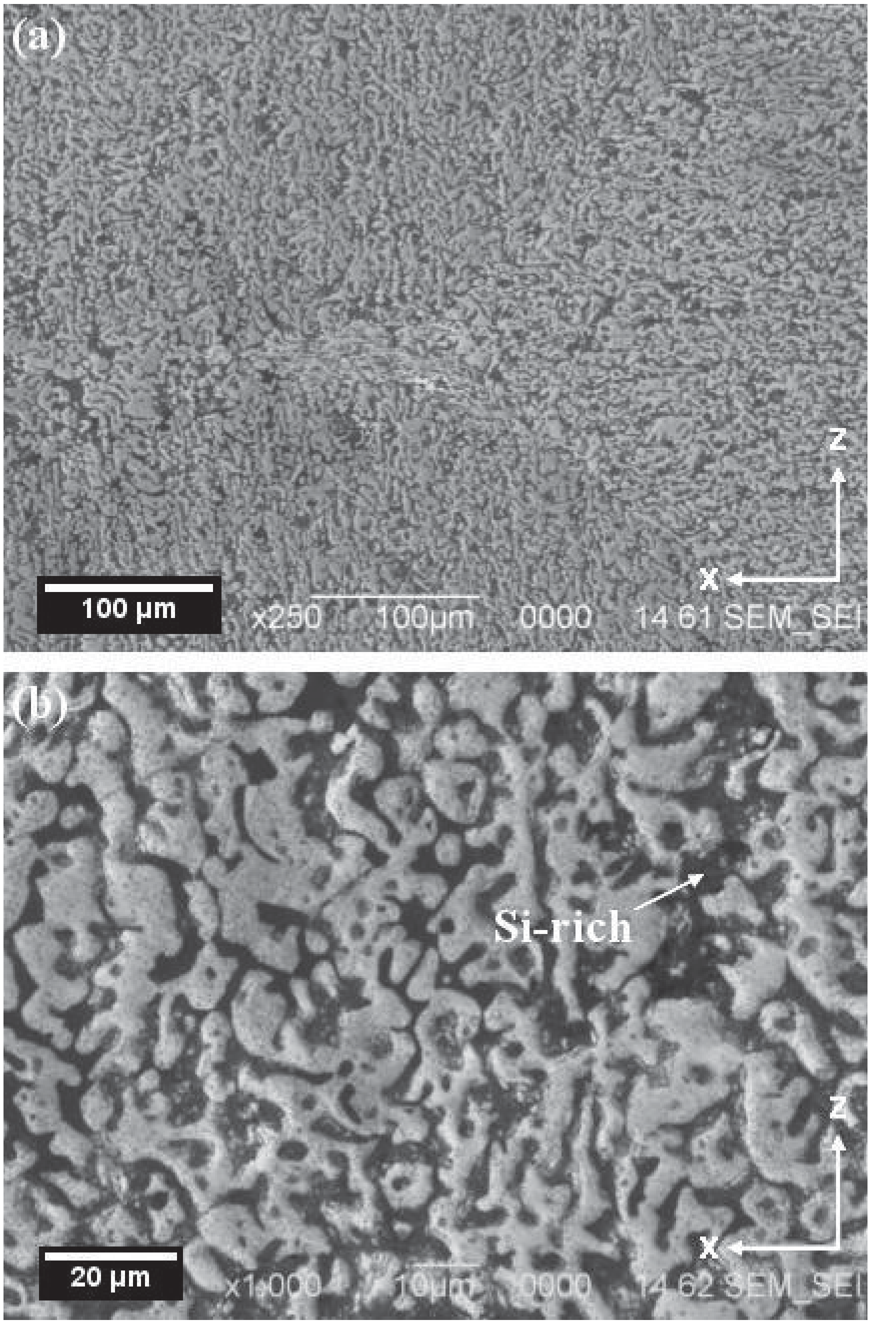

Fig. 4-33: (a) SEM secondary electron micrograph of the Al-25wt.% sample, ×250 magnification, showing the formation of the Y-shaped boundary feature by the intersection of Al_2O_3 growth colonies. (b) SEM secondary electron micrograph, ×1000 magnification, showing the Al_2O_3 (light gray) – Al (gray) network with an overall growth in the z-direction. Interconnected Si-rich (dark gray) phases can also be observed.

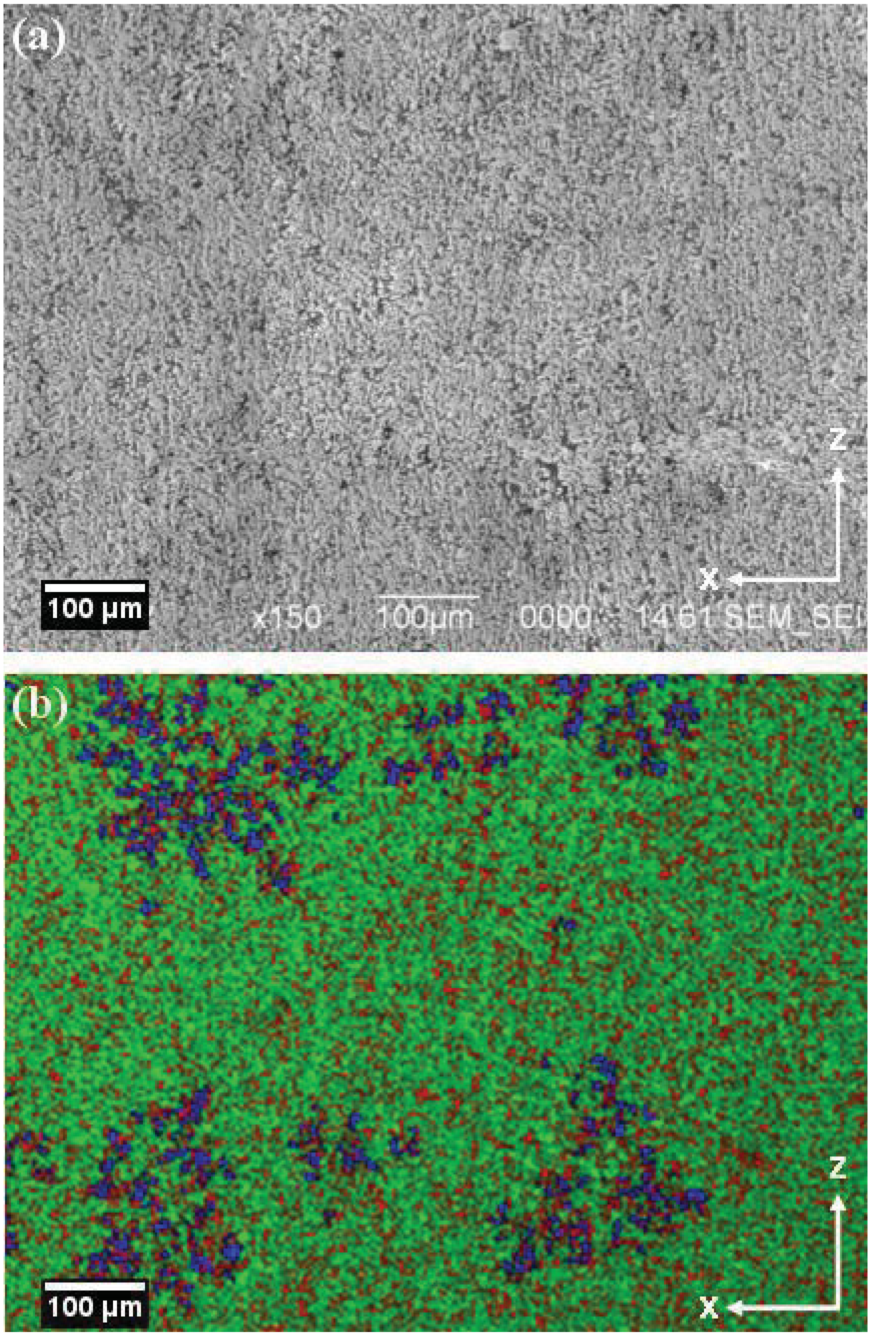

Fig. 4-34: (a) SEM secondary electron micrograph of the Al-25wt.%Si sample taken at ×150 magnification. (b) EDS elemental map showing the distribution of O – red, Al – green, and Si - blue in the micrograph above. The Si-rich phases correspond to the dark clusters observed in stereo-OM.

4.7.3. Partially Transformed Al(2hr) Sample

The Al(2hr) sample, which was stopped after 2 hours of reaction, is useful for examining the transformation mechanisms during RMP processing. Stereo optical microscopy, Fig. 4-35, shows the development of the bright Al_2O_3 growth colonies and Y-shaped boundary-like feature. A strip of untransformed clear fused quartz preform remains symmetrically positioned at the center of the sample. Brightfield optical microscopy, shown in Fig. 4-36, highlights the reaction interface and demonstrates that the reacted zone is not a flat layer. Instead, pockets of reacted materials form along the reaction front. The reaction interface was analyzed using polarized optical microscopy and the morphology of the interface is displayed in Fig. 4-37. Polarized microscopy reveals an uneven layer that forms between the pockets and the transformed product. The contrast achieved by polarized light microscopy shows that the pockets and the layer are anisotropic materials, which indicates that they are at least partially crystalline with a non-cubic structure. Furthermore, the morphologies of the pockets and the layer are dissimilar suggesting that they are different in some way.

The product phases immediately near the transition zone have a different structure than those away from the reaction front, see Fig. 4-38. The Al_2O_3 phases near the reaction front have sharper features and are jagged in nature. The areas away from the reaction front maintain Al_2O_3-Al structures equivalent to those in the Al, Al-7.5wt.%Fe, and Al-25wt.%Si samples. The SEM backscatter micrograph in Fig. 4-39(a) shows a contrast difference between the pockets and the transition layer. The layer exhibits minimal cracking compared to the extensive cracking found in the pocketed areas. An aggregated boundary has formed between the transition layer and the transformed product.

Phase cluster analysis was performed on the transition zone, shown in Fig. 4-39(b). As expected, a large amount of displaced Si is detected near the reaction front in the pockets, layer, and transformed areas. From the phase map it appears that overall the Si is quite disperse with a few regions of high concentration. A positive identification of the pocketed and layered phases can not be determined by EDS. The only conclusion that can be made is that the phases contain varying amounts of Al and O with appreciable amounts if Si interspersed throughout. Further investigation to determine the exact composition of these phases will be crucial in understanding how ceramic-metallic IPC's are produced by RMP processing, and may offer insight into predicting how preform and alloying additions can alter the final products.

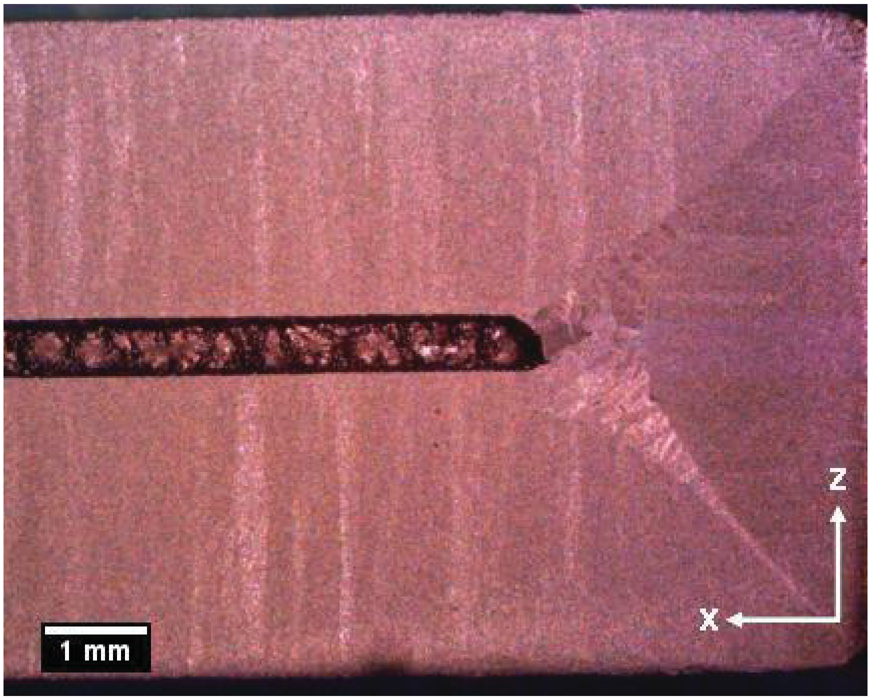

Fig. 4-35: Stereo-OM micrograph of the partially transformed Al sample showing the development of the bright Al_2O_3 growth colonies and Y-shaped boundary-like feature. A section of untransformed clear fused quartz preform is symmetrically positioned in the center of the sample.

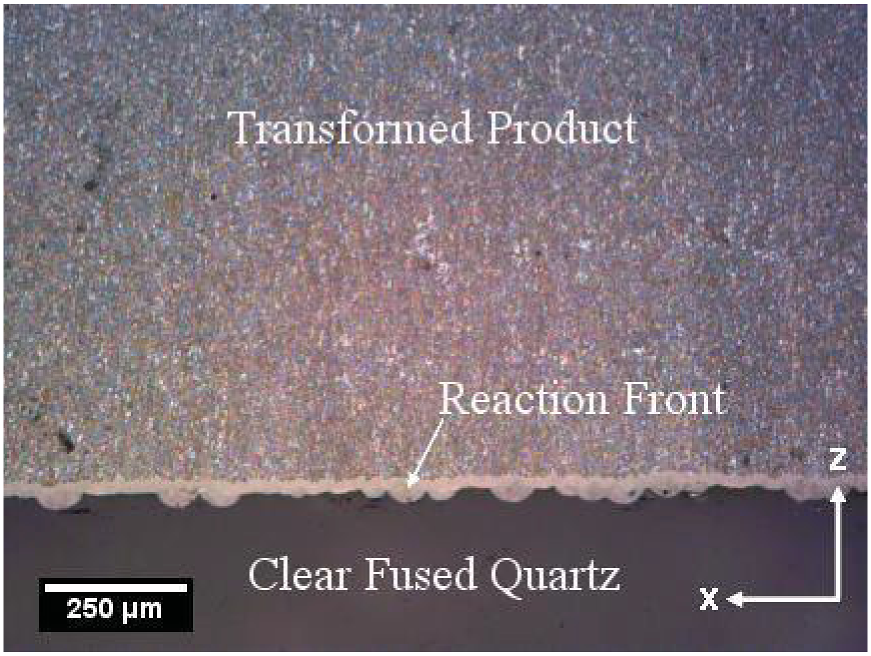

Fig. 4-36: Brightfield-OM micrograph of the partially transformed Al(2hr) sample. Pockets of transformed material have formed along the reaction front.

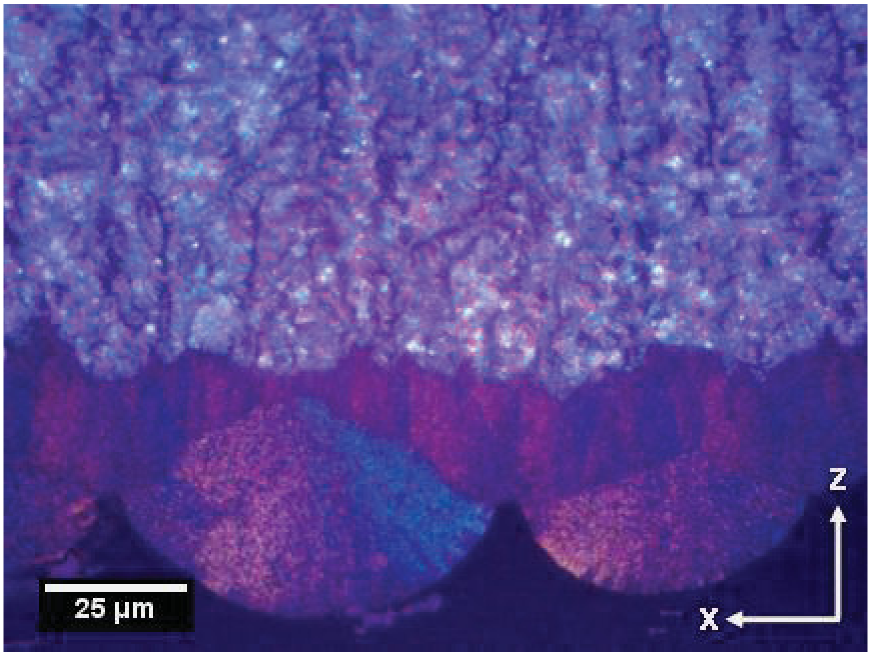

Fig. 4-37: Polarized light-OM micrograph of the Al(2h) sample showing that an uneven transition layer and pockets have formed between the transformation product and the clear fused quartz preform.

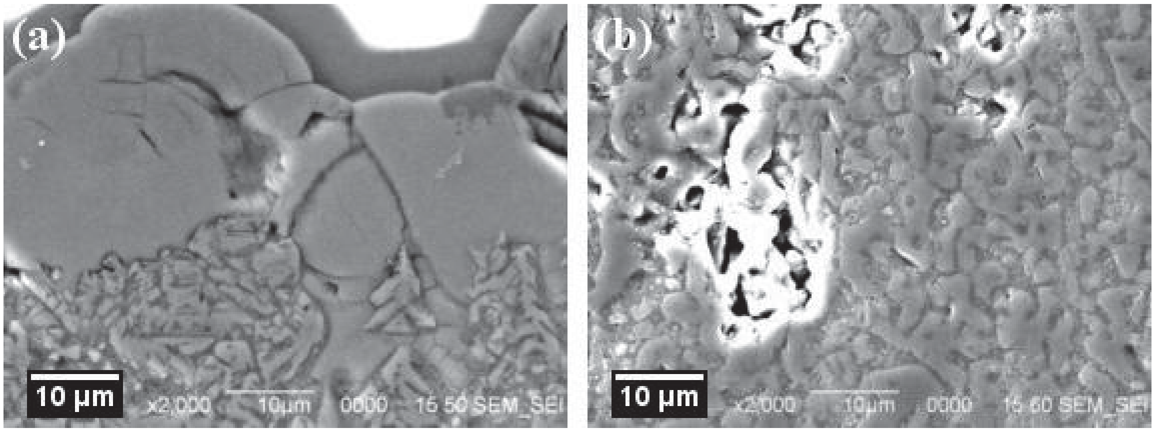

Fig. 4-38: SEM secondary electron micrographs of the Al(2hr) sample, ×2,000 magnification, showing the Al_2O_3-Al structure near the reaction interface (a) and away from the interface (b). The Al_2O_3 grains near the interface have sharp features and appear jagged. The Al_2O_3 grains away from the reaction interface have softer features and resemble those found in the Al, Al-7.5wt.%Fe, and Al-25wt.%Si samples. The large feature in (b) is a void.

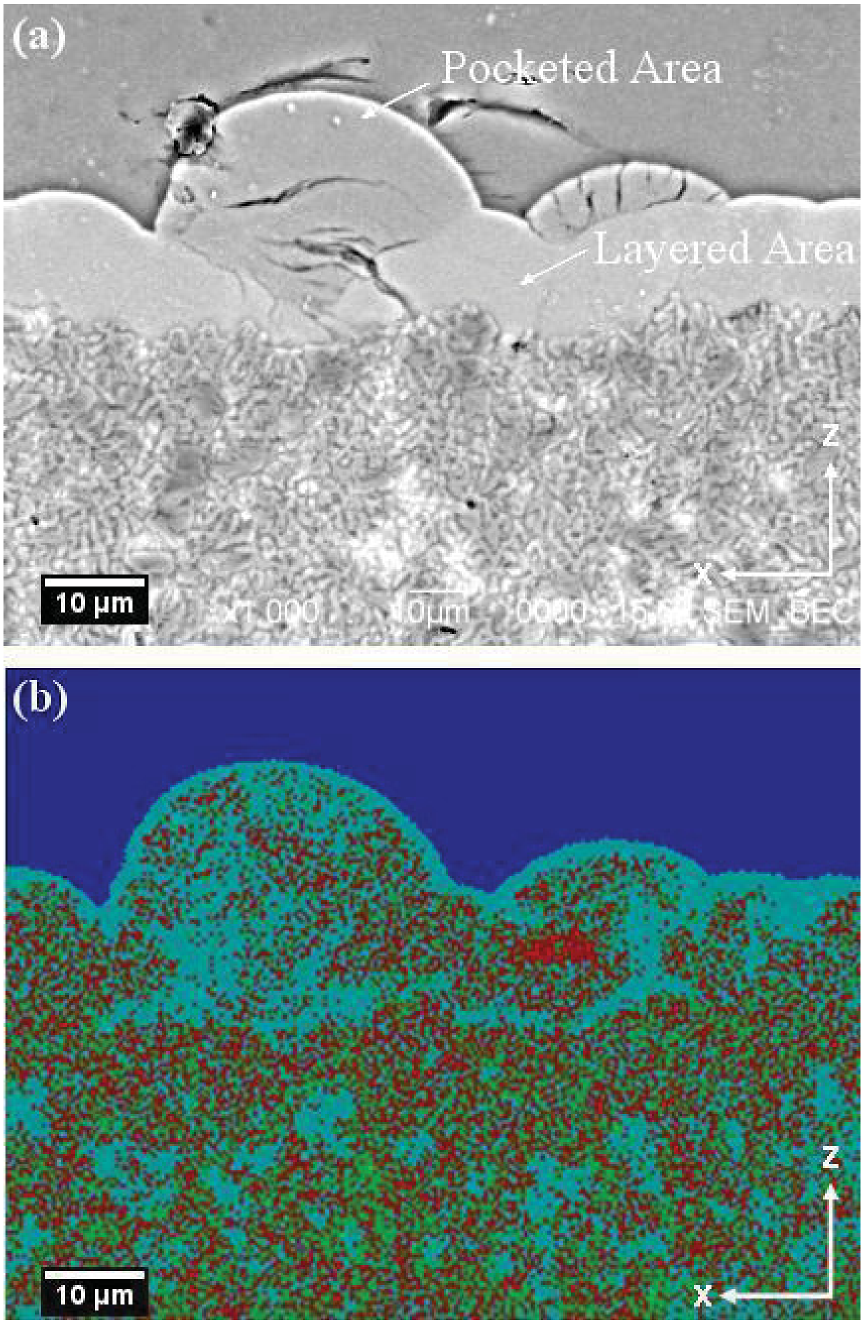

Fig. 4-39: (a) SEM backscatter micrograph of the Al(2hr) sample taken at ×1000 magnification. The pocketed areas show extensive cracking, while cracking in the layered area is minimal. (b) PCA using EDAX^{TM} software shows the distribution of Al metal (green), A – O phase (red), SiO_2 (blue), and Al – O – Si (cyan). The Al – O phase in the pockets and transition layer cannot be positively identified as Al_2O_3 by EDS alone. The distribution of the Si-rich phases and the contrast observed in the backscatter micrograph suggests that the transition zone may contain multiple phases.

4.8. Discussion

The results provided by the analysis of the Al and Al-7.5wt.%Fe samples present the opportunity for further discussion of certain topics. One aspect that deserves extra attention is the transformation mechanism that produces the interconnect network. The results presented in this work are in disagreement with the "cracking" mechanism presented by Breslin *et al.*[17] (see *section 2.3.2.*) for a number of reasons. First, the colonies of differently orientated Al_2O_3 phases are indicative of a growth pattern rather than systematic cracking. The overall consistency in the phases' shape, size, and geometry and smooth features are uncharacteristic of cracking. For example, the cracking in the Al_2O_3 phases observed in the FIB polished area of the Al sample does not resemble the channels formed by the microstructure. In addition, the direction and size of the cracking documented in pocketed transition areas of the Al(2hr) sample could not have formed the columnar Al_2O_3 phases present in the TCON samples. Furthermore, one would expect to see the layered area between the pockets and transformed material to show some sort of branched cracking, however, cracking of the layer is minimal. Finally, the large amounts of Si dispersed throughout the pocketed and layered transition zones suggests that the chemical reactions associated with the IPC microstructure are more complex than a simple displacement reaction.

The results from this experimentation coincide more closely with the results and explanation provided by Rapp *et al.*[43] (see *section 2.3.2.*). The observed reaction front in the Al(2hr) sample is clearly uneven, which is the prerequisite for Rapp's theory. Also, the jagged features of the Al_2O_3 phases near the reaction interface are better explained by the growth of the microstructure compared to a microstructure that forms by cracking. For instance, if it is hypothesized that the transport of O through Si is the limiting factor for Al_2O_3 growth, it would be reasonable to assume that the jagged features result from the O slowly collecting and reacting at the tips of the previously formed Al_2O_3 grains. Based on the PCA analysis of the Al(2hr), it can be theorized that some Al-Si-O compound or compounds have formed, either as a reaction step or during cooling. This is further supported by Rapp's report that a $NiFe_2O_4$ layer formed at the reaction interface between Fe and NiO, which also formed an IPC. A plausible explanation is that the Al_2O_3 network will form after enough Si diffuses away from the reaction front. While the information provided in this report cannot provide a definite reaction mechanism, it does provide a solid groundwork for future investigation.

Another feature that requires further discussion is the series of voids that form along the Y-shaped boundary in the Al and Al-7.5wt.%Fe samples. A proposed explanation is that the voids are formed by the volumetric contraction of the metallic phase during the cooling process. It is know that Al undergoes an approximate 6.6% volumetric contraction during freezing.[59] Therefore, if the metal phases cool and solidify from the outer edges first, then the volumetric contraction will pull molten metal from the inner core. Eventually, the solidification process will reach the middle of the sample and there will be no metal left to fill the voids resulting in pore formation. To further support this claim, it is known that Si content reduces the volumetric contraction of Al-Si alloys during freezing,[55] and it has been shown that the Al-25wt.%Si sample does not contain the series of voids at the boundary feature.

The role of Si in Al-Si alloys might help explain the differences in porosity throughout the bulks of the samples, as well. Al-Si alloys are often used in intricate casting processes because Si increases the fluidity and wetting properties of Al.[54] Consequentially, the Al-25wt.%Si sample showed the least porosity based on microscopic observation. This can be attributed to the combination of reduced volumetric contraction and better flow properties from the Si addition. On the other hand, based on microscopic observation the Al-7.5wt.%Fe showed the most porosity throughout the bulk of the material, refer to Fig. 4-5(a). From the Al-Fe binary phase diagram it is evident that several Fe-Al phases can solidify at higher temperatures than pure Al. The solidification of such phases can block the fluid flow of Al during cooling, and as a result the voids left by volumetric contraction cannot be filled by the remaining molten metal. In fact, many of the larger voids observed in Fig. 4-5(a) are surrounded by Fe-rich phases. The addition of alloying Fe has previously shown to improve the mechanical properties of Al_2O_3-Al based IPC's,[8] but these results also show that it is important to consider the implications Fe has on metal flow during processing.

Chapter 5: Conclusion

A detailed analysis of the microstructural properties of two ceramic-metallic IPC's produced by reactive metal penetration (RMP) was performed. Both materials were manufactured by Fireline TCON, Inc. of Youngstown, OH by immersing clear fused quartz preforms into molten metal baths at 1200 °C. The first was transformed in a commercially pure Al melt for 6 hours and the other in an Al-7.5wt.%Fe melt for 4.63 hours. Three supplementary materials were examined to better understand the properties of the Al and Al-7.5wt.%Fe samples. The supplementary materials include a piece of the Al-7.5wt.%Fe melt, a TCON material produced by the immersion of clear fused quartz in an Al-25wt.%Si melt, and partially transformed TCON material produced by the immersion of clear fused quartz in a pure Al bath.

Microscopic observation determined that the Al sample contains two interconnected phases that are continuous throughout the microstructure. As expected, EDS and XRD analysis confirmed that the phases are Al_2O_3 and Al. The Al-7.5wt.%Fe sample also contains the Al_2O_3-Al network but with additional Fe-rich phases. The Fe-rich phases have plate-like features and are interconnected with the other phases. XRD could not accurately determine the exact composition of the Fe-rich phases due to their relatively low concentrations. Both samples exhibited appreciable amounts of Si based on EDS and XRD analysis. EDS and PCA mapping was utilized to examine the distribution of Si in the Al-7.5wt.%Fe sample. In areas that do not contain iron the Si precipitates as concisely defined particles. Where as, in Fe-rich areas the Si is more disperse. S/TEM observation coupled with EDS analysis of an Fe-rich area shows the formation of larger Al-Fe intermetallics surrounded by smaller Al-Fe-Si and Al-Fe-Si-O phases.

Both the Al and Al-7.5wt.%Fe samples exhibited a Y-shaped boundary feature that is positioned symmetrically to the corners and edges of the sample. It was found that the boundary is formed primarily by the intersection of Al_2O_3 colonies. Further investigation of the colonies revealed that primary growth of Al_2O_3 phases is in the z-direction (perpendicular to the sample edges) and that some branching occurs in the x and y directions. The Y-shaped boundary is accentuated by a series of voids in both samples. The voids are not completely empty but contain an interconnected network of some phase or phases. In the Al-7.5wt.%Fe sample, the boundary feature is uniform throughout the material. By contrast, the boundary in the Al sample is inconsistent, specifically near the sample corners. Cracking and defects can be observed along the Y-shape in the Al sample, as well as features that have microstructures that differ significantly from the rest of the material. The Al_2O_3 phases contained in the features are finer and unidirectional, meaning they do not exhibit the branching typical found in the bulk of the material.

Focused ion polishing was used to examine the Al_2O_3-Al network in the Al sample and in an Fe-less region of the Al-7.5wt.%Fe sample. Ion polishing revealed features that could not be observed in the mechanically polished samples. It showed that the precipitated Si particles in the Al sample are small and elongated as compared to the larger, more compact particles found in the Al-7.5wt.%Fe sample. FIB polishing also revealed that the Al_2O_3 phases in the Al sample contain a considerable amount of cracking. Since the cracks are partially or completely filled with Al metal, it was concluded that the cracking occur during the RMP process and not during handling. This sort of cracking was not observed in the Al-7.5wt.%Fe sample, though the FIB polished area only represents a small section of the entire material. Tilting the Al sample to induce ion channeling revealed sub-micron sized Al grains. Image analysis of the FIB polished areas showed that both samples contain approximately 65% ceramic and 35% metallic phases.

Analysis of the supplementary materials offered some insight into the features observed in the Al and Al-7.5wt.%Fe samples. For example, the precipitated Si particles found in the melt sample confirms that Si diffuses into the metal bath during processing. In addition, the investigation of the Al-25wt.%Si sample suggests that the decreased volumetric contraction during solidification and increase fluidity contributed by the excess Si helped decrease the overall porosity of the material. It also eliminated the series of voids that form along the Y-shaped boundary.

The partially transformed Al(2hr) sample was particularly useful in understanding the transformation process. It shows that the reaction between pure Al and SiO_2 yields an uneven reaction interface that contains pockets of a transition material. The pockets are separated from the transformed product by an additional layer of transition material. Polarized light microscopy shows that the pocketed areas and transition layer have different morphologies. The Al_2O_3 phases of the transformed product have sharper features near the reaction front compared to the rest of the material. The results from the Al(2hr) sample provide a basis for future research.

In conclusion, the microstructures of two Al/Al alloy-Al_2O_3 IPC's were investigated. The 7.5 weight percent Fe-alloy addition to the RMP process did not affect the overall shape and size of the Al_2O_3-Al network. However, it introduced intermetallic phases that can contribute their characteristics to the material. Imperfections along the Y-shaped boundary prevalent in the Al sample were drastically reduced in the Al-7.5wt.%Fe sample. An increase in porosity throughout the bulk of the Al-7.5wt.%Fe sample was noticed when compared to the Al sample. While more research is necessary to determine the exact transformation mechanisms, the microstructural differences between the two samples confirms the notion that additions to the RMP process can produce IPC's that have properties tailored to specific applications.

5.1. Future Work

Currently, TEM analysis is being utilized to provide a more thorough understanding of the micro and atomic-structures of the presented IPC's. High resolution micrographs can show the presence of nano-scale phases that are beyond the resolution of SEM or XRD. It can also show the bonding properties of the different phases on an atomic scale. Electron diffraction is being used to determine the exact structures and compositions of the intermetallic phases found in the Al-7.5wt.%Fe sample. In the future, 3D reconstruction using FIB techniques may be instrumental in understanding the distribution of phases throughout the microstructure. The 3D reconstruction of a material can be accomplished by serially sectioning a sample using ion milling while simultaneously capturing micrographs at each step. Software programs can reassemble the micrographs to provide a 3D representation of the sample.

It is recommended that future work focuses on the transformation mechanism. A thorough understanding of how and why an IPC is formed during the RMP process will be infinitely useful in optimizing the product properties. An immediate approach is by identifying the compositions and structures of the pockets and transition layer in the Al(2h) sample. This may provide information about the chemical reactions that take place during RMP. Analytical techniques that can be used to address this issue include TEM, XRD, and Raman spectroscopy. Of course, the analysis of more samples transformed under different conditions will also be useful. Future experiments should include both partially and completely reacted materials so that the reaction interface can be examined and correlated to the final material properties.

Future work should also address the series of voids that form along the Y-shaped boundary. The voids can contribute to decreased mechanical properties and pose a serious issue for the implementation of IPC's in industrial applications. Therefore, steps should be taken to eliminate the processing factors that contribute to the void formation. Quenching and directional cooling are methods that can be used to test the theory suggesting that the volumetric contraction of the metal phases during solidification is the cause of this issue.

Chapter 6: References

6.1. Publications and Presentations Based on the Present Research

1. Yurcho, A. Peters, K.M., Hetzel, B., Zeller, M., Wagner, T.R. and Solomon, V.C. (2011). Microstructural Analysis of Ceramic-Metallic Interpenetration Phase Composites. *Proceedings of the 2011 ASEE North Central & Illinois-Indiana Section Conference*, Mt. Pleasant, MI. April 1-2, 2011.

2. Yurcho, A. (2011). Material Characterization of Ceramic-Metallic Interpenetrating Phase Composites. *Youngstown State University Quest 2011*, Youngstown, OH. April 5, 2011.

3. Yurcho, A. (2011). Structural and compositional investigation of Al-alloy-Al2O3 based ceramic-metallic composites using JEOL JIB-4500 MultiBeam System. *Advances in FIB-SEM and TEM for materials science applications – JEOL Seminar*, Youngstown, OH. April 12, 2011.

4. Yurcho, A. Peters, K.M., Hetzel, B., Zeller, M., Wagner, T.R. and Solomon, V.C. (2011). Microstructural and Compositional Investigation of Al-alloy-Al2O3 Ceramic-Metallic Composites Synthesized by Reactive Melt Penetration. *The Eight International Congress in Materials Science and Engineering – ISSIM 2011*, Iasi, Romania. May 26-29, 2011. [accepted]

5. Yurcho, A. Peters, K.M., Hetzel, B., Zeller, M., Wagner, T.R. and Solomon, V.C. (2011). Electron Microscopy Study of Co-Continuous Al-Fe/Al2O3 Composite Synthesized by Reactive Melt Infiltration. *Microscopy & Microanalysis 2011 Meeting*, Nashville, TN. Aug. 7-11, 2001. [accepted]

6. Yurcho, A. Peters, K.M., Hetzel, B., Zeller, M., Wagner, T.R. and Solomon, V.C. (2011). Structural and compositional investigations of ceramic-metal interpenetrating phase composites produced by reactive metal penetration in molten Al and Al-Fe alloy. *Materials Science & Technology 2011 Conference & Exhibition*, Columbus, OH. Oct. 16-20, 2011. [accepted]

6.2. References

7. La Vecchia, G., Badini, C., Puppo, D. and D'Errico, F. (2003). Co-continuous Al/Al_2O_3 composite produced by liquid displacement reaction: Relationship between microstructure and mechanical behavior. *Journal of Materials Science*,

vol. 38, 3567-3577.

8. Paul, R. (2007). Microstructural and Chemical Characterization of Interpenetrating Phase Composites as Unique Refractory Materials Produced Via Reactive Metal Penetration. Master's Thesis, Youngstown State University, Youngstown, OH U.S.A.

9. Clarke, David R. (1992). Interpenetrating Phase Composites. *Journal of the American Ceramic Society*, vol. 75(4), 739-759.

10. Hemrick, J.C., Hu, M.Z., Peters, K.M. and Hetzel, B. (2010). Nano-Scale Interpenetrating Phase Composites (IPC's) for Industrial and Vehicle Application. (ORNL/TM-2010/80) Oak Ridge, TN.

11. San Marchi, C., Kouzeli, M., Rao, R., Lewis, J.A. and Dunand, D.C. (2003). Alumina-aluminum interpenetrating-phase composites with three-dimensional periodic architecture. *Scripta Materialia*, vol. 49(9), 861-866.

12. Kim, J.S., Kwon, Y.S., Lomovsky, O.I., Korchagin, M.A., Mali, V.I. and Dudina, D.V. (2006). A synthetic route for metal-ceramic interpenetrating phase composites. *Material Letters*, vol. 60, 3723-3726.

13. Subramanian, R., McKamey, C., Schneibel, J., Buck, L. and Menshhofer, P. (1998). Iron aluminide-Al_2O_3 composites by in situ displacement reactions: processing and mechanical properties. *Materials Science and Engineering*, vol. A254, 119-128.

14. Yoshikawa, N., Hattori, A. and Taniguchi, S. (2003). Growth rates and microstructure of reacted layers between molten Al-Fe alloy and SiO_2. *Materials Science and Engineering*, vol. 342(A), 51-57.

15. Feng, H. J. and Moore, J. (1995). In situ combustion synthesis of dense ceramic and ceramic-metal interpenetrating phase composites. *Metallurgical and Materials Transactions B*, vol. 26(2), 265-273.

16. Hu, Q., Luo, P. and Yan, Y. (2007). Influence of an electric field on combustion synthesis process and microstructures of TiC-Al_2O_3-Al composites. *Journal of Alloys and Compounds*, vol. 439, 132-136.

17. Zhou, W., Hu, W., and Zhang, D. (1998). Study on the making of metal-matrix interpenetrating phase composites. *Scripta Materialia*, vol. 39(12), 1743-1748.

18. Mattern, A., Huchler, B., Staudenecker, D., Oberacker, R., Nagel, A. and Hoffmann, M.J. (2004). Preparation of interpenetrating ceramic-metallic composites. *Journal of European Ceramic Society*, vol. 24, 3399-3408.

19. Breslin, M. C., Ringnalda, J., Xu, L., Fuller, M., Seeger, J., Daehn G. S., Otani T., and Fraser, H. L. (1995). Processing, microstructure, and properties of co-

continuous alumina-aluminum composites, *Materials Science and Engineering*, Vol. A195, 113-119.

20. Murthy, V.S.R., Kawahara, K., Saito, Y., Matsuzaki, T. and Watanabe, T. (2005). Orientation and Grain Boundary Microstructure of Alumina in Al/Al_2O_3 Composites Produced by Reactive Metal Penetration. *Journal of the American Ceramic Society*, vol. 88(10), 2902-2907.

21. Liu, W. and Köster, U. (1996). Criteria for formation of interpenetrating oxide/metal-composites by immersing sacrificial oxide preforms in molten metals. *Scripta Materialia*, vol. 35(1), 35-40.

22. Wang, L.L., Munir, Z.A. and Maximov, Y.M. (1993). Thermite reactions: their utilization in the synthesis and processing of materials. *Journal of Materials Science*, vol. 28, 3693-3708.

23. Xi, W., Zhou, H., Ma, C., Duan, H. and Zhang, T. (2007). Thermodynamic analysis of thermite reactions for synthesizing Ni-based alloys. *Journal of Materials Science*, vol. 42(20), 8489-8495.

24. Peters, K.M. and Hetzel, B. (2010). Private communication regarding the TCON process. Fireline Inc., Youngstown, OH.

25. Daehn, G.S. and Breslin, M.C. (2006) Co-continuous composite materials for friction and braking applications. J*ournal of the Minerals, Metals and Materials Society*, vol. 58(11), 87-91.

26. George, H. (1955). Manufacture of Articles from Substances Containing Silica. *U.S. Patent No. 2,702,750*.

27. Aghajanian, M.K. and Newkirk, M.S. (1992). Aluminum Metal Matrix Composites. *U.S. Patent No. 5,298,339*.

28. Cannell, J.C., Leaper, R.S. and Parratt, N.J. (1976). Method of Manufacturing Composite Materials. *U.S. Patent No. 3,970,136*.

29. Grimshaw, R.W. and Poole, C. (1980). Composite Materials and Their Production. *U.S. Patent No. 4,232,091*.

30. Sane, A.Y., Wheeler, D.J. and Kuivila, C.S. (1983). Aluminum Wettable Materials. *European Patent No. 94,353*.

31. Yeshwant, S.A., Wheeler, D.J., Gagescu, D., Debely, P.E., Adorian, I.L. and Derivaz, J.P. (1984). Aluminum Production Cell Components. *European Patent No. 115,742*

32. Landingham, R.L. (1973). Method for Forming Metal-Filled Ceramics of Near Theoretical Density. *U.S. Patent No. 3,718,441*.

33. Newkirk, M.S. and Dizio, S.F. (1986). Novel Ceramic Materials and Methods for Making Same. *U.S. Patent No. 4,713,360*.

34. Breslin, M.C. (1993). Process for Preparing Ceramic-Metal Composite Bodies. *U.S. Patent No. 5,214,011*.

35. Peters, K.M., Cravens, R.M., Hemrick, J.G. (2009). Advanced ceramic composites for improved thermal management in molten aluminum applications. Energy Technology Perspectives: Conservation, Carbon Dioxide Reduction and Production from Alternate Sources – *Proceedings of Symposia held during TMS 2009 Annual Meeting and Exhibition*, 241-248.

36. Way, H. (2008). Media-Milled Nanoparticles Boosts Ceramic Armor. *American Ceramic Society Bulletin*, vol. 87(5), 20-24.

37. Konitzer, L.N., Fargo, M.V., Brininger, T.L. and Reed, M.L. (2008). Association between back, neck, and upper extremity musculoskeletal pain and the individual body armor. *Journal of Hand Therapy*, vol. 21(2), 143-148.

38. Chin, E.S.C. (1999). Army focused research team on functionally graded armor composites. *Materials Science and Engineering*, vol. 25A(2), 155 – 161.

39. Hart, S.V. (2004). Status Report to the Attorney General on Body Armor Safety Initiative Testing and Activities. (NJC 204534) Washington, D.C.

40. Ilic, N., Jovanovic, M.T., Todorovic, M., Trtanj, M. and Saponjic, P. (1999). Microstructural and Mechanical Characterization of Postweld Heat-Treated Thermite Weld in Rails. *Materials Characterization*, vol. 43(4), 243-250.

41. Kallio, M., Ruuskanen, P., Maki, J., Poylio, E. and Lahteenmaki, S. (2000). Use of the Aluminothermic Reaction in the Treatment of Steel Industry By-Products. *Journal of Materials Synthesis and Processing*, vol. 8(2), 87-92.

42. Mu, L., Yin, S., Yanping, W. and Heyi, L. (1997). The characteristics of combustion in a centrifugal-thermite process. *Journal of Materials Science*, vol. 32(17), 4711-4713.

43. Mei, J., Halldearn, H.D. and Xiao, P. (1999). Mechanism of the aluminum-iron oxide thermite reaction. *Scripta Materialia*, vol. 41(5), 541-548.

44. Maleki, A., Panjepour, M., Niroumand, B. and Meratian, M. (2010). Mechanism of zinc oxide-aluminum aluminothermic reaction. *Journal of Material Science*, vol. 45(20), 5574-5580.

45. Rapp, R.A., Ezis, A. and Yurek, G.J. (1973). Displacement Reactions in the Solid State. *Metallurgical Transactions*, vol. 4, 1283-1292.

46. Bialas, H. and Stolz, H.J. (1975). Lattice dynamics of sapphire (corundum), Part

I: Phonon Dispersion by Inelastic Neutron Scattering. *Zeitschrift für Physik B Condensed Matter and Quanta*, vol. 21(4), 319-324.

47. Andersson, J.M. (2005). Controlling the Formation and Stability of Alumina Phases. Ph.D. Dissertation, Linköping University, Sweden.

48. Baker, H. and Okamoto, H. (1992). ASM Handbook, Volume 03 - Alloy Phase Diagrams. ASM International.

49. Rhines, F.N. (1956). *Phase Diagrams in Metallurgy*. New York, NY: McGraw-Hill Book Company, Inc.

50. Cava, S., Tebcherani, S.M., Souza, I.A. and Pianaro, S.A. (2007). Structural characterization of phase transition of Al_2O_3 nanopowders obtained by polymeric precursor method. *Materials Chemistry and Physics*, vol. 103, 394-399.

51. Łodziana , Z. and Parliński , K. (2003). Dynamical stability of the alpha and theta phases of alumina. *Physical Review B*, 67(17), 174106-174106-7.

52. Cai, S.H., Rashkeev, S.N., Pantelides, S.T. and Sohlberg, K. (2003). Phase transformation mechanism between gamma - and theta -alumina. *Physical Review B*, vol. 67 (22), 224104-224104-10.

53. Levin, I. and Brandon, D. (1998). Metastable Alumina Polymorphs: Crystal Structures and Transition Sequences. *Journal of the American Chemical Society*, vol. 81(8), 1995-2012.

54. Timpel, M., Wanderka, N., Murty, B.S. and Banhart, J. (2010). Three-dimensional visualization of the microstructure development of Sr-modified Al-15Si casting alloy using FIB-EsB tomography, *Acta Materialia*, Vol. **58**, 6600-6608.

55. Li, J., Zarif, M. and Schumacher, P. (2010). TEM Investigation of a Novel Fe Containing Phase in High Purity Al-Si-Fe Alloys. *Berg- and Hüttenmännische Monatshefte*, vol. 155(11), 499-505.

56. Liu, P. and Dunlop, G.L. (1988). Crystallographic Orientation Relationships For Al-Fe and Al-Fe-Si Precipitates in Aluminum. *Acta Materialia*, vol. 36(6), 1481-1489.

57. Kaufman, J.G. (1999). *Properties of Aluminum Alloys*. Materials Park, OH: ASM International.

58. Hatch, J.E. (1984). *Aluminum: Properties and Physical Metallurgy*. Metals Park, OH: American Society for Metals.

59. Belov, N. A., Aksenov, A. A. and Eskin, D. G. (2002). *Iron in aluminum alloys: impurity and alloying element*. New York, NY: Taylor and Francis.

60. Subramanian, R., McKamey, C., Buck, L. and Schneibel, J. (1997). Synthesis of iron aluminide-Al_2O_3 by in-situ displacement reactions. *Materials Science and Engineering*, vol. A*239-240*, 640-646.

61. Dolata-Grosz, A., Formanek, B., Sleziona, J. and Wieczorek, J. (2005). Al-FeAl-TiAl-Al_2O_3 composite with hybrid reinforcement. *Journal of Materials Processing Technology,* vol. 162, 33-38.

62. ASM International Handbook Committee (1990). ASM Handbook, Volume 02 - Properties and Selection: Nonferrous Alloys and Special-Purpose Materials. ASM International.

63. Shankar, S., Riddle, Y.W. and Makhlouf, M.M. (2004). Nucleation mechanism of the eutectic phases in aluminum–silicon hypoeutectic alloys. *Acta Materialia*, vol. 52, 4447-4460.

64. Royset, J., Leinum, J.R., Overlie, H.G. and Reiso, O. (2006). An Investigation of the Solubility of Scandium in Iron-bearing Constituent Particles in Aluminium Alloys. *Materials Science Forum*, vol. 519-521, 531-536.

65. Kaushish, J.P. (2010). *Manufacturing Processes.* Second Edition. New Dehli: PHI Learning Private Limited.

66. Liu, Z.K. and Chang, A. (1999). Thermodynamic Assessment of the Al-Fe-Si System. *Metallurgical and Materials Transactions A*, vol. 30A, 1081-1095.

67. Cizek, P. (2006). Electron microscopy investigation of the TiBAl and TiCAl grain refiner master alloys, *Journal of Physics*, vol. 26, 107-110.

68. National Bureau of Standards, US. (1981). Monogr. 25(18), 5.

69. Shabashov1, V.A., Brodova, I.G., Mukoseev, A.G., Sagaradze, V.V. and Litvinov, A.V. (2007). Deformation-induced phase transformations in the Al–Fe system under intensive plastic deformation. *Journal of Physics: Condensed Matter*, vol. 19, 1-16.

70. Li, L., Zhang, Y., Esling, C., Jiang, H., Zhao, Z., Zuoa, Y. and Cuia, J. (2010). Crystallographic features of the primary $A_{13}Fe$ phase in as-cast Al–3.31wt% Fe alloy. *Journal of Applied Crystallography*, vol. 43, 1108-1112.

71. Raghaven, V. (2002). Al-Fe-Si (Aluminum-Iron-Silicon). *Journal of Phase Diagram Equilibria and Diffusion*, vol. 32(2), 140-142.

72. Callister, W.D. (2005). *Fundamentals of Materials Science and Engineering*. Second Edition. John Wiley & Sons, Inc.

73. Mertz, J. (2010). *Introduction to Optical Microscopy*. Greenwood Village, CO: Robert and Company Publishers.

74. Delly, J.G. (2008). Essentials of Polarized Light Microscopy. College of Microscopy. Westpoint, IL.

75. Bozzola, J.J. and Russell, L.D. (1992). *Electron Microscopy: Principles and Techniques for Biologists.* Toronto: Jones and Bartlett Publishers.

76. Skoog, D.A., Holler, F.J. and Crouch, F.A. (2006). *Principles of Instrumentation Analysis*. Fifth Edition. Brooks Cole.

77. Volkert, C.A. and Minor, A.M. (2007). Focused Ion Beam Microscopy and Micromachining. *MRS Bulletin*, vol. 32, 389-395.

78. Williams, D.B. and Carter, C.B. (2009). *Transmission Electron Microscopy: A Textbook for Materials Science, Part 1*. New York, NY: Springer Science+Business Media, LLC.

79. Pecharsky, V.K. and Zavalij, P.Y. (2003). *Fundamentals of Powder Diffraction and Structural Characterization of Materials*. New York, NY: Springer Science+Business Media, Inc.

80. Guinebretière, R. (2007). *X-ray Diffraction by Polycrystalline Materials*. Newport Beach, CA: ISTD, Ltd.

81. Bruker AXS. (2001). *D8 Advanced X-ray Diffractometer User's Manual: Vol. II.* Karlsruhe, Germany: Bruker AXS GmbH.

82. Smith, W.F. and Hashemi, J. (2009). Foundations of Material Science and Engineering. Fifth Edition. New York, NY: McGraw Hill College.

83. ASTM Standard C1327-08 (2008). Standard Test Method for Vickers Indentation Hardness of Advanced Ceramics. (DOI: 10.1520/C1327-08) ASTM International, West Conshohocken, PA.

84. Aluminum Iron Powder Diffraction File; International Centre for Diffraction Data: Newtown, PA, 2011; PDF# 00-050-0797 (accessed 10 Feb 2011).

85. Aluminum Oxide Powder Diffraction File; International Centre for Diffraction Data: Newtown, PA, 2011; PDF# 00-010-0173 (accessed 10 Feb 2011).

86. Aluminum Powder Diffraction File; International Centre for Diffraction Data: Newtown, PA, 2011; PDF# 00-004-0787 (accessed 10 Feb 2011).

87. Silicon Diffraction File; International Centre for Diffraction Data: Newtown, PA, 2011; PDF# 00-010-0173 (accessed 10 Feb 2011).

88. National Institute of Health. ImageJ software, version 1.44. *U.S. Department of Health and Human Services*, <http://rsbweb.nih.gov/ij/>, (accessed 2011).